Les nanoparticules du groupe IV pour l'imagerie et la thérapie cellulaire

Alexander Kharin

N° d'ordre 32-2016 Année 2016

THÈSE DE L'UNIVERSITÉ DE LYON

Délivrée par l'UNIVERSITÉ CLAUDE BERNARD LYON 1

Et l'ÉCOLE DOCTORALE INTERDISCIPLINAIRE SCIENCES-SANTÉ

Pour l'obtention du DIPLÔME DE DOCTORAT

Spécialité BIOCHIMIE

Soutenue publiquement le 25 février 2016

par

Alexander KHARIN

Group IV nanoparticles for cell imaging and therapy

DIRECTEUR DE THESE
Dr Alain GELOEN

CODIRECTEUR DE THESE
Dr Vladimir LYSENKO

MEMBRES DU JURY

Dr Vladimir SIVAKOV
Pr Luigi BONACINA
Pr Olivier TILMENT (Président)
Dr Vladimir LYSENKO
Dr Alain GELOEN (invité)

Table of contents

List of acronyms

AFM – atomic force microscopy

CFO – carbon fluorooxide

DLS – dynamic light scattering

IR – infrared

NPs – nanoparticles

PDT – photodynamic therapy

PSi – porous silicon

SEM – scanning electron microscopy

SHG – second harmonic generation

TEM – transmission electron microscopy

TPEF – two photon excited fluorescence

UV – ultraviolet

XRD – x-ray diffraction

UNIVERSITE CLAUDE BERNARD - LYON 1

Président de l'Université	**M. François-Noël GILLY**
Vice-président du Conseil d'Administration	M. le Professeur Hamda BEN HADID
Vice-président du Conseil des Etudes et de la Vie Universitaire	M. le Professeur Philippe LALLE
Vice-président du Conseil Scientifique	M. le Professeur Germain GILLET
Directeur Général des Services	M. Alain HELLEU

COMPOSANTES SANTE

Faculté de Médecine Lyon Est – Claude Bernard	Directeur : M. le Professeur J. ETIENNE
Faculté de Médecine et de Maïeutique Lyon Sud – Charles Mérieux	Directeur : Mme la Professeure C. BURILLON
Faculté d'Odontologie	Directeur : M. le Professeur D. BOURGEOIS
Institut des Sciences Pharmaceutiques et Biologiques	Directeur : Mme la Professeure C. VINCIGUERRA
Institut des Sciences et Techniques de la Réadaptation	Directeur : M. le Professeur Y. MATILLON
Département de formation et Centre de Recherche en Biologie Humaine	Directeur : Mme. la Professeure A-M. SCHOTT

COMPOSANTES ET DEPARTEMENTS DE SCIENCES ET TECHNOLOGIE

Faculté des Sciences et Technologies	Directeur : M. F. DE MARCHI
Département Biologie	Directeur : M. le Professeur F. FLEURY
Département Chimie Biochimie	Directeur : Mme Caroline FELIX
Département GEP	Directeur : M. Hassan HAMMOURI
Département Informatique	Directeur : M. le Professeur S. AKKOUCHE
Département Mathématiques	Directeur : M. le Professeur Georges TOMANOV
Département Mécanique	Directeur : M. le Professeur H. BEN HADID
Département Physique	Directeur : M. Jean-Claude PLENET
UFR Sciences et Techniques des Activités Physiques et Sportives	Directeur : M. Y.VANPOULLE
Observatoire des Sciences de l'Univers de Lyon	Directeur : M. B. GUIDERDONI
Polytech Lyon	Directeur : M. P. FOURNIER
Ecole Supérieure de Chimie Physique Electronique	Directeur : M. G. PIGNAULT
Institut Universitaire de Technologie de Lyon 1	Directeur : M. le Professeur C. VITON
Ecole Supérieure du Professorat et de l'Education	Directeur : M. le Professeur A. MOUGNIOTTE
Institut de Science Financière et d'Assurances	Directeur : M. N. LEBOISNE

Résumé:

La biomédecine et la biophotonique sont des champs de recherches en plein expansion qui grandissent à vive allure, constituant un secteur entier d'activités novatrices. Ce secteur, vraiment interdisciplinaire, comprend le développement de nouveaux nanomatériaux, de sources lumineuses et l'élaboration de nouveaux concepts, de dispositifs/équipements pour quantifier la conversion de photons et leurs interactions. L'importance décisive du diagnostic précoce et du traitement individuel des patients exige des thérapies soigneusement ciblées et la capacité de provoquer sélectivement la mort cellulaire des cellules malades. Malgré les progrès spectaculaires réalisés en utilisant les points quantiques ou des molécules biologiques organiques pour l'imagerie biologique et la libération ciblée de médicaments, plusieurs problèmes restent à résoudre : obtenir une sélectivité accrue pour une accumulation spécifique dans les tumeurs et une amélioration de l'efficacité des traitements. D'autres problèmes incluent la cytotoxicité et la génotoxicité, l'élimination lente et la stabilité chimique imparfaite. Des espérances nouvelles sont portées par de nouvelles classes de matériaux inorganiques comme les nanoparticules à base de silicium ou à base de carbone, qui pourraient faire preuves de caractéristiques de stabilité plus prometteuses tant pour le diagnostic médical que pour la thérapie. Pour cette raison, la découverte de nouveaux agents de marquage et de transport de médicaments représente un champ important de la recherche avec un potentiel de croissance renforcé.

Dans ce travail nous nous sommes intéressés à 5 types différents de nanoparticules du groupe IV. Elles ont été synthétisées de différentes manières. Le premier type de nanoparticules a été produit à partir de silicium poreux par anodisation électrochimique d'une plaque de silicium monocristallin. Cette technique très connue permet de produire des nanoparticules ayant une structure poreuse et une photoluminescence (PL) très intense. Les nanoparticules de silicium poreux sont des agglomérats de minuscules grains de silicium de 3 nm. Le second type est représenté par des nanoparticules de 20 nm de silicium cristallin produites par ablation laser dans l'eau, d'un substrat de silicium. Ces nanoparticules ne présentent pas de PL sous excitation UV, mais elles sont luminescentes sous excitation à deux photons. Le troisième type de nanoparticules sont des nanoparticules de diamant de 8 nm produites par ablation laser dans un liquide. Les nanodiamants sont luminescents. En solution, ils forment des agrégats de 20 nm. Le quatrième type est représenté par les nanoparticules de fluooroxide de carbone, non cristalline, semi-organique de 8 nm faisant preuve d'une forte luminescence. Elles se dispersent parfaitement bien dans l'eau sans former d'agglomérat. Le dernier type de particules est de relativement grande taille (100-200nm) de carbure de silicium produites par carboréduction du

silicium. Elles sont luminescentes et à la différence des autres nanoparticules elles ont une structure cristalline non-centrosymétrique ce qui les rend parfaitement adaptées pour une interaction optique non linéaires.

Toutes les particules ont été testées pour l'imagerie sur des cellules 3T3-L1, avec différents modes de détection : fluorescence excitée à un ou deux photons ou la génération de seconde harmonique. Les nanoparticules les plus intéressantes pour la détection en microscopie fluorescente excitée par un photon sont les nanoparticules de silicium poreux, les nanodiamants et les nanoparticules de fluooroxide de carbone (CFO). Les nanoparticules de silicium poreux et les nanodiamants ont été observées dans le cytoplasme des cellules tandis que les CFO pénètrent dans le noyau des cellules. Les particules de SiC de grande taille et celles de 20 nm de silicium peuvent générer des signaux de seconde harmonique, de telle sorte qu'il est possible de les visualiser en microscopie.

La toxicité des nanoparticules a été mesurée par une méthode non invasive basée sur impédancemétrie qui permet de mesurer la prolifération cellulaire en temps réel. Leur toxicité est inférieure de plusieurs ordres de grandeurs à celle de nanoparticules inorganiques telles que celle en or ou en Fe_3O_4. La faible toxicité des nanoparticules du groupe IV, rend leur utilisation parfaite pour l'imagerie cellulaire. La localisation des nanoparticules de CFO est particulièrement fascinante, puisqu'elles se concentrent dans le noyau des cellules quand celles-ci se divisent. Nous avons étudié leurs caractéristiques de capture intra-cellulaire.

L'objectif final de la mise au point des NPs est leur utilisation *in vivo*. Cela signifie que lors de leur utilisation, en injection périphérique (intraveineuse ou intraabdominale) elles seront en contact avec de nombreuses molécules biologiques présentent dans le sang ou le liquide interstitiel. L'albumine est la protéine la plus présente dans le sang. La capacité de fixation des nanoparticules à l'albumine a été mesurée. Les nanoparticules de CFO et de Si se fixent facilement à l'albumine. L'incubation préliminaire des nanoparticules de CFO avec certains acides aminés réduit fortement leur liaison à l'albumine. Cette observation est intéressante car la fixation de nanoparticules de CFO à l'albumine diminue fortement sa pénétration intra-cellulaire.

Parce que les propriétés des nanoparticules de CFO sont très intéressantes, notamment leur pénétration intra-nucléaire, elles ont été testées sur des cellules cancéreuses. Nous avons observé que les nanoparticules de CFO sont moins toxiques pour les cellules non cancéreuses (3T3-L1) que pour les cellules cancéreuses (HSC, HuH7, Panc01, HepG2). Cet effet est le résultat d'une capture intracellulaire supérieure des nanoparticules par les cellules cancéreuses

que par les cellules non cancéreuses. Cette différence désigne les nanoparticules de CFO comme un bon candidat pour la thérapie anti-cancer.

Par ailleurs les ultrasons (US), à une intensité 1000 fois inférieure à celle utilisée pour les applications médicales, détruisent les cellules qui contiennent des nanoparticules de CFO. Il est possible de focaliser les ultrasons avec une grande précision. Cet avantage permettrait de palier l'inconvénient d'une répartition non spécifique des NPs, résultant en une destruction très focalisée des foyers tumoraux.

En conclusion, nos résultats montrent que les nanoparticules du groupe IV permettent de réaliser une imagerie cellulaire multi-modale, les différents types de nanoparticules présentant des avantages variés selon le type de modalité envisagé. Les nanoparticules du groupe IV sont moins toxiques que les autres nanoparticules inorganiques. Leur comportement en présence de matériel biologique suggère que certaines d'entre elles sont de bons candidats pour la thérapie contre le cancer.

Thesis structure

This work shows the progress in research dedicated to the applications of nanoparticles for cell labeling and therapy: 1st chapter is an introduction, 2nd chapter of research is a review of state of art on group IV nanoparticles synthesis and applications as labels for microscopy and as an agents for cancer therapy. 3rd chapter describes the materials and equipment used in the current work. 4th chapter is dedicated to the synthesis and characterization of the nanoparticles. 5th chapter shows examples and comparisons of different nanoparticles as labels for optical microscopy. 6th chapter includes the investigation of utilization of carbon fluorooxide nanoparticles for the cancer therapy. 7th chapter is a general discussion and it contains analysis and comparison of different nanoparticles properties and the possibilities of their applications. 8th chapter is a conclusion which shows the progress made by the work and further perspectives.

1. Introduction

Inorganic nanoparticles are extremely interesting object for the investigation since the quantum dot luminescence discovery in 1981 by Alexey Ekimov [1]. The main advantages using different points of view can be observed:

1. At the "physical" point of view, the properties of crystalline NPs are different from the properties of the bulk material. The quantum confinement effect can be observed in relatively small (less than 100 nm) objects and it may cause the shift of PL bands. In case of ferromagnetic material, small particles can have superparamagnetic properties. Other property changes are less interesting into the frame of the current work.

2. "Chemically", the main difference between the material into the bulk form and the form of the nanoparticles is about 10^{10} -10^{14} times increased surface per mass unit, so the reactivity of the material in form of nanoparticles can be hundred billion times higher, than the reactivity of the less thin powder.

3. For biologists, the main advantage of nanoparticles is the ability to penetrate through the cell membrane, to be carried by the blood stream and the ability to be bound by the different proteins.

So, by combining all the above mentioned facts, it is possible to conclude that the materials in form of nanoparticles are almost perfectly fit the needs of bioresearch. Nevertheless, they found only limited number of applications, such as the magnetic labels for MRI and the labels for photoluminescent microscopy. The main problem for the bio-application of the nanoparticles is the low biocompatibility and high toxicity of the most common metal or semiconducting nanoparticles.

There are several ways to overcome that limitation.

- First way is the utilization of organic or polymer nanoparticles, particularly the micellar or lyposomic NPs. In this way the problem is evident: using the organic NPs causes the loss of crystallinity and, as a result loss of the most important functional properties. The micelles and other organic NPs are usually used as a carrier for drug delivery. Such kinds of NPs do not use any of the "physical" properties of nanoparticles.
- Second way is a protection of the nanoparticle from the direct contact with any organics. In fact such protection usually is the coating of the particles with the polymers or biologically inert layer. That way is extremely promising and can be used for almost any

type of NPs. Nevertheless, the coverage often increases the sizes of particles too much and, as a result, NPs loose the "biological" advances.

- The third way is the utilization of the common and safe inorganic compounds. The toxicity of carbon or silicon nanoparticles should be much lower than the toxicity of the metal ones. Besides, the nanocarbon and nanosilicon have great number of different forms.

The present work is concentrated on the investigation of different group IV nanoparticles and their applications for the cell imaging and therapy. The most interesting task is the comparison of the nanoparticles which do not differ significantly in order to understand how the different factors influent the properties.

Five different types of group IV nanoparticles were tested for bioapplications: the silicon particles were presented as porous silicon and 20 nm Si particles, carbon particles were 6 nm nanodiamonds and non-crystalline carbon fluorooxide (CFO) nanoparticles, SiC particles were presented in form of 3-c SiC particles.

Such set of the chosen nanoparticles allows varying the different parameters with the other ones remain similar. The pairs of particles for comparison are shown in **Table 1.1**

Different size		Different structure		Different composition		Different crystallinity	
Porous silicon	Silicon 20 nm	Silicon 20 nm	SiC	Porous silicon	Nanodiamonds	nanodiamonds	CFO (non-crystalline)
The same crystallic structure (diamond-like), same composition		Similar crystallite sizes.		The same structure and close sizes		The same size (6-8 nm) and the same composition (carbon)	

Table 1.1: *The pairs of particles for comparison*

So, by the investigation of the behavior of 5 different NPs it is possible to find out the influence of varying size, crystallinity, crystallic structure and composition of NPs.to the intercellular uptake. These specific parameters should have an effect on the physical properties and they could define the special ways of applications. For example, bulk silicon is not luminescent due to indirect bandgap structure Si in form of small crystallites is luminescent due to quantum confinement effect. The 20 nm Si particles are not luminescent. On the other hand,

the big particles due to large surface can be able to generate second harmonic (SH) signal under visible irradiation. The changes in structure can change the SH ability, change in composition with the same structure and NPs sizes causes the shift of the PL bands. The absence of crystallinity and specific molecular structure in case of CFO NPs allows observing them as semi-inorganic material.

The specific structure, size and composition of the NPs lead to the specific properties and, as a result, some of the nanoparticles types are preferable to be used in specific kinds of applications. The comparison of such properties in accordance with the applications is the main task of the current research.

2. Group IV nanoparticles for bioapplications: a review of State of art

There are lots of different biocompatible inorganic materials; one of the most interesting among them is group IV nanoparticles. Group IV elements play crucial roles both in our daily life and in our bodies. The group IV elements in form of nanoparticles can perfectly fit some needs of bioscience. Other nanoparticles, such as group II–VI quantum dots contain heavy metal elements that are toxic to living cells and tissues[2, 3, 4]. In this respect, group IV nanoparticles bring new hopes as benign materials accompanied by the abovementioned properties, which favor their biological applications.

First section of that chapter describes the variety of the synthetic methods for the group IV nanoparticles, such as Si, C and SiC nanoparticles. Since the surface state is vital for the behavior of such nanoparticles into the biological environment, second section shows the ways of the surface modifications. Than we show the current advances on the of group IV nanoparticles applications for the cell imaging (section 3) and cancer therapy (section 4).

2.1 Fabrication of group IV nanoparticles: advantages and disadvantages top-down vs bottom-up technique

There are two general strategies for the production of the nanoparticles. Nanoparticles can be produced either by the degradation of the bulk material or by the assembly of a smaller species (**Figure 2.1.1**). That group of methods called top-down strategies and it includes, such techniques, as a mechanical grinding with or without addition of special surfactant to the powder, electrochemical etching and lithographical methods. Here is the list with description of the most important top-down techniques

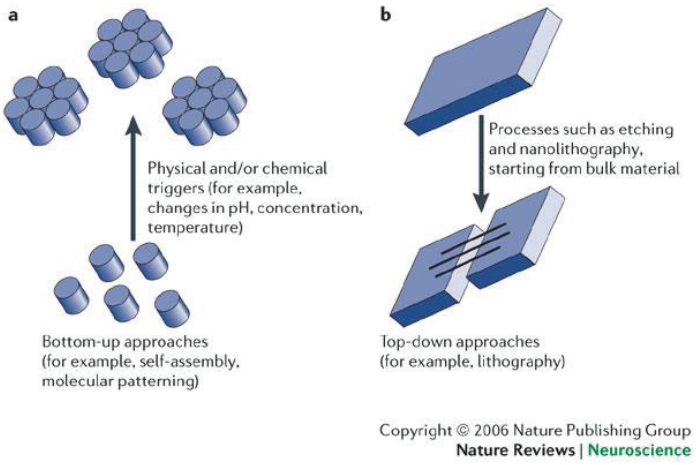

Figure 2.1.1 *The illustration of general difference between top-down and bottom-up synthetic approaches[5]*

- The mechanical grinding of the bulk material. Such method have also thermodynamic limitations – due to the high surface tension energy of free-standing surface , so the small

particles are tend to agglomerate, so it is not possible to make very small particles. That size limitation can be shifted down by the addition of the surfactants during grinding.

- Second method for the formation of nanostructured material is electrochemical or chemical etching of bulk material. In order of better structuring of material, the etching catalyzer can be placed to the material before the etching. The catalyzer can be placed in form of special mask in order to manage the etching process.
- The idea of masking the material before the etching leads us to the lithography technique. The special photo- or -electron sensitive polymer can be placed to the surface of the semiconductor for etching (usually silicon) and after irradiation through the special mask polymer change its properties and it can be removed from the non-irradiated places only. Than in case of etching, only non-covered places are etched.

The second group of methods called bottom-up approach leads to the formation of the nanoparticles from the smaller species, such as atoms, molecules or ions. That group of methods includes combustion synthesis, all of the "wet" chemistry methods, which form the nanoparticles assembled from solutions of precursors under special conditions. The different kinds of chemical vapor deposition lead to the formation of the nanoparticles from gas phase.

- The colloidal synthesis is a group of methods to produce colloids of the nanoparticles, usually quantum dots using reduction of metal ion or other ways of chemical technology.
- The syntheses of nanoparticles from gas or plasma methods are the group of chemical vapor deposition methods. The molecules of precursor in gas phase (or ions in case of plasma activation) are decomposed under several conditions (temperature, catalyst, presence of electric field) at the plate.
- The physical vapor deposition is the similar method, but the difference is that the precursor in PVD is the gas of atoms (not molecules of precursor). The free standing gas of atoms is not stable and they rapidly form the agglomerates. The main difference in methods in this group is the way of atom gas production. That can be laser ablation, sparking ablation, ion or electron beam ablation.

2.1.1 Silicon nanoparticles

Silicon is an essential element to sustain life [6].preliminary studies have also demonstrated the biocompatibility of bulk silicon. [7], Silicon also is the one of the most widely used semiconductors in the world. The silicon technology advances, which necessary to use it as a material for microelectronics allows getting massive production of

the extremely pure (99.9999999%) bulk silicon. Also, using the lithographic technology on the silicon wafer it is possible to get the objects with the sizes down to 10 nm. Since the bulk silicon has an indirect band gap it has poor photoluminescence. However, small-sized silicon (below 5 nm) NPs exhibit relatively strong fluorescence, showing the prospect of long-awaited optical applications. Therefore, intense studies have been intrigued to develop fluorescent silicon NPs and their optics-relative applications since the first observation of porous silicon-based fluorescence. In that case, the 5 nm Si particles gives a near-infrared photon [8].

The silicon nanoparticles can exist in several different forms.

Porous silicon

One of the most widespread and abundant method to get the silicon nanoparticles is electrochemical production of porous silicon. After its discovery in 1956 by Uhlir [10], porous silicon has not atrracted much attention till 1990. In 1990 Canham [11] had discovered room temperature photoluminescence of porous silicon. After such discovery, lots of new research projects on porous silicon have started.

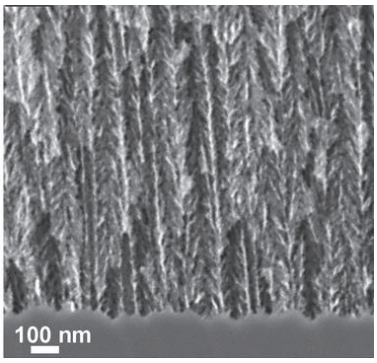

a

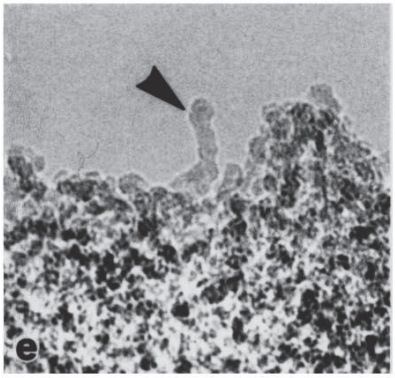

b

Figure 2.1.1.1*: TEM images of non-luminescent porous silicon film (a) and grinded luminescent porous silicon film (b) [9]*

The main preparative method for that material is an electrochemical etching of the bulk silicon in the fluoric acid-ethanol mixture,

Other way of porous silicon production is electroless etching in specific conditions: it is possible to obtain porous silicon through stain-etching with hydrofluoric acid, nitric acid and water. Porous silicon formation by stain-etching is particularly attractive because of its simplicity and the presence of readily available corrosive reagents; namely nitric acid (HNO_3) and hydrogen fluoride (HF).

Depending in the initial wafer orientation [12], its resistivity and conductivity type, mixture composition, current density and illumination during etching, it is possible to get variety of porous structures with the different pores' and particles' sizes. So, we can get highly

controllable method to produce the nanoparticles with relatively small sizes. Nanoporous silicon has remarkably bright photoluminescence with quantum yield up to 50% [13].There are lots of researches concerning to the biomedical applications of porous silicon.

The resulting material – porous silicon has the complicated structure of small Si crystallites (3-4 nm) agglomerated into the pore structure with average pore diameter from micrometers to several nanometers, depending of synthesis conditions. So for the bioapplications, porous silicon powder should be grinded for the formation of smaller particles According to the crystallites' size, they can be both, luminescent or non-luminescent [14]. The big surface area (200-300 m^2/mg) provides usage of the porous silicon as drug carrier. **Figure 2.1.1.1** shows the examples of the electrochemically etched silicon. It is seen, that it exists in form of film (a), which consist of small (4-8 nm) crystallites (b).

Silicon nanocrystals

In recent two decades, many other synthetic strategies (e.g., solution-phase reduction, microemulsion, sonochemical synthesis [21], mechanochemical synthesis, laser ablation [22] and laser pyrolysis of SiH_4 gas [23]) have been developed for the preparation of separated silicon nanoparticles.

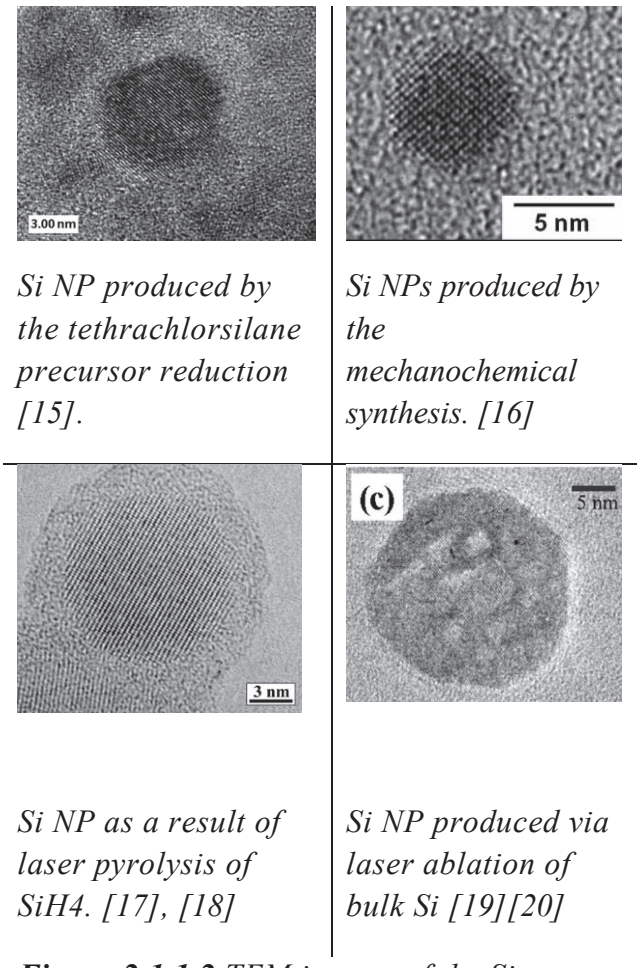

Si NP produced by the tethrachlorsilane precursor reduction [15].

Si NPs produced by the mechanochemical synthesis. [16]

Si NP as a result of laser pyrolysis of SiH4. [17], [18]

Si NP produced via laser ablation of bulk Si [19][20]

***Figure 2.1.1.2** TEM images of the Si nanoparticles obtained by different methods*

- For the solution-phase reduction synthesis proposed by Kauzlarich and coworkers, silicon halides (e.g., SiCl4) are reduced in organic solution (e.g., ethylene glycol dimethyl ether) to produce silicon nanocrystalline under mild conditions [24].
- Mechanochemical synthesis is a method of grinding of bulk silicon in presence of the special reagents. Those reagents can be described as a chemical surfactant that easily reacts with the silicon surface and so, prevent the agglomeration of nanoparticles.

- Silicon clusters and nanocrystals containing up to several thousand atoms per cluster could be generated by pulsed CO2 laser-induced decomposition of SiH_4 in a flow reactor [25] Resulting material for all of these methods is a uniform spherical non-luminescent well-crystalline nanoparticles with sizes from 10 to 100 nm. Depending on the method, the surface coverage and surface groups can vary
- The silicon nanoparticles can be obtained by the ablation of the silicon wafer by laser. The ablation can be done both in vacuum [26] or in liquid [27] medium. The resulting nanoparticles are well crystalline and they can have the sizes from 2 to 40 nm depending on synthesis conditions

Utilization of the described methods allows producing of well-crystalline silicon nanoparticles with the sizes ranged from 2 up to 100 nm (see **Figure 2.1.1.2**). The methods without any coverage and surface protection against oxidation gives core-shell structure with the amorphous silica shell around silicon core (**Figure 2.1.1.2** laser pyrolysed particles).

Silicon nanowires

Silicon nanowires are the material which is a one dimensional silicon structures with a length of several microns and width up to hundred nanometers. Since its discovery in 1960s, by Treuting and Arnold was published [29, 30], they attract a lot of attention due to their potentially interesting semiconducting properties.

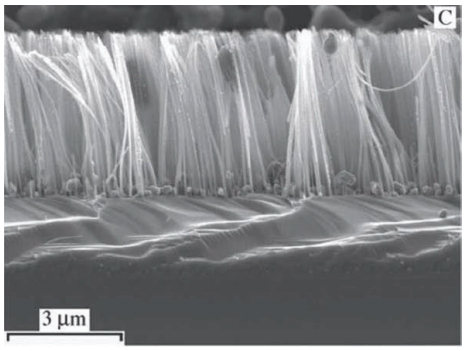

Figure 2.1.1.3 *The silicon nanowires produced by the metal-assisted chemical etching [28]*

The most attractive method for the production of nanowires for bioapplications is a metal-assisted etching. The predeposited metal catalyst (usually silver) causes the specific etching process which can lead to the formation of the arrays of nanowires (**Figure 2.1.1.3**). Those arrays can be easily removed from the substrate and used separately.

2.1.2 Carbon nanoparticles

Carbon is the backbone of all known life-forms on earth. In the human body, it is the second most abundant element by mass after oxygen. Carbon in nature exists mostly in the form of graphite, diamond, and amorphous carbon. The carbon nanomaterials are the fullerenes, single-wall and multiwall nanotubes, nanodiamonds, graphene sheet layers and

graphene-based materials, graphite whiskers [31]. All of these forms should be considered as different materials.

Nanotubes

Carbon nanotubes represent one of the best examples of novel nanostructures derived by bottom-up chemical synthesis approaches. Nanotubes have the simplest chemical composition and atomic bonding configuration but exhibit perhaps the most extreme diversity and richness among nanomaterials in structures and structure - property relations. Single wall carbon nanotubes (SWNTs) can be either metals or semiconductors, with band gaps that are relatively large (0.5 eV for typical diameter of 1.5 nm) or small (10 meV), even if they have nearly identical diameters.

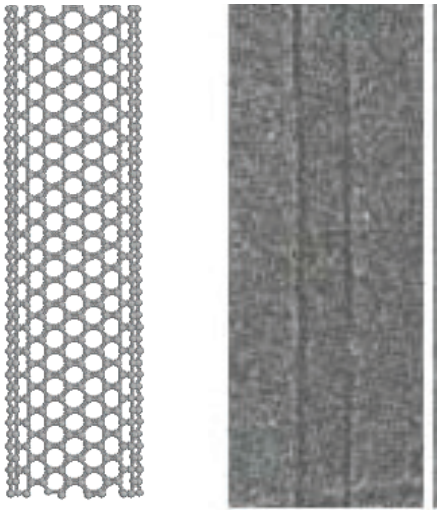

Figure 2.1.2.1*: Schematic honeycomb structure of a single-walled nanotube [32] the TEM image of single-wall carbon nanotube [33]*

Arc-discharge, laser ablation, and chemical vapor deposition have been the three main methods used for carbon nanotube synthesis [34]. The first two employ solid-state carbon precursors to provide carbon sources needed for nanotube growth and involve carbon vaporization at high temperatures (thousands of degrees Celsius). Chemical vapor deposition (CVD) utilizes hydrocarbon gases as sources for carbon atoms and metal catalyst particles as “seeds” for nanotube growth that takes place at relatively lower temperatures (500 - 1000 ° C). For SWNTs, none of the three synthesis methods has yielded bulk materials with homogeneous diameters and chirality thus far. Nonetheless, arc-discharge and laser ablation techniques have produced SWNTs with narrow diameter distributions averaging 1.4 nm.

Fullerenes

A fullerene is a molecule of carbon in the form of a hollow sphere, ellipsoid, tube, and many other shapes. Fullerenes can be synthesized in the laboratory in a wide variety of ways, all involving the generation of a carbon-rich vapor or plasma [35]. All current methods of fullerene synthesis produce primarily C60 and C70 and these molecules are now routinely isolated in gram quantities and are commercially available. Higher-mass fullerenes and endohedral complexes can also be made and isolated, albeit in substantially reduced amounts. At present the most efficient method of producing fullerenes involves an electric discharge between graphite electrodes in 200 torr of He gas. Fullerenes are embedded in the emitted carbon soot and must then be extracted and subsequently purified. The following extraction and purification of fullerenes uses difference in fullerenes solubility in organic solvents ore gase-phase separation using difference in molecular weight of different fullerenes. [36]

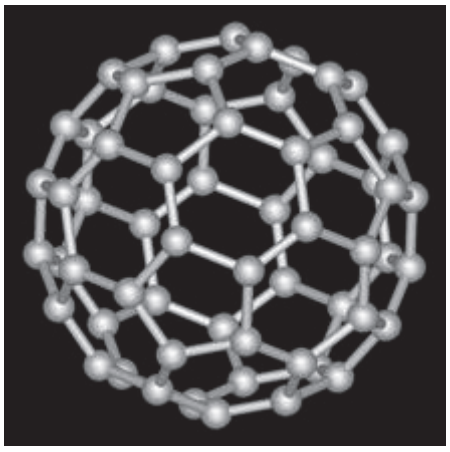

Figure 2.1.2.2 *The schematic structure of fullerenes*

Graphene

Graphene is allotropes of carbon in the form of a two-dimensional, atomic-scale, hexagonal lattice in which one atom forms each vertex. It is the basic structural element of other allotropes, including graphite, charcoal, carbon nanotubes and fullerenes. It can also be considered as an indefinitely large aromatic molecule, the limiting case of the family of flat polycyclic aromatic hydrocarbons.

There are 3 main methods to obtain graphene. 1st method is a separation of a single graphene layer from the graphite. It is possible to use an adhesive tape, sonication in special solvents, such as N-methylpyrrolidone or exfoliation of graphite [37]. The exfoliation can take place both in the solution and in the solid graphite. Graphene in form of epitaxial layers can be obtained using CVD on a SiC or other wafer. Partly oxidation of SiC at high temperatures (above 1100^{o}C) can also give us graphene particles (**Figure 2.1.2.3**). Graphene particle is a set of bound graphene sheets.

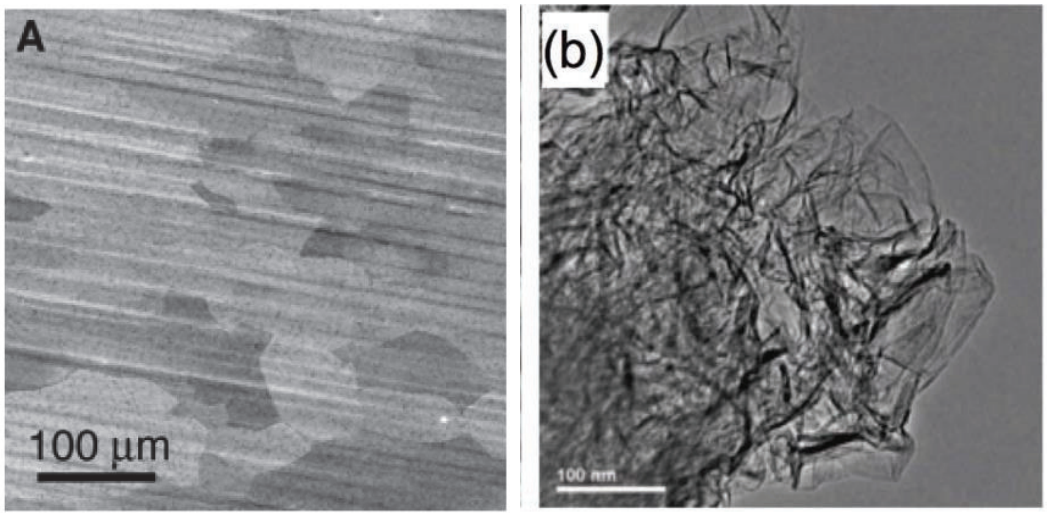

a **b**

Figure 2.1.2.3 *TEM images showing individual graphene sheets (a) and particle composed of agglomerated graphene platelets (b) [37]*

Nanodiamonds

Nanodiamonds are the small crystalline carbon particles (about 5-10 nm)-with the crystalline structure close to one in bulk diamond. The most abundant way to produce them is an explosive synthesis. When an oxygen-deficient explosive mixture of TNT/RDX (2,4,6-Trinitrotoluene abd trini 1,3,5-Trinitroperhydro-1,3,5-triazine) is detonated in a closed chamber, diamond particles with a diameter of ca. 5 nm are formed at the front of detonation wave in the span of several microseconds [38] (**Figure 2.1.2.3**).

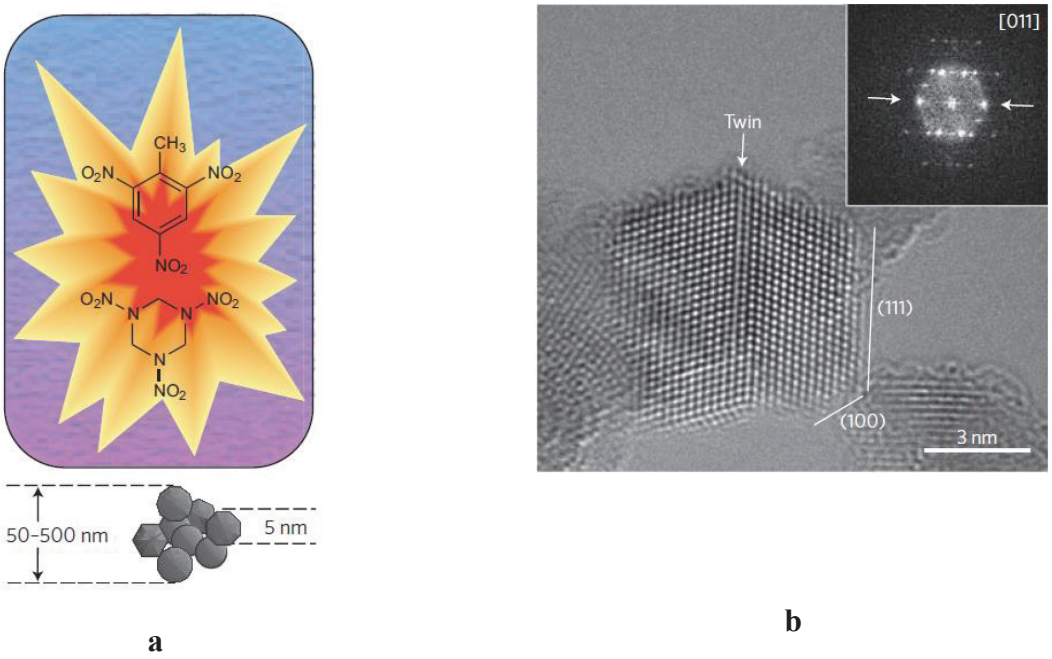

a **b**

Figure 2.1.2.3*: a – Detonation synthesis of nanodiamonds scheme. After detonation, diamond-containing soot is collected from the bottom and the walls of the chamber.*

b –nanodiamond synthesized by detonation method [38]

The study of Khachatryan et al. (2008) [39] shows that diamond microcrystals can also be synthesized by the ultrasonication of a suspension of graphite in organic liquid at atmospheric pressure and room temperature.

It also was show that nanodiamonds can be stably formed in the gas phase at atmospheric pressure and neutral gas temperatures <100 °C by dissociation of ethanol vapor in a microplasma process [40]. Nevertheless; the most popular method for nanodiamonds' synthesis remains detonatinal synthesis. There are also some communications about the other methods for nanodiamonds' formation, such as CVD [41] or colloidal synthesis [42].

Carbide-derived carbon

Carbide-derived carbons (CDCs) represent a new class of nanoporous carbons with porosity that can be tuned with sub-angstrem accuracy in the range 0.5-2 nm. CDCs have a narrower pore size distribution than single-wall carbon nanotubes or activated carbons; their pore size distribution is comparable with that of zeolites.

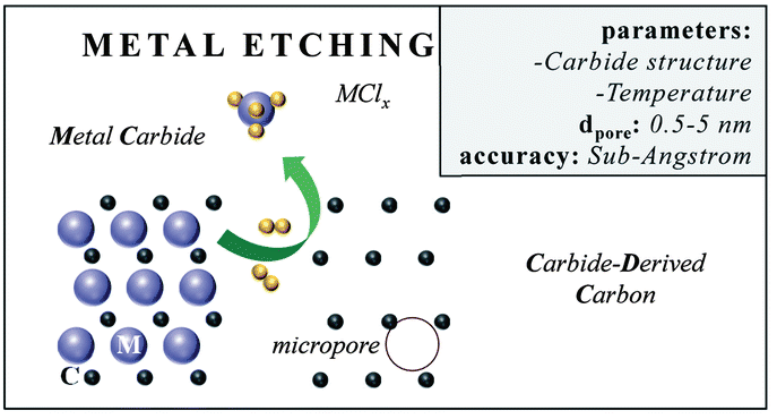

***Figure 2.1.2.4**: the mechanism of CDC the formation [43]*

Leaching in supercritical water or high-temperature treatment in halogens can be used to remove metals from carbides producing carbon coatings, powders or components (**Figure 2.1.2.4**). Since the rigid metal carbide lattice is used as a template and the metal is extracted layer-by-layer, atomic level control can be achieved in the synthesis process and the carbon structure can be templated by the carbide structure. Further structure modification and control can be achieved by varying the temperature, gas composition, and other process variables. Unlike carbons of organic origin, CDCs produced by chlorination do not contain hydrogen.

Comparison of scattered literature data on CDCs shows that, for different carbides (SiC, TiC, ZrC, B_4C, TaC, Mo_2C and many others) and chlorination temperatures, pores of any size between 0.5 and 5 nm, determined by the structure of the carbide precursor and process parameters, were produced [44].

2.1.3 Silicon carbide nanoparticles

Silicon carbide is a well-known semiconductor with excellent biocompatibility [46]. Neither silicon nor carbon causes deleterious effects such as cytotoxicity. Therefore, silicon carbide is very promising in the biomedical field having many potential cardiovascular applications. In addition, luminescent silicon carbide nanocrystals may be good light emitters in biological imaging [45].

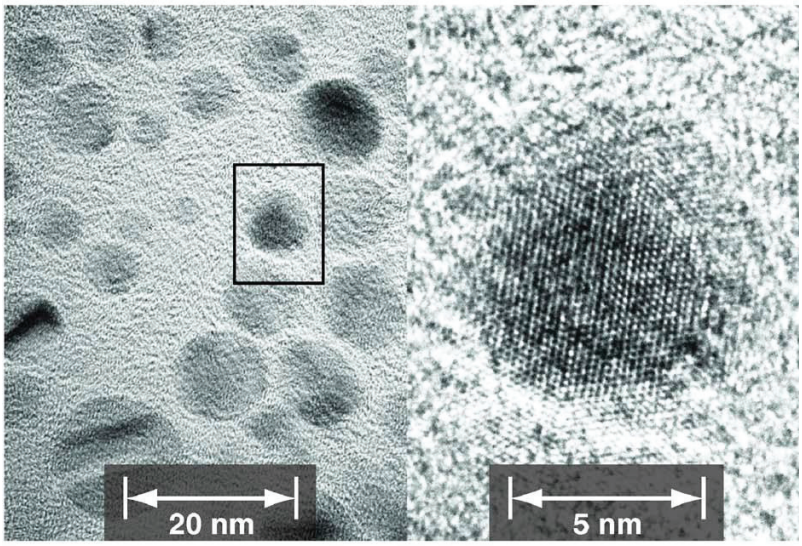

Figure 2.1.3.1: *TEM image of 6H SiC nanoparticles and enlarged image of isolated silicon carbide nanoparticle showing visible lattice fringes from a single SiC nanoparticle. [45]*

SiC nanocrystals can be obtained by the large number of methods, such as ion implantation of carbon ions into the silicon matrix, laser pyrolysis of mixture of silicon and carbon-contained gases, chemical vapor deposition and thermoreduction of SiO2 nanoparticles, synthesis of amorphous SiC nanoparticles using the low pressure microwave plasma,- synthesis α-SiC nanocrystals by carbothermic reduction [47].

Since the silicon carbide nanoparticles are less investigated than the silicon or carbon ones, there is no “standard” industrial method for synthesis of large quantities of nanoparticles. Every abovementioned method has its own advantages and disadvantages (see **Table 2.1.3.1**)

Synthesized method	Efficiency	Cost	T°C	Diameter	Catalyst
Carbon nanotube confined reaction	Low	Higher	1400	20-25	No
Arc discharge	Higher	Low	3000	20-60	Yes
Laser ablation	High	High		20-70	Yes
Sol-gel and carbothermal reduction	Higher	Low	900	40-80	No
Chemical vapor deposition	Higher	Higher	1100	10-100	Yes
High-frequency induction heating	Higher	Low	1450	5-25	No

***Table 2.1.3.1**: the advantages and disadvantages of the different methods for SiC nanoparticles synthesis [*48*]*

Silicon carbide nanoparticles produced by etching of 6H SiC are shown on **Figure** 2.1.3.1. It is clearly seen, that the etching of 6H SiC yields well-crystallined 5 nm SiC nanoparticles.

2.2 Surface chemistry of group IV nanoparticles

This section will describe the general methods ant techniques that can be used for the change of the group IV nanoparticles surface state and the chemical modifications of the surface.

The aims of the modification are varying depending on the nanoparticles application. The problems which can solve the surface modification are the low solubility of NPs or too high dissolution rate (for porous silicon). More complicated reasons are concerned to the functional action of NPs. For example, surface can be modified with so-called vectors for specific targeting or with the drug to use the particle as a drug carrier.

There are 2 general methods to cover the nanoparticles with some other compound. First one is a physical absorption on the surface, usually realized as a polymer coating [49]. The second is a chemical binding of the compound to the NPs. The chemical binding usually includes 2 steps: First is the specific reaction of the particle's surface with the organic compound in order to change the "inconvenient" surface chemistry to more common organic one.

After initial coating, it is easy to handle with further modification of surface. It can be more useful and easier to react than the initial one. The main standard coupling reactions for such kind of modification are shown at **Figure 2.2.1** and can be used for

every kind of particles. But the first step – coupling to organic radicals should be described for each kind of particles separately.

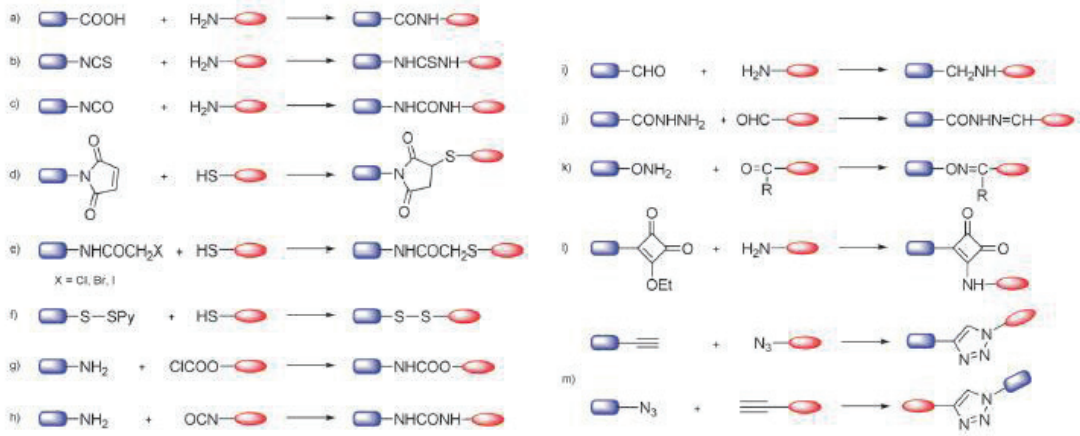

Figure 2.2.1: *typical coupling reactions for modification of NPs surface [50]*

2.2.1 Silicon particles

Surface of the silicon itself can be easily oxidized by the contact with water, producing thick (15 nm) layer of the silicon oxide. Since the nanoparticles of silicon have the less size, they are not stable in water suspensions. The dissolution rate of nc-Si in aqueous solution depends on the pH level (acidity or alkalinity) and varies from 1 nm/day to 1 μm/day [51].

The process of the silicon nanoparticles dissolution sometimes has to be more controllable. In case of porous silicon [52], the particles are the 100-200 nm aggregates of the small (2-3 nm) crystallites. Because of such structure and hydrophobicity of bulk silicon, it is difficult to oxidize the inner particles with water and the oxidation is dramatically slow down. Other way to protect the silicon from the oxidation is a modification of the nanoparticles' surface with the some radicals. It can prevent the accessibility of the silicon core from the outer water. The bigger particles (more than 100 nm) do not need any protection from oxidation because the silicon core still remains after surface oxidation.

The chemical modification of silicon surface lies on 2 reaction types:

First one is hydrosililation or interaction of double or triple c-c bond of non-saturated molecule with the Si-H bond at the surface: Such kind of reaction requires initial nanoparticles hydrogen-terminated (**Figure 2.2.1.1**).

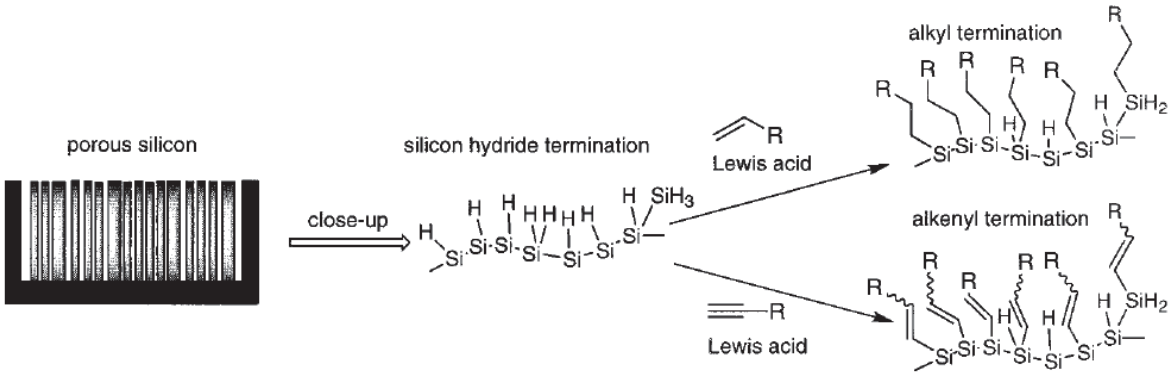

Figure 2.2.1.1: *the reaction between the hydrogen-terminated porous silicon and non-saturated hydrocarbons. [53]*

So, the contact with water should be avoided before the end of the reaction [52]. Hydrosililation can be catalyzed by UV irradiation or metal (usually Pt or Pd) catalyzer, otherwise it requires temperatures above 120°C.

Other way is protecting of partly oxidized particles with aminopolysilane (APTES) – that is reaction with Si-OH surface groups [54] or other kinds of silane derivatives (**Figure 2.2.1.2**).

The non-chemical grafting with some biological polymers (i.e dextran) is also common way to change the surface state of the silicon particles.

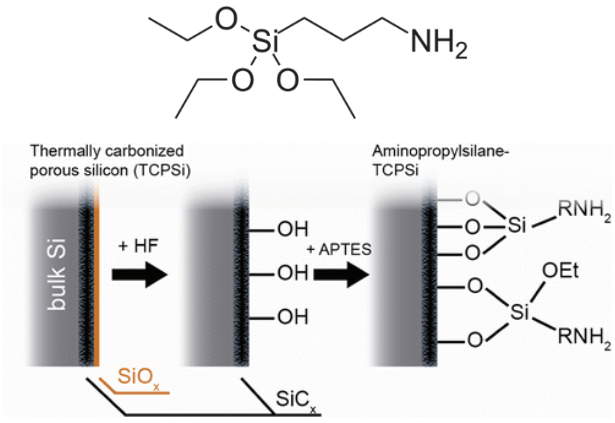

Figure 2.2.1.2: *APTES strucutre and the reaction between the hydroxyl-terminated porous silicon and aminopyrosilane.[54]*

2.2.2 Carbon particles

The surface chemistry of carbon particles is the same as for aromatic carbon structures in organic chemistry, so it can be modified by all of the methods, concerning to coupling with hydroxyl, carboxyl, ester and other common groups. In case of non-saturated, but stable SP^2 hybridized c-c bonds (in fullerenes or nanotubes), the reaction with Si-OH bond of silane can occur, but it requires at least tome atoms SP^3 hybridized.

So, the most popular way to modify the carbon SP^2 hybridized particles is partly oxidation of aromatic C-C bonds. Since the structure is stable, it is difficult to oxidize them without complete destruction of structure. The methods for mild oxidation of carbon are:

O_2 or O_3 plasma treatment, chemical oxidation with HNO_3 or H_2SO_4 or H_2O_2, electrochemical oxidation and other ways *[55]* (see **Figure 2.2.2.1a**).

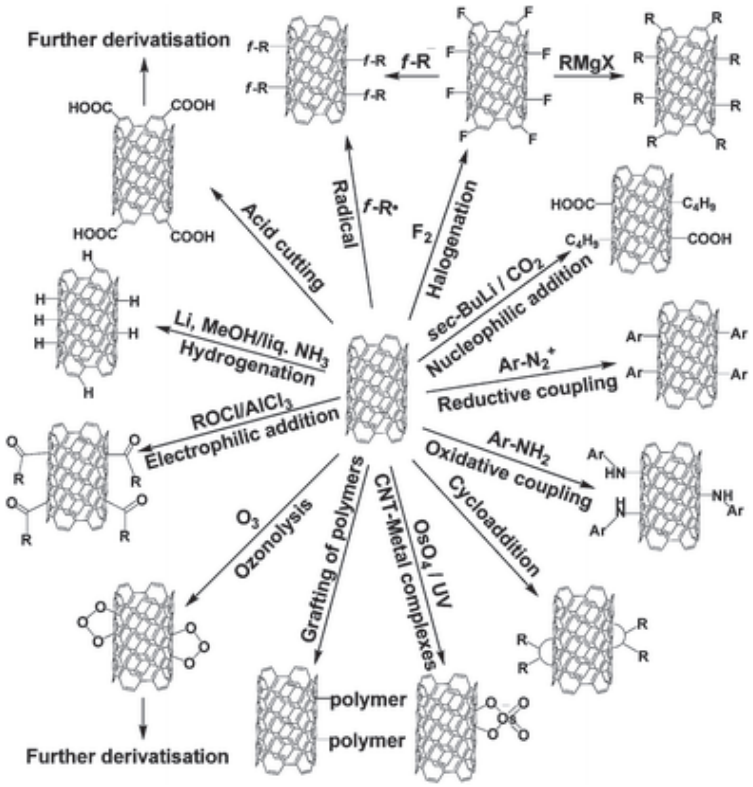

a

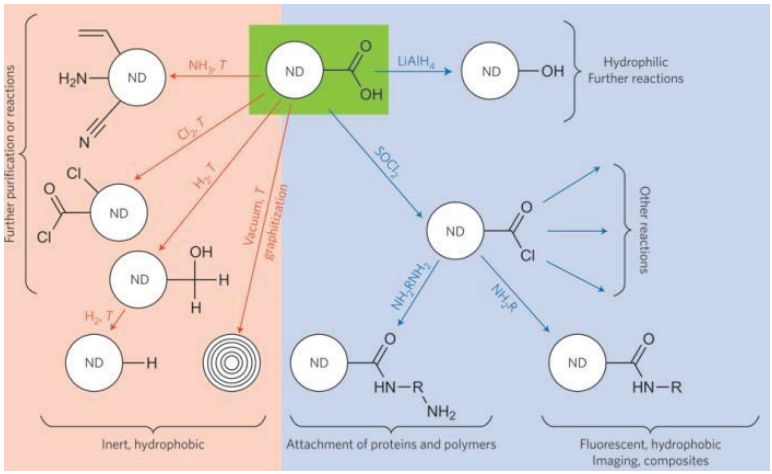

b

Figure 2.2.2.1*: the most common ways to modify the carbon nanoparticles: a - carbon nanotubes [55] b – nanodiamonds [56]*

SP^3 hybridised C atoms of nanodiamonds or oxidized nanotube or grapheme sheet are much easier to conjugate with the organic compounds. Depending on synthesis method,

they are initially terminated with C-OH or COOH groups and very suitable for further modification (**Figure 2.2.2.1b**.) using the methods of the organic chemistry. [56]

2.2.3 SiC particles

While the successful application of the SiC nanoparticles in bioimaging techniques is related to their bioinert and photostable properties further applications in medicine and drug delivery rely on the ability of engineering the desired surface properties by attaching different functional molecular groups. To obtain tailor-made functionalized surfaces it is necessary to understand the complex structure of the SiC surface. The surface of the silicon carbide nanoparticles can be predominantly terminated either with Si-OH groups or C-OOH groups. The Si-OH surface groups can be modified the same way as Si-OH groups of silicon NPs [57, 58]. The APTES or other silane derivates can easily react with the Si-OH groups (**Figure 2.2.3.1**).

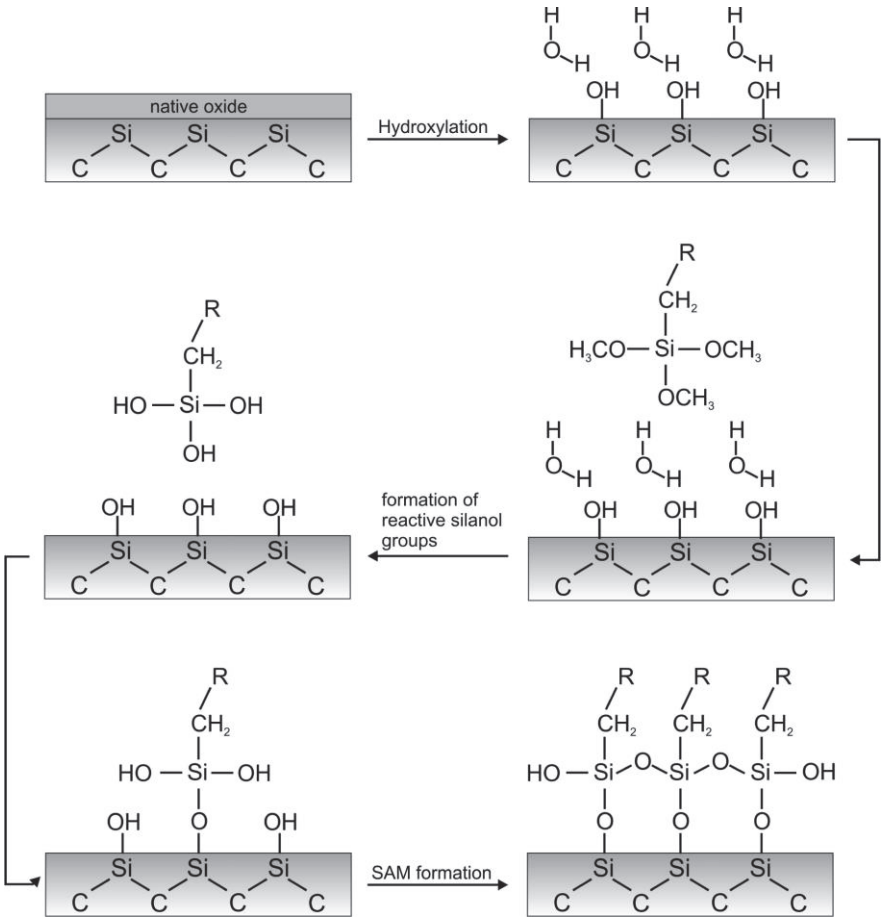

Figure 2.2.3.1: *the reaction scheme between the hydroxyl-terminated porous silicon and aminopyrosilane. [59]*

The other possibility to change the surface chemistry of such particles is reaction with amines (in case of initially carboxyl-terminated NPs)

$$SiC - COOH + NH_2R \rightarrow SiC - CONHR + H_2O$$

This kind of reaction can occur under the catalyzer action in water-free medium.

2.3 Group IV nanoparticles for cell imaging

The term imaging can be understood in many ways imaging can be spilited to; optical, mechanical, spectroscopy, acoustic, or photoacoustic. Imaging is a kind of photography in most people's perception. Scientific imaging goes far beyond this. Images can additionally be created by diverse methods such as (near) infrared and Raman spectroscopy, electrochemical imaging using rastering electrodes, by mechanical methods such as AFM, and by even more sophisticated scanning methods. It has become accepted that virtually any method yielding a 2-dimensional picture can be referred to as ''imaging''. Many of these methods are destructive or require extensive sample preparation, but others are not and therefore well applicable to living systems or intact tissues. The group IV nanoparticles are most applicable for the tasks of optical imaging. That section is dedicated to the optical cell imaging modalities and describes the progress in group IV nanoparticles applications for imaging.

Optical imaging describes various imaging techniques using visible, ultraviolet, and infrared light used in imaging. The process which underlies the interaction of the object with the light defines the optical imaging methods. The most evident optical imaging technique is a bright field imaging, where the interaction of the light with the sample can be considered as a simple reflecting, transmittance or scattering. The photoluminescent imaging is based on the absorbance of the light with a short wavelength and re-emission in a spectral range with longer wavelength. The difference in wavelengths allows discriminating the exciting and emitted light using filters and estimating the position of the fluorescent molecules or the species. Some of materials are able to simulteniously absorb 2 photons and emit the light with shorter wavelength. The two photon excited luminescence (TPEL) microscopy uses the principle of such idea. Due to some specificities of TPEL, TPEL microscopy is usually realized in form of sample scanning, where the focused laser beam scans the sample pixel by pixel. The other optical effect which also requires the intense laser irradiation is the second harmonic (SH) generation. Special materials (usually structured at atomic scale, but non-symmetric) are able to generate the light with half wavelength compared to the excitation light. The SH microscopy is an optical technique which detects the SH light. Other non-linear effect that can be used for imaging is Raman effect – effect of shifting of the excitation light wavelength due to vibrations of material. Raman imaging is also usually performed in form of sample scanning. One of the "hybrid" optical-ultrasound imaging techniques that

requires special sensitizers is a photoaccoustic imaging, where the absorbed light cause the irradiation of the acoustic wave in form of ultrasound. Below we describe optical imaging techniques and its benefits in biological imaging applications.

2.3.1 One-photon excited photoluminescent cell imaging

Depending on nanoparticles' sizes, the silicon nanoparticles, nanodiamonds, nanotubes and carbon dots could be used both for in-vitro cell imaging or in-vivo imaging.

Silicon particles

Silicon particles for imaging are usually used in form of microporous silicon, since lack of luminescence for bigger Si particles and fast oxidation of non-porous particles. Specially coated in order to prevent dissolution, they can be effectively used for cell imaging in vitro [60] (**Figure 2.3.1.1**) or even in-vivo cancer cell imaging.

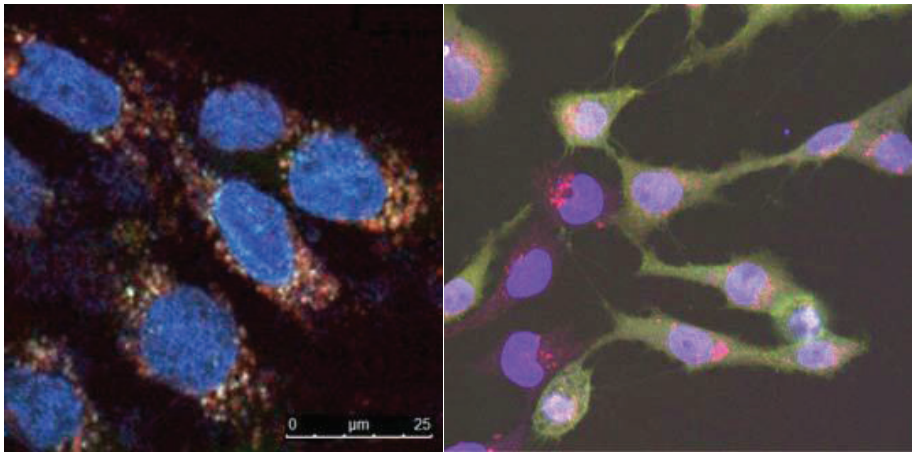

Figure 2.3.1.1 *Photoluminescent image of CF2Th (dog thymus) cells with Silicon nanoparticles. Blue and red colors correspond to cell nuclei and SiNPs, respectively [61] [62]*

The emission in red-near IR spectral range, which is weakly absorbed by the body, allows observing the fluorescence originated from the several centimeters depth inside the body. **Figure 2.3.1.2** shows the accumulation of the silicon nanoparticles inside the mouse body via photoluminescence detection.

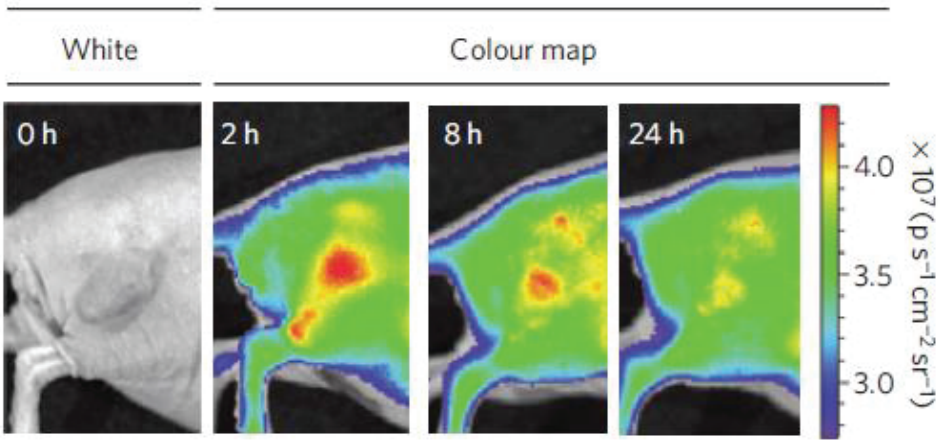

Figure 2.3.1.2: *Fluorescence images of a mouse bearing an MDA-MB-435 tumour. The mouse was imaged using a Cy5.5 excitation filter and an ICG emission filter at the indicated times after intravenous injection of SiNPs (20 mg/kg) [63]*

Carbon particles

Carbon particles can be used for imaging in forms of graphene dots, nanotubes or nanodiamonds. Nanodiamonds and carbon or grapheme quantum dots show good ability to penetrate inside the cell cytoplasm (**Figure 2.3.1.2**) and they have similar spectral characteristics of photoluminescence. There is no significant difference into the NPs distribution inside the cells, labeled by the nanodiamonds and grapheme dots.

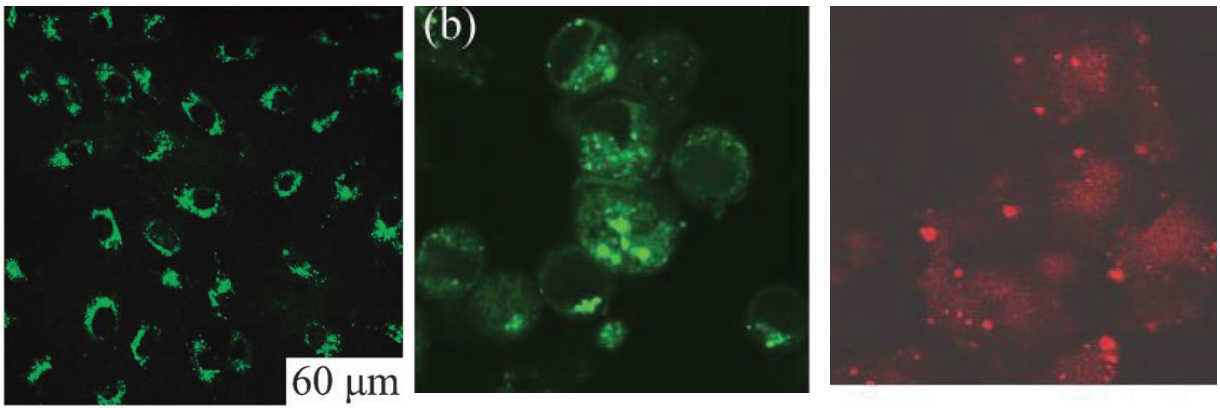

Figure 2.3.1.2:*The cells labeled with carbon NPs* ***a*** *labeling of MG-63 cells with graphene quantum dots [64]* ***b*** *Caco-2 cells from the uptake experiment with the carbon dots, excited at 488 nm and detected in the 530–750 nm range* ***c*** *Confocal microscopy image of fluorescent nanodiamond swallowed by 293T human kidney cells about 33 um in size. The bright red spots are nanodiamonds. [65]*

The higher quantum yield and much lower cytotoxicity of nanodiamonds compared to other carbon nanomaterials make them preferable material for imaging. Since broad luminescence peak, the nanodiamonds luminescence can be detected in red-IR range, so the

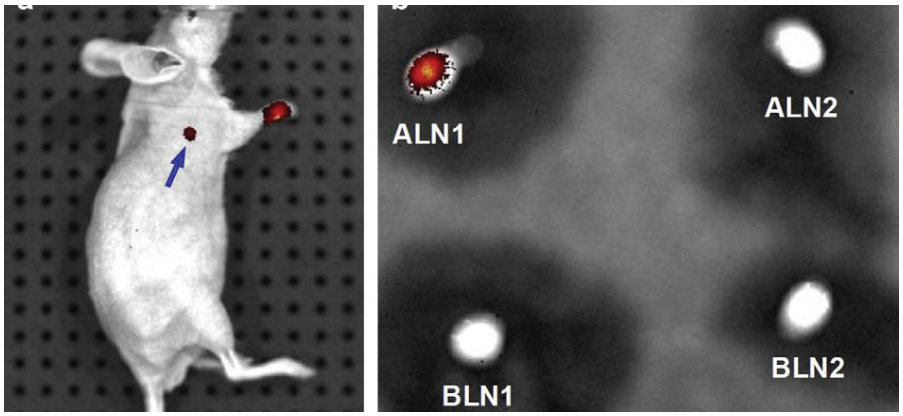

a

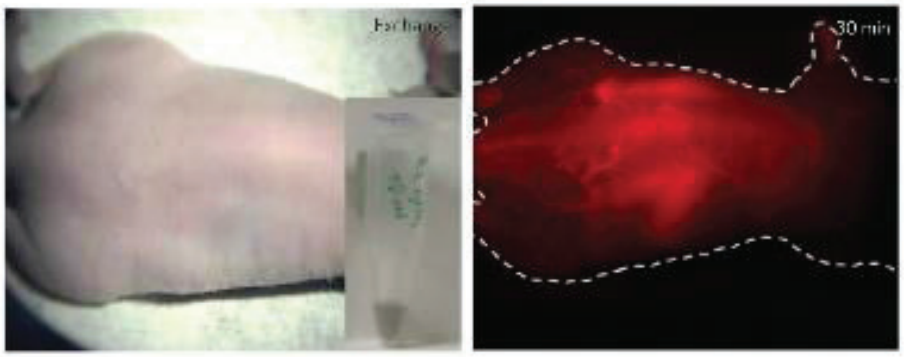

b

Figure 2.3.1.3:*in vivo labeling with carbon particles*

a In vivo and lymph node imaging of a nude mouse after injection of nanodiamonds. [66]

b NIR photoluminescence images of nude mice treated with PEG-bound carbon nanotubes[67].

nanodiamonds could be also used for the in-vivo imaging (**Figure 2.3.1.3a**).

Some kinds of carbon nanotubes also have the luminescence in near-IR range, so they can be easily used for in-vivo PL imaging (**Figure 2.3.1.3b**). Surface modification of such tubes can increase the efficiency of such kind of imaging.

Silicon carbide NPs

Silicon carbide also can be used for the cell imaging and, as it was shown [68] that Nps distribution inside the cells depends on the surface state of the particles. It is possible

to obtain silicon carbide images with uniform distribution inside the cells *[69] [70]* (**Figure 2.3.1.4**).

(a)

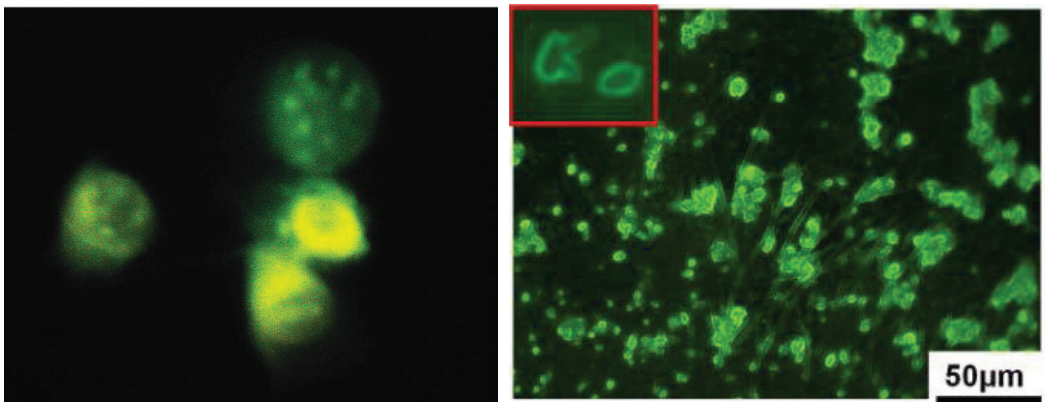

Figure 2.3.1.4: *images of hFOB and Aureobasidium pulluans cells after 3C–SiC nanocrystal uptake excited at 420–490 nm c examined with a fluorescence microscope. First image width 93 um [69,70]*

The photoluminescence in green-blue spectral range of the silicon carbide does not allow performing any in vivo photoluminescent imaging experiments.

2.3.2 Two-photon excited luminescence

The concept of two-photon excitation is based on the idea that two photons of comparably lower energy than needed for one photon excitation can also excite a fluorophore in one quantum event. Each photon carries approximately half the energy necessary to excite the molecule. An excitation results in the subsequent emission of a fluorescence photon, typically at a higher energy than either of the two excitatory photons. The probability of the near-simultaneous absorption of two photons is extremely low. This is the reason why 2PA is only observed in intense laser beams, particularly focused pulsed lasers, which generate a very high instantaneous photon density. Most of the applications for 2PA result from this intensity dependence. [71].

The most commonly used fluorophores have excitation spectra in the 400–600 nm range, whereas the laser used to excite the two-photon fluorescence lies in the ~700–1000 nm (infrared) range. If the fluorophore absorbs two infrared photons simultaneously, it will absorb enough energy to be raised into the excited state. The fluorophore will then emit a single photon with a wavelength that depends on the type of fluorophore used (typically in the visible spectrum).

Porous silicon has PL signal at the red-IR range, so it can give 2-photon excited fluorescence signal. Under IR excitation it is possible to perform even-in vitro cell imaging [72]. The in vitro images are shown on the **Figure 2.3.2.1**.

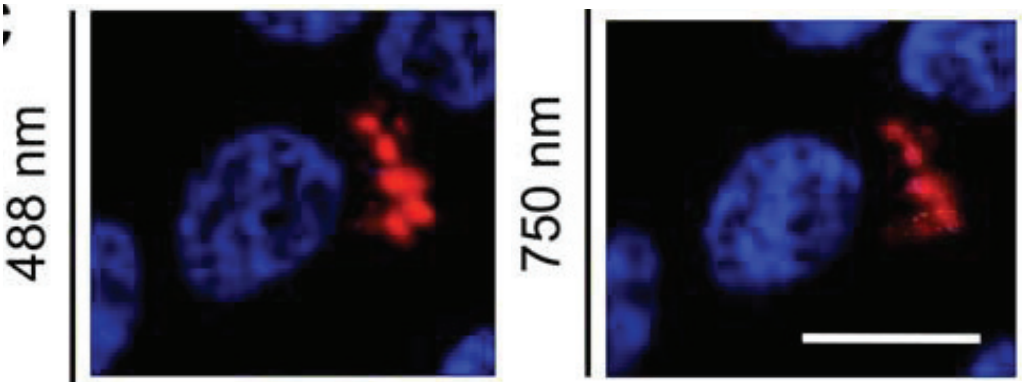

Figure 2.3.2.1: *Single photon (left) and multi-photon (right) fluorescence microscope images of celluar uptake of SiNPs on HeLa cells. The scale bar is 20 μm in vitro cellular imaging with SiNP. HeLa cells were treated with SiNP for 2 h, fixed and then imaged*

The Silicon nanoparticles are clearly observable inside the cells under two-photon excitation conditions as well as with single-photon excitation.

Both carbon nanotubes [73] and carbon dots [74] are found able to luminesce in 400-550 nm wavelength region under IR excitation. So, such materials also can be used for two-photon cell imaging. The localization of the quantum dots inside the cells is in coincidence with 1 photon excited microscopy and the carbon dots are mainly localized into the cell's cytoplasm (**Figure 2.3.2.2**)

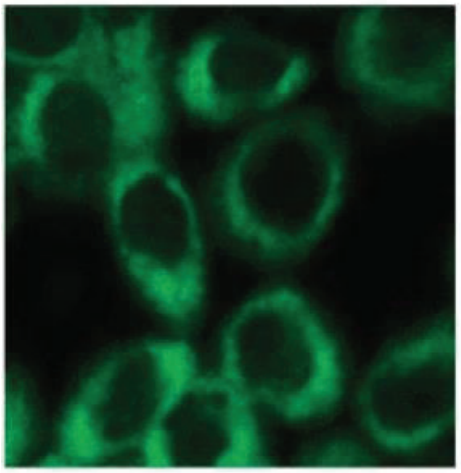

Figure 2.3.2.2: *representative two-photon luminescence image (800 nm excitation) of human breast cancer MCF-7 cells with internalized carbon dots. [73]*

SiC QDs were found to have a strong emission at the 400-500 nm wavelength under two-photon excitation. It is possible to detect fluorescence from SiC QDs injected to neuron cells by a two-photon microscope (**Figure 2.3.2.3**).

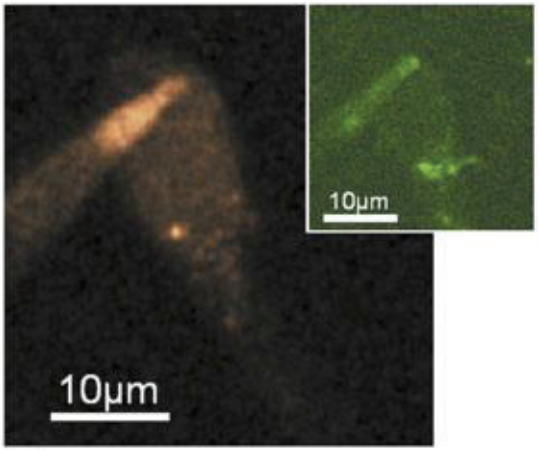

Figure 2.3.2.3: *Two-photon imaging of a neuron labeled by SiC QDs. Red fluorescence signal (600–700 nm, red channel) was generated at 830 nm excitation. Inset, the same neuron but fluorescent signal was collected from 425 to 525 nm (green channel) [75]*

2.3.3 Raman microscopy

Raman spectroscopy is a spectroscopic technique used to observe vibrational, rotational, and other low-frequency modes in a system. Raman Effect is an inelastic scattering of light on vibrational or other modes. The energy of the scattered light is shifted, with the shift corresponding to the vibrational frequencies of the molecule. For spectroscopy, the down-shifted peak is usually used to estimate the vibrational states.

Raman spectroscopy can be performed by the microraman setup and scanning the surface with the laser beam. In this case, it is possible to get the Raman "map" of the sample. Since well-crystallized nanoparticles itself have strong Raman signal, it is possible to use them as a markers for Raman microscopy measurements. Carbon nanotubes could be used as markers to visualize the cells (**Figure 2.3.3.1**). The different isotopical composition of the CNT allows to discriminate the chemically identical CNT via raman imaging and estimate the selectivity of different CNT-drug conjugates. Figure 2.3.3.1 shows the possibility of selective labeling. C-13 consisted CNT, C-13 contained CNTs and C12 CNT were conjugated to the antibodies selective for different cell lines. Such method leads to the specific labeling of the different cells.

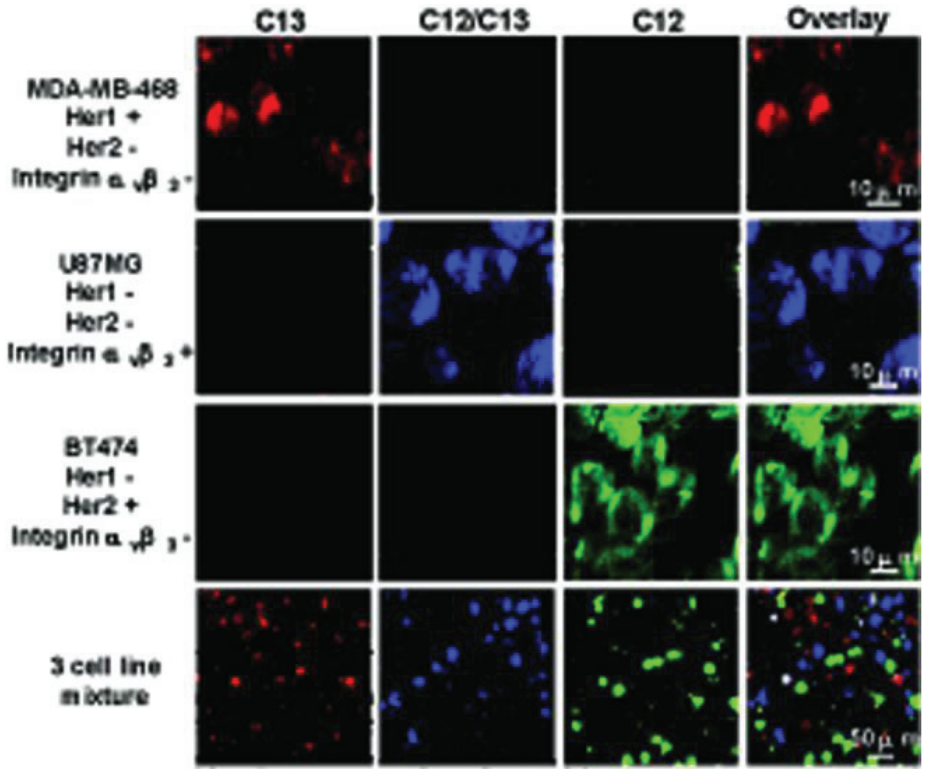

Figure 2.3.3.1*: multi-color Raman imaging with SWNTs. Deconvoluted confocal Raman spectroscopy images of three different cell lines after incubation with a mixture of the three-color SWNTs (top 3 rows, red, blue, green colors are Raman intensities of C12, C12/C13 and C13 SWNTs respectively). In the bottom row, a mixture of three cell lines was incubated with the three color SWNT mixture. Those images clearly show a mixture of cells with differentiated Raman labeling by three types of SWNTs. Occasional co-localization of different colors could due to dead cells or non-specific nanotube binding. [76]*

There are no studies about Raman mapping using other group IV particles.

2.3.4 Photoacoustics

Photoacoustic imaging also called optoacoustic or thermoacoustic imaging has emerged as a promising non-invasive imaging modality, which combines the spectral selectivity of molecular excitation by laser light with the high resolution of ultrasound imaging. Currently, two photoaccoustic techniques are actively studied: photoacoustic tomography (PAT) and photoacoustic microscopy (PAM). PAM typically uses a raster-scanned focused ultrasonic detector coupled with confocal optical illumination

The group IV nanoparticles usually used for photoaccoustic imaging are the carbon nanotubes [77], carbon dots [78]. Different kinds of silicon nanoparticles are also able to generate photoacoustic signal, but it is too weak to use it for imaging [79]. The example of PA imaging using carbon nanotubes is shown on **Figure 2.3.4.1.** With the administration of the carbon nanotubes in water (0.2 μM), the optical absorption of the blood was increased and the

contrast between the vessels and the background tissues was enhanced. Thus, in **Figure 2.3.4.1 b–e**, the vasculature is seen with greater clarity in comparison to **Figure 2.3.4.1a. Figure 2.3.4.1e** was acquired at 30 min post-injection of nanotubes. Due to the rapid clearance of the OCN from the blood, the optical absorption in the blood vessels decreased significantly. The differential image in **Figure 2.3.4.1f** is a result of the subtraction of the pre-injection image in **Figure 2.3.4.1a** from the post-injection image in **Figure 2.3.4.1c.** This image depicts the distribution of differential optical absorption in the vascular induced by the exogenous contrast agent. The injection of saline alone was not found to make any distinctive changes in PA signals

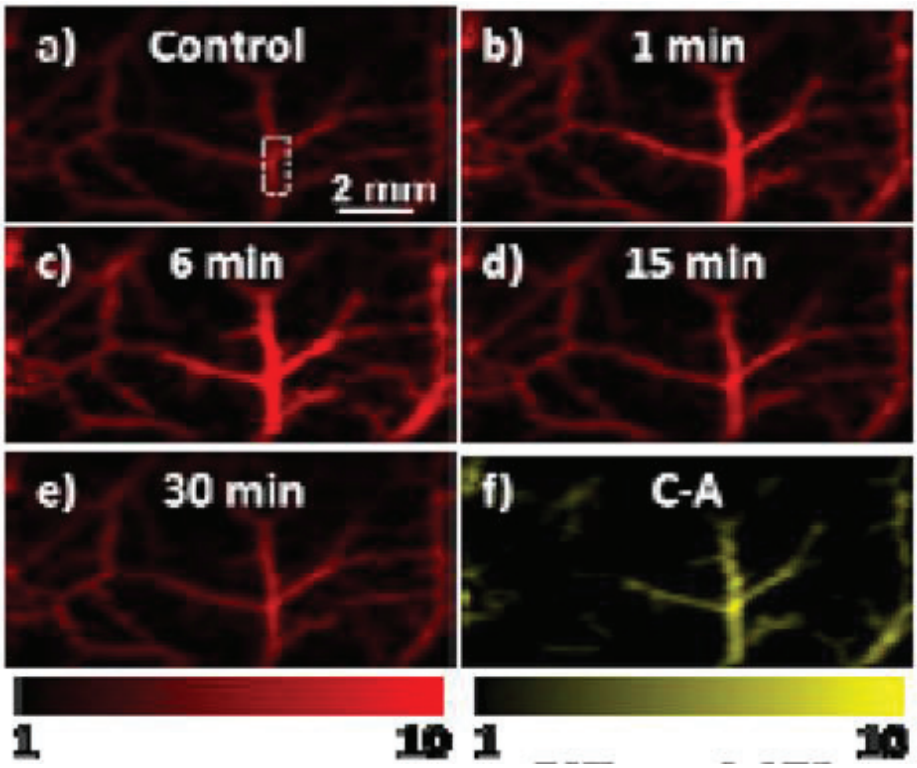

Figure 2.3.4.1 *Noninvasive PA imaging of femoral vasculature of a nude mouse employing carbon nanotubes as contrast agents. The PA signal from the femoral vessels was monitored after NT (25 vol %, 100 µL) was intravenously injected slowly through the tail vein. The laser was tuned to a wavelength of 650 nm. (a) PA MAP image acquired before the injection of OCN. Red parts represent optical absorption from blood vessels. (b)-(e) PA MAP images obtained at 1 (b), 6 (c), 15 (d), and 30 min (e) post-injection of OCN, respectively. Red scale bar corresponds to a)-e); (f) Differential image that was obtained by subtracting the pre-injection image from the post-injection image (Image f = Image c - Image a) [80]*

2.4 Cancer therapy with group IV nanoparticles

That section contains a general description of the methods and examples of group IV nanoparticles used for cancer therapy. Two concepts of the NPs applications for cancer therapy are the utilization of nanoparticles as some kind of sensibilizators. The nanoparticles itself have

low toxicity, but under the excitation (with light, ultrasound, electromagnetic field etc) they can damage the cancer cells. The mechanism of cell damage can vary: some particles produce heat and can burn the tumors, other cause the oxidative stress by the catalyzing the production of reactive oxygen forms, also mechanical vibrations can damage the cancer cells. Other way for the NPs application for cancer therapy is the utilization of the nanoparticles as drug delivery platform. That method may include the idea of controllable drug release under special conditions and targeting of drug – nanoparticle conjugate.

2.4.1 Hyperthermia

One of the most rapidly growing researches of cancer therapy using nanoparticles bases on hyperthermia methods. Hyperthermia (also called thermal therapy or thermotherapy) is a type of cancer treatment in which body tissue is exposed to high temperatures (up to 45^{O}C). Researches have shown that increased temperatures can damage and kill cancer cells, usually with less injury to normal tissues [82]. The 2 main methods of hyperthermia usually used in medicine: it is possible to heat all the body to the temperature close to 45^{o}C or selectively heat the tumor and locally reach significantly higher temperatures without significant damage for surrounding tissues. Both methods have their advantages of disadvantages. The nanoparticles' application for hyperthermia is usually means the second method. In general, the nanoparticles are used as an agent, susceptible to some kind of excitation, which produces the heat.

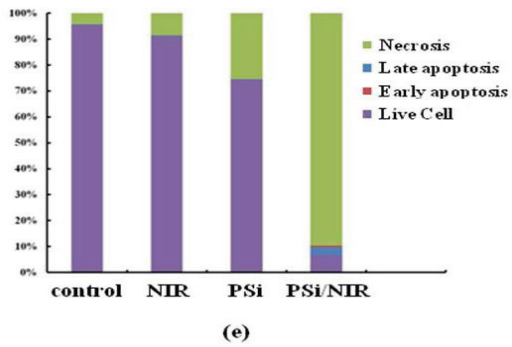

Figure 2.4.1.1: *apoptosis assay results: Flow cytometry profiles represent Annexin-V-FITC Summary of the Annexin V-FITC Apoptosis assay results showing the percentages of cell death modes: necrosis, late apoptosis, early apoptosis, and live cell* [81].

Previously investigated thermal therapies have employed a variety of heat sources including laser light, focused ultrasound and microwaves [83].

Porous silicon can be used for hyperthermia under excitation with NIR laser light [84] or ultrasound [85]. Incorporation of the magnetic particles inside the pores of the porous silicon allows using the alternating magnetic field for heating [86]. Since silicon nanoparticles in form of porous silicon are the easiest to produce and control their properties, all of the hyperthermia tests are made only on porous silicon but not the other types of Si. Both in vitro (**Figure 2.4.1.1**)

and in vivo (**Figure 2.4.1.2**) tests were performed using porous silicon for hyperthermia. The in-vitro cell viability measurements show the increasing amount of the necrotic cells after the combined action of the NIR light irradiation and porous silicon presence (**Figure 2.4.1.2**). An in vivo test on mice shows the absence of the cancer tumor growth in case of combined porous silicon and NIR irradiation action.

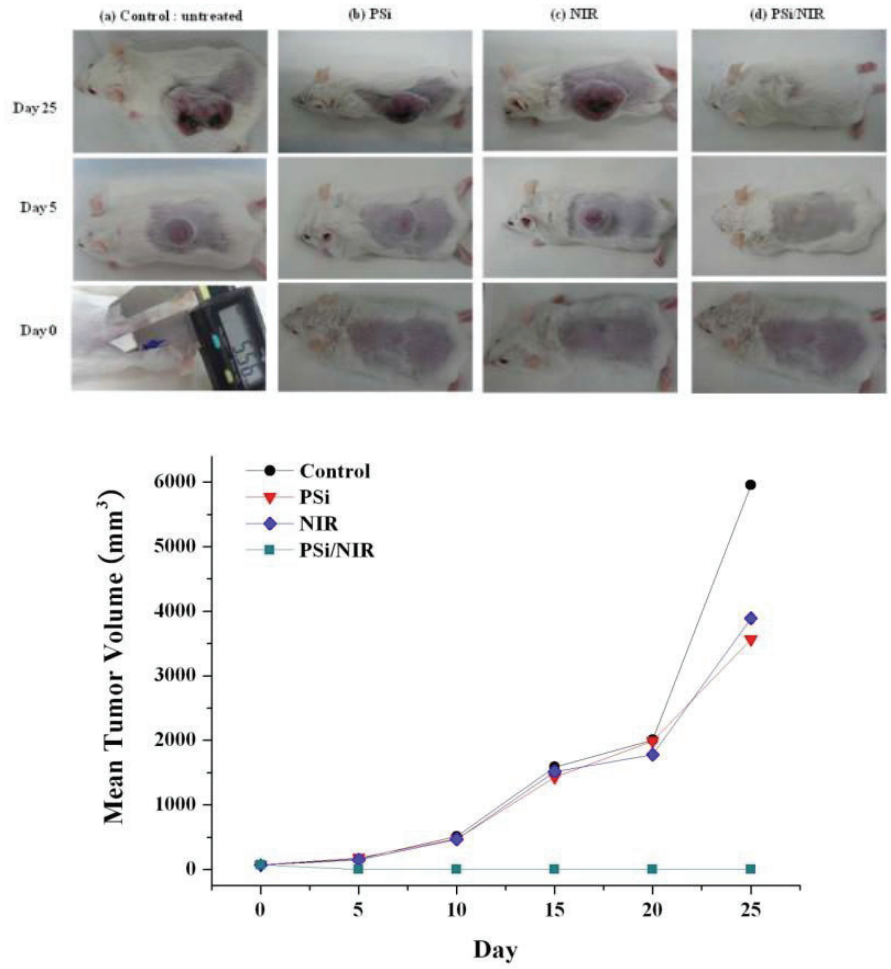

Figure 2.4.1.2: *Change of tumor volume of mice treated with porous silicon and NIR laser during time. Tumor volume CT-26 tumor cell xenografts. Tumor volumes were measured once a week after sample treatments. The group treated with a PSi/EtOH:PEG solution followed by NIR laser treatments (4 times for 2 min at 1.5 W/cm2 each time with a time interval of 2 min) shows efficient tumor growth inhibition compared with other experimental groups. [83]*

Also NIR excitation can be used for heating some composite nanoparticles, consisting of the relatively big silicon particles or wires with gold quantum dots on it. In this case gold absorbs the light and due to energy transfer to the silicon, the heating can occur. **Figure 2.4.1.3** shows

the photothermal effect of silicon-gold composite particles. It is seen that under NIR irradiation, AuNPs@SiNWs solutions showed rapid rise in temperature, whereas water, PBS, and RPMI 1640 medium showed little change in temperature upon NIR laser irradiation.

Due to wide absorbance spectrum, carbon nanotubes and graphene dots also can be used as a sensitizer for thermal therapy under NIR laser irradiation [88, 89]. The irradiation of carbon dots or the nanotubes leads to the heat production and can cause the cell destruction. The example of such effect for carbon dots is shown on **Figure 2.4.1.4.** First graph shows the heating effect, second – the cell viability during the irradiation and third is the images of the cells before and after treatment. Silicon carbide nanoparticles had never been tested as an agent for hyperthermia.

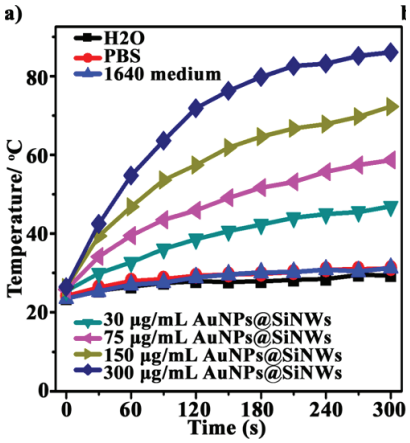

***Figure 2.4.1.3**: Photothermal effect of AuNPs@SiNWs solution showing temperature increase as a function of NIR irradiation (2W/cm2) time and sample concentration. [87]*

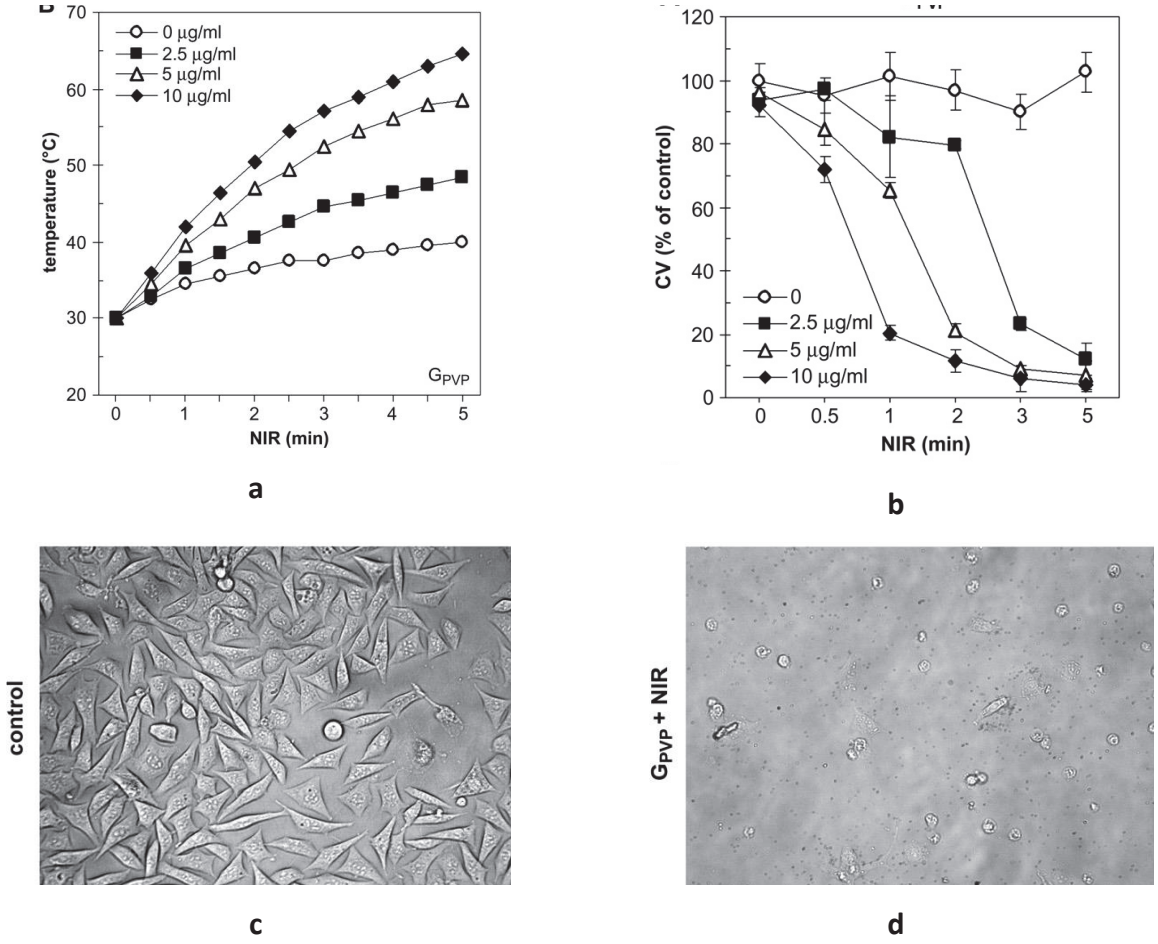

Figure 2.4.1.4 *The carbon dots as a hyperthermia agent: a NIR-induced heat generation. b Photothermal killing of cancer cells c,d - U251 cells before and after treatment with NIR laser. [88]*

2.4.2 Photodynamic therapy

The molecular oxygen O_2 can be presented in several electron states. The ground state $^3O_2$ called triplet oxygen has much lower activity than the excited state – singlet oxygen $^1O_2$ the transition between the states requires energy and due to quantomechanical symmetry principles cannot be excited directly by the irradiation. Nevertheless, some chemical compounds can activate such transition. This kind of excitation of $^1O_2$ is usually known as photosensitization. The preferable material for such kind of photosensitization needs to be able to absorb the light and relax using radiative or non-radiative way in order to transfer part of absorbed energy to oxygen molecule. For the efficient energy transfer, the relaxation through the mechanism of singlet oxygen generation should be preferable over others. That means, the lifetime of the excited state of the material should be long enough in absence of oxygen and significantly shorter in presence of it.

Photodynamic therapy (PDT) can be an effective clinical treatment for certain types of cancer because of its relatively low systemic toxicity and its non-invasive nature. The operational principle for PDT involves the conversion of ground-state molecular oxygen ($^3O_2$) to singlet

oxygen ($^1O_2$) by energy transfer from a photoexcited molecule or particle (a photosensitizer). **Figure 2.4.2.1** shows the energy diagram of the singlet oxygen excitation mechanism. The photosensitizer initially absorbs a photon that excites it to the first excited singlet state and this can relax to the more long lived triplet state. This triplet PS can interact with molecular oxygen in two pathways, type I and type II, leading to the formation of reactive oxygen species (ROS) and singlet oxygen respectively.

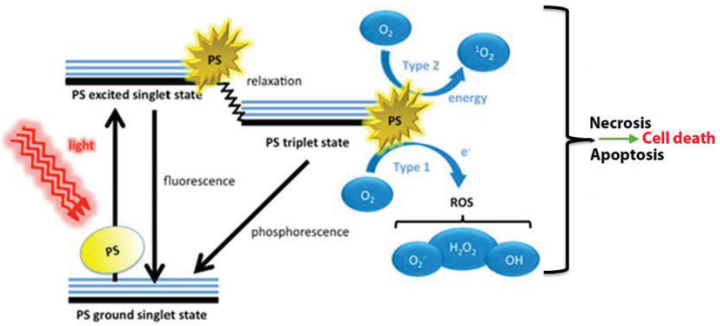

Figure 2.4.2.1: *Schematic illustration of photodynamic therapy including the Jablonski diagram [90].*

The highly reactive $^1O_2$ causes lethal damage to cancer cells and destruction of tumor vasculature. Despite the advantages of the therapy itself, photosensitizers in use today display toxic or other side effects that limit their use. Recent studies using nanoparticle hosts containing conventional organic photosensitizers have demonstrated improved water solubility and biocompatibility. However, most of these approaches use non-functional silica or polymer-based nanomaterials as the carriers, and there is still a risk of the photosensitizer payload leaking from the carriers into the body before reaching the target. Nanomaterials which can intrinsically generate $^1O_2$ when photoexcited could overcome such problems. However, concerns regarding biodegradability, toxicity of degradation by-products and relatively low $^1O_2$ quantum yield of such materials have impeded their clinical application.

According to [91], excitons in nanocrystalline silicon can transfer the energy to molecular oxygen adsorbed on the nc-Si surface. The photosensitization of singlet oxygen by nc-Si is now a subject of numerous studies, because nanoparticles possess several advantages for targeted PDT [92]. The interaction between excitons in nc-Si and O2 results in formation of a singlet oxygen with efficiency several times higher than traditional organic synthesizers [93,94].

Some kinds of carbon nanotubes were found to have weak $^1O_2$ sensitizing effect, which can be only detected by not-direct observations [95].Carbon dots in any form were not found to

be used as photosensitizers for PDT, but they can be conjugated with the organic PDT drugs and used for their delivery [96].

Silicon carbide does not luminesce in near-IR range and it have not any significant interest for using in PDT.

2.4.3 Destruction of cancer due to cavitation effect

Other interesting way for cancer treatment using the group IV nanoparticles is the utilization of the nanoparticles for the mechanical stress generation. For example carbon nanotubes inside the cancer cells under irradiation can generate sound wave (photoacoustic effect) which can destroy the cells [97]. **Figure 2.4.3.1** shows the scheme of the destruction of the cells using photoaccoustic wave.

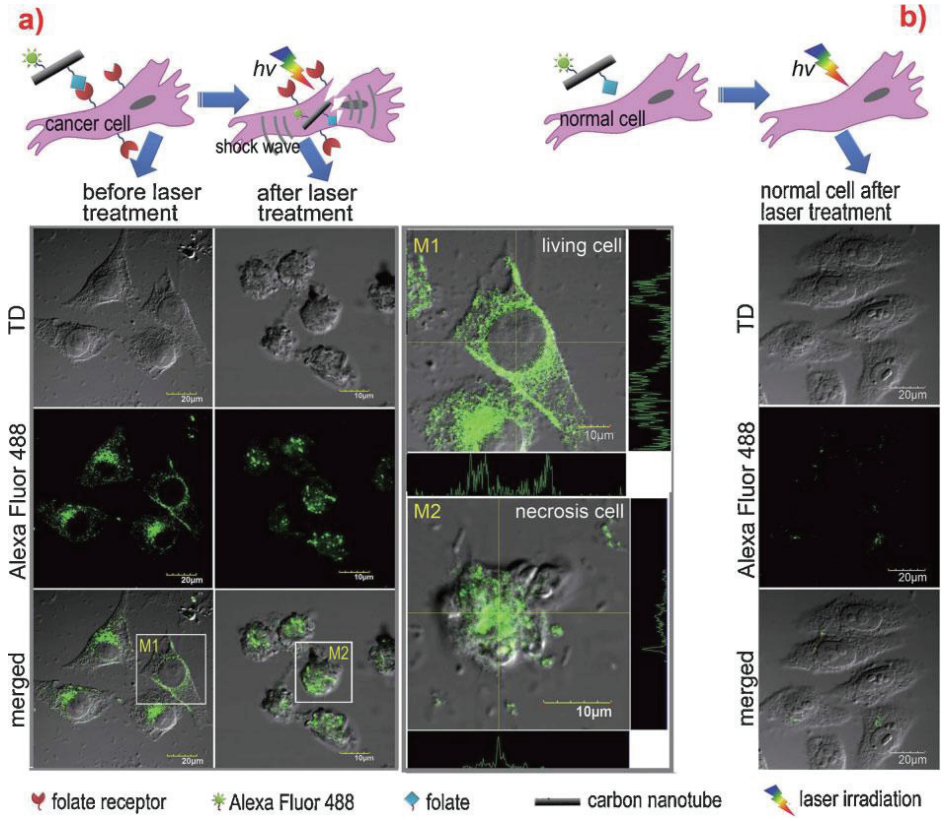

Figure 2.4.3.1 *Targeted destruction of cancer cells by SWNT photoacoustic effect.*

It is seen, that combined action of the nanotubes and laser treatment can cause the complete cell destruction, while neither nanotubes itself nor laser irradiation alone do not produce such effect.

2.4.4 Drug delivery

Other way to treat the cancer with the nanoparticles bases on a drug delivery. The drug delivery concept lies on the construction of multi-purpose agent. There are 2 parts of such agent: first is responsible to the accumulating to the right place of the human organism (in tumor for

cancer treatment) and called vector, other is the drug, which slows down or stops the cancer growth and which is able to kill the tumor cells.

There are 3 main approaches for the construction of drug delivery system:

- First one is the covalent binding of the drug to the nanoparticle. That approach arises from the molecular drug engineering. In this case, the nanoparticle-drug conjugate will work as a new multifunctional agent.
- Second way is the incapsulation of the drug inside the nanoparticle. The shell protects the drug till it will be delivered, so the higher local concentration can be achieved at the target. In this case very important is the drug release kinetics and possibility of the drug release control using outer excitation.
- Third approach is the electrostatic binding – for example, the negative drug is preferable to bound to positively charged nanoparticle. That binding is weak and it is easy to detach the drug. Almost always the electrostatics should be taken in account during the drug load into the porous structure.

Group IV nanoparticles are one of the least toxic inorganic particles, so there are some researches dedicating to the drug delivery using them. Group IV nanoparticles can be engineered as nanoplatforms for effective and targeted delivery of drugs and imaging labels by overcoming the many biological, biophysical, and biomedical barriers.

An emerging theme in porous Si as applied to medicine has been the construction of microparticles (“mother ships”) with sizes on the order of 1–100 μm that can carry a molecular or nanosized payload, typically a drug. With a free volume that can be in excess of 80%, porous Si can carry cargo such as proteins, enzymes, drugs, or genes. [98].

Carbon materials, i.e carbon nanotubes and graphene are widely investigated for the purpose of drug delivery. Their main advantage of carbon nanotubes is that CNTs are chemically inert and there is a lot of ways to bind some drugs to their surface. Depending on the surface modification of the CNT there are several ways to enter the cell [99]. Non-modified CNTs are able to pin the cell membrane and they can be used as nano-needles for delivery [100]. Unfortunately, after pinning the cell, they stuck into the membrane and often cause the cell death. So, despite of the chemical inhercy, they are highly cytotoxic. Nanodiamonds and graphene dots are less cytotoxic and they are very perspective for the drug delivery via chemical coupling due to very flexible and well-known surface chemistry.

Nanodiamond–doxorubicin complexes (ND–Dox) were used to treat drug-resistant breast cancer (4T1) and liver cancer (LT2-M) models. The nanodiamond reduced the capacity of the tumours to expel the doxorubicin, and the circulation half-time of the ND–Dox complexes was found to be 10 times that of unmodified doxorubicin [101]. Both carbon and silicon porous particles could be used as drug carriers for delivery. There is no data about SiC nanoparticles utilization for drug delivery.

2.5 Conclusion of chapter 2

The **Table 2.5.1** shows the information about utilization of the different nanoparticles as labels for different imaging techniques.

Imaging modality	**Si**	**C**	**SiC**
One-photon excited PL	Porous silicon	Carbon dots Nanotubes Graphene Nanodiamonds	SiC nanoparticles
Two-photon excited PL	Porous silicon	Carbon dots	SiC NPs
Raman mapping	-	nanotubes	-
Photoaccoustics	-	Carbon dots nanotubes	-

Table 2.5.1 *The comparison of the nanoparticles by the possibilities of the utilization for imaging.*

Each of the empty cells corresponds to the unknown but potentially interesting application. The silicon carbide had not ever been considered as for 2 photon excited photoluminescence agent since under the same conditions it produces the bright second harmonic signal, which is more suitable for practical applications. The empty cells are the utilization of Silicon nanoparticles as second harmonic agents for imaging. That idea can be promising since theoretical studies show that relatively big (20 nm) Si nanoparticles can effectively produce second harmonic. So, the same idea can be considered also for the carbon particles, in case of carbon NPs that is necessary to have the 20-40 nm particles of well-crystalline carbon (probably diamond-like). The Raman mapping is a sophisticated technique and for bioimaging it needs to presence of specific vibrations of NPs at the spectral range which excludes the coincidences of Raman shifts for NPs and for the organic compounds presented into the cell. The ordinary spectral range for such molecules is 200-3000 cm^{-1}. Other possibility is the utilization of the NPs which yield the Raman signal several orders of magnitude higher than the signal of organics usually presented inside the cell. The CNT have strong Raman signal peak at 1500-1600 cm^{-1} depending on the environment of the CNT. The Si and SiC NPs have the Raman peak at the similar ranges so potentially they can be used as Raman imaging agents.

It is seen that there is a lot of ways for the utilization of group IV nanoparticles for different kinds of optical imaging. Despite of the great biocompatibility and low cytotoxicity, there are some approaches for several NPs are not well-studied.

Group IV nanoparticles as agents for sensibilisation could be used in different ways. There is a large number **of** cancer therapy methods with the NPs used as sensibiliztion agents. The NPs can be used for different kinds of hyperthermia, photoaccoustic and photodynamic therapy.

The group IV nanoparticles fit such application since their biocompatibility and low toxicity. Since the big particles (more than 100 nm) under ultrasound treatment cause the heating, the smaller particles should be used for the mechanical motion effect examination.

Despite the huge amount of studies concerning the utilization of the goup IV NPs as sensibilizators and drug carriers, the effect of “bare” nanoparticles, nanoparticles without modification or any extra excitation is not well – studied. Nevertheless, nanoparticles itself can be selectively absorbed by some kinds of tumors.

3. Materials and methods

3.1 Methods used for nanoparticles characterization

That section describes the main physical principles of the methods used for the characterization of the nanoparticles in the current work. The basic information about the photoluminescence, the dynamic light scattering and scanning microscopy is given in this section. Also there is a description of the setups and equipment used for such measurements into the current research.

3.1.1 Size distribution analysis

The size distribution of the nanoparticles in form of colloids can be obtained by the dynamic light scattering method (DLS). It bases on the next principles: A monochromatic light source, usually a laser is shot through a polarizer and into a sample. The scattered light then goes through a second polarizer where it is collected by a photomultiplier.

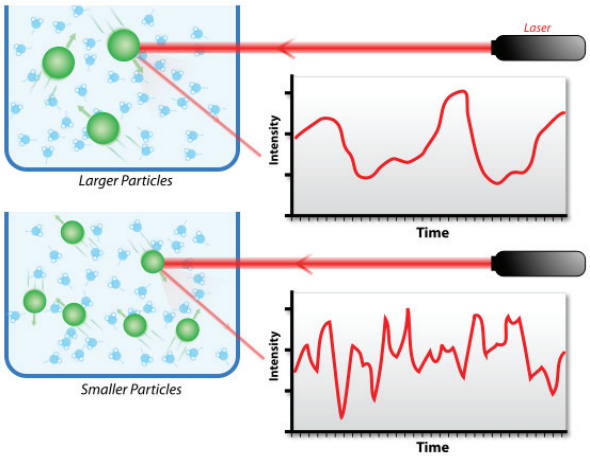

Figure 3.1.1.1: *Hypothetical dynamic light scattering of two samples: Larger particles on the top and smaller particles on the bottom [102]*

All of the particles in the solution are being hit with the light and all of the molecules diffract the light in all directions. The diffracted light from all of the particles can either interfere constructively (light regions) or destructively (dark regions). This process is repeated at short time intervals and the resulting set of speckle patterns are analyzed by an autocorrelator that compares the intensity of light at each spot over time.

When light hits small particles, the light scatters in all directions (Rayleigh scattering) as long as the particles are small compared to the wavelength (below 250 nm). If the light source is a laser, and thus is monochromatic and coherent, the scattering intensity fluctuates over time. This fluctuation is due to the fact that the small molecules in solutions are undergoing Brownian motion, and so the distance between the scatterers in the solution is constantly changing with time. This scattered light then undergoes either constructive or destructive interference by the surrounding particles, and within this intensity fluctuation, information is contained about the time scale of movement of the scatterers. In general, the smaller are the particles, the more frequent are the changes into the scattered signal (**Figure 3.1.1.1**). The quantative alalysis of the

intensity-time dependences is possible in terms of autocorrelation function. The autocorrelation function is

$$G(\tau) = \lim_{T\to\infty}\left(\frac{1}{T}\int_0^T I(t) * I(t+\tau)dt\right)$$

That function shows the correlation between the intensities at the times differ at τ. In case of correlation function close to 1 means the passing of single particle through the beam. Zero – time of passing of several particles through beam. The time of the nanoparticles passing through the beam allows the calculation of the size distribution of the samples.

The DLS method is acceptable for the measurement of the dispersed particles with size from 0.1 nm to 10um. Nevrtheless, it has quiet low resolution (the relative size observation error may reach 30%). Other problem is that the small quantity of small size particles can easily be "hidden" in a much larger quantity of large size particles. So, the measurement givus us disproportionally information in case of relatively big particles.

DLS measurements were performed using zetasizer z-nano equipement. Dynamic light scattering (also known as photon correlation spectroscopy or quasi-elastic light scattering) is a technique in physics that can be used to determine the size distribution profile of small particles in suspension or polymers in solution.

3.1.2 Zeta potential analysis

It is also possible to estimate z-potential of the particles using the same setup. Every particle can bind some solvent molecules which will preferentially move with the particle. The slipping plane is a relative to a point in the bulk fluid away from the interface.

Z-potential is a potential of the slipping plane. Since the particle moves with the "shell", (**Figure 3.1.2.1)** the potential of such shell is vital for behavior under application of electrical field. The positively charged nanoparticles will move along the electric field, the negative ones – in opposite direction. The value of potential and the liquid viscosity will define the speed of such particle under electric field. Under application of alternating electrical field and measurement the nanoparticles' average speed in such conditions by DLS, z-potential can be measured.

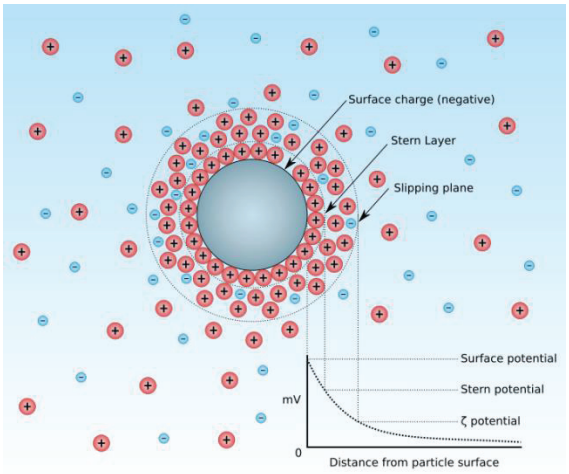

Figure 3.1.2.1: *diagram showing the ionic concentration and potential difference as a function of distance from the charged surface of a particle suspended in a dispersion medium.[103]*

High Z-potential is an important characteristic for the colloid solution stability. Colloids with high zeta potential (negative or positive) are electrically stabilized while colloids with low zeta potentials tend to coagulate or flocculate as outlined in the **Table 3.1.2.1**[104].

Zeta potential [mV]	**Stability behavior of the colloid**
from 0 to ±5,	Rapid coagulation or flocculation
from ±10 to ±30	Incipient instability
from ±30 to ±40	Moderate stability
from ±40 to ±60	Good stability
more than ±61	Excellent stability

Table 3.1.2.1: *The table showing colloidal suspension electrostatic stability characteristics.*

For zeta potential measurements Zetasizer Nano Z zeta potential analyzer had been used. All the measurements were applied at 22^0 C in water solution. The zetameter is able to measure the sizes from 3.8 nm up to 100 microns ad zeta potential in range from -250 mV to +250 mV [105]

3.1.3 X-ray diffraction

The XRD technique is one of the most commonly used for inorganic material analysis. The X-rays can interact with the electrons into the crystal. The electrons are worked as a re-emitter of the x-ray not only into the direction of initial wave, but also in all the other sidections. Since the wavelength of the x-rays (usually about 1.5 angstroms) is close to the lattice parameter for most of inorganic crystals, (several angstroms) it is possible to observe the diffraction of the waves refracted by the different atomic layers of the crystal. In case of monocrystals, using the information about the diffraction peaks positions and intensity, it is possible to reconstruct electronic density map of the cell. In case of powder diffraction, used in this research, it is possible to estimate the parameters of the crystal cell, (symmetry and size). But the other method is just comparison of the XRD with the already existing patterns for most of materials in order to estimate the presence of the phase. The width of the peaks depends on several parameters: x-rays may be non-monochromatic, some equipement parameters and the sample parameters, such as irregularities due to thermal motion or presence of defects. But in case of crystallites smaller than 200 nm, the dominating parameter which is responsible for the peaks width is a crystallite size. The dependence of the peak shape and crystallite size was found by Paul Scherrer in 1912:

$$D = \frac{k\lambda}{FWHMcos\theta}$$

D is a crystallite size, λ is a x-ray wavelength, θ is a diffraction angle, FWHM is a Full width at half maximum – parameter of the peak width. k is a dimensionless shape factor, with a value close to unity. The shape factor has a typical value of about 0.9 for spherical particles, but varies with the actual shape of the crystallite. The XRD in the currend work were used for the comparison of the NPs crystallic structure with the crystallic structure of bulk material and estimate the size of crystallites.

The x-ray diffraction experiments were performed using Cu k aloha x-ray source (0.15418 nm), SmartLab diffractometer at the nanoparticles dried powders.

3.1.4 AFM

Surface topology of the planar nanostructures can be measured by atomic force microscopy (AFM), whose schematic diagram is presented in **Figure 3.1.4.1**.

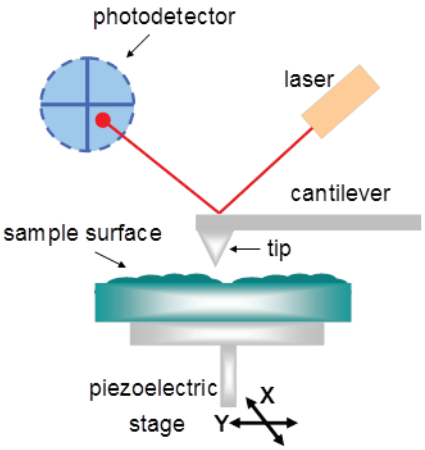

Figure 3.1.4.1: *Functional principle of AFM*

In this technique, the tip attached to a cantilever sweeps the surface of the material to be studied, following the relief. The cantilever may be deflected under the action of different types of forces, such as Van der Waals, electrostatic, magnetic, etc. The relative position of the tip to the surface is measured by a position-sensitive photodetector detecting a laser beam reflected by the cantilever carrying the tip. Through a piezoelectric ceramic, tip-cantilever system can be moved along the X and Y directions (in the plane of the sample) and Z (perpendicularly to the sample). Mapping the position of the tip gives precisely the probed surface topography.

On some systems, the movement in the XY plane is through the sample and not by the tip-cantilever system. Lateral resolution of AFM is determined by the tip curvature radius, while the vertical resolution is of the order of angstrom: one can easily visualize atomic steps on a clean surface. Viewable surface depends on the piezoelectric ceramic, and can range from hundred nanometers to about 150 microns. The AFM is suitable to any surface, including the insulating surfaces. The AFM also offers the possibility to browse the surface without touching it (non-contact method), or by intermittent contact (tapping mode), to limit the possible damage of a fragile samples.

AFM images were acquired by commercially available Digital 3100 (DI 3100) apparatus.

3.1.5 Electron microscopy

In electron microscopy (EM), operating principles are the same as in optical microscopy, but are based on electrons instead of light. Electron microscopes have a greater resolving power than a light-powered optical microscope, because electrons have wavelengths about 100,000 times shorter than visible light (photons), and can theoretically achieve better than 50 pm resolution, whereas ordinary, non-confocal light microscopes are limited by diffraction to about 200 nm resolution.

Images in EM are obtained by the focused electron beam, which illuminate the surface of the sample. Pictures can be seen in many ways - in rays which passed through the object, the reflected rays, by registering secondary electrons or X-rays. Focusing the beam of electrons is ensured by means of electrostatic or electromagnetic lenses as the lenses of the optical microscope.

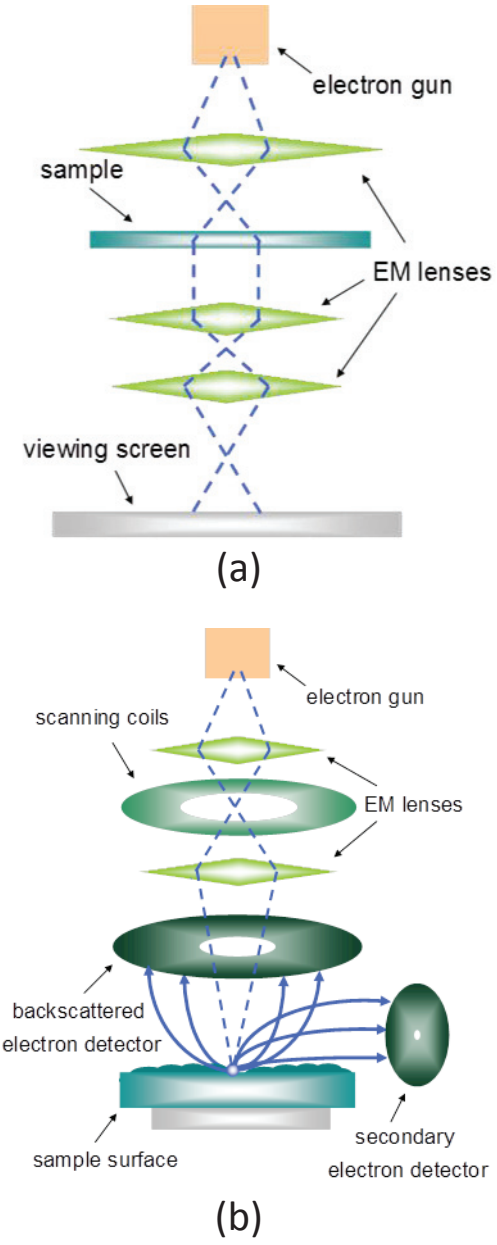

Figure 3.1.5.1: *Function principle of (a) TEM, and (b) SEM*

The schematic principle of TEM is shown in **Figure 3.1.5.1a**. The system consists of a vacuum chamber where the electrons are emitted by an electron gun. The electrons are accelerated in the barrel by a high voltage, which defines associated wavelength of the electrons. A second magnetic lens system is used to enlarge the image obtained. The final image, magnified about 10,000 times, is formed in the observation chamber on a fluorescent screen that can be observed visually. When the electron beam passes through the sample, a very large proportion of electrons is transmitted directly, this provides an interpretable image of the specimen.

Unlike the TEM, where electrons of the high voltage beam carry the image of the sample, the electron beam of the scanning electron microscope (SEM) carry only part of it. The

SEM produces images by probing the specimen with a focused electron beam that is scanned across a rectangular area of the specimen. The general principle of SEM operation is illustrated in **Figure 3.1.5.1b**. As in the TEM, the system consists of a vacuum chamber where the electrons are emitted by an electron gun. Deflection coils of X and Y move the electronic beam over the surface of the sample (XY plane). The primary electrons from the electron gun strike the surface of the sample. Some electrons are scattered elastically (high-energy backscattered electrons), while others, during the impact give part of their kinetic energy to the atoms, causing ionization and ejection of low-energy secondary electrons. The ionized atoms can decay by light emission (cathodoluminescence) or X-ray emission. The backscattered and secondary electrons emitted by the sample are collected by selective detectors. The image displayed by an SEM represent the surface morphology of the sample by corresponding variable intensity of signals from the detectors with the position of the beam on the specimen when the signal was generated. Despite the fact that the image resolution of an SEM is about an order of magnitude poorer than that of a TEM, SEM is able to image bulk samples and relying on surface processes rather than transmission can produce images that are good representations of the three-dimensional shape of the sample.

TEM pictures were obtained by EM-002B (Topcon, Japan) high-resolution transmission electron microscope operating at 200 kV. SEM observations were performed by means of SEM (Tescan, Czech Republic) or Inspect S50 (FEI, USA).

3.1.6 Steady-state and time-resolved PL

The materials are able to absorb the energy from different sources: electromagnetic waves, chemical reactions, interaction with the electrons etc. After the energy absorption, the material turns into the excited state with the excitation of the extra energy in form of photons.

According to the Jablonsky diagram (**Figure 3.1.6.1**), there is 3 steps in luminescence. 1^{st} is a absorption of the photon with the energy E_{ex} from the light source (laser o lamp). That step is relatively short and lasts about 10^{-8} – 10^{-10}s during that time, the system get the conformational changes and react with the environment.

The fluorescence lifetime is an important parameter for practical applications of fluorescence such as fluorescence resonance energy transfer and Fluorescence-lifetime imaging microscopy. The semiconducting, such as QDs are usually have longer lifetimes, about tenth of nanoseconds. The indirect band gap porous silicon had the lifetime about several microseconds. So, using the luminescence kinetics it is also possible to propose the mechanism of the luminescence origin.

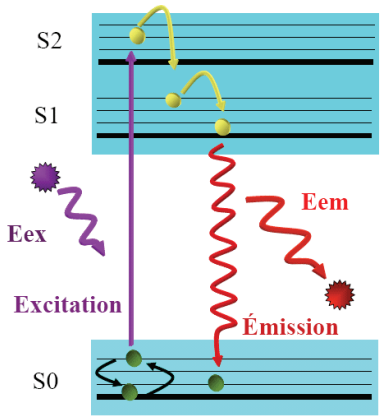

Figure 3.1.6.1: *Jablonski diagram*

All the photoluminescence characterization that have been done for this research were done at the INL facility at INSA Lyon The spectro-fluorimeter was used for such experiment is a commercially available PTI Fluoresence System (FeliX), which scheme is shown on **Figure 3.1.6.2.** The source of the light is a xenon lamp. The light produced by the lamp (1) crosses the adjustable windows (2) and monochromator for choosing the estimated excitation wavelength (3). The selected wavelength light enters the sample zone (4). The higher harmonics of the light can be cut off by the filters (5). The light is focused on the sample by the optical system (7), which also allows the emitted light to pass to the shutter (9) emitted light monochromator (10) and detector (11). For the protection the sample zone is covered by the lid (6). The system is connected to the PC and operated by the FeliX software, which can allow to choose the measurement type, excitation and emission measured wavelength, the step during spectra measurements, integration times and other parameters.

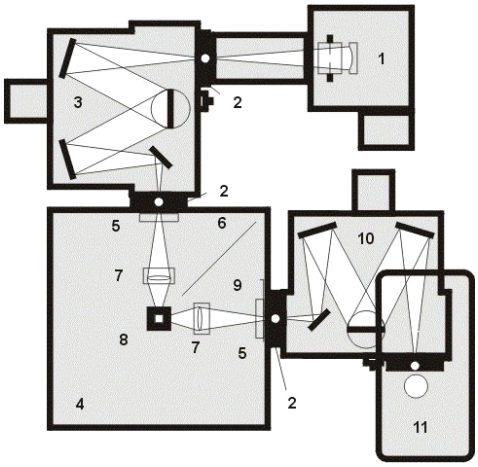

Figure 3.1.6.2: *spectrofluorometer PTI Fluorescence System (FeliX).*

3.2 Protocols and methods of NPs-cellular activity measurements.

That section contains the information about the protocols of cell growth and preparation and about equipement and techniques used for the toxicity tests and imaging.

3.2.1 Luminescent microscopy

A fluorescence microscope is an optical microscope that uses fluorescence and phosphorescence instead of, or in addition to, reflection and absorption to study properties of organic or inorganic substances. The "fluorescence microscope" refers to any microscope that uses fluorescence to generate an image, whether it is a more simple set up like an

epifluorescence microscope, or a more complicated design such as a confocal microscope, which uses optical sectioning to get better resolution of the fluorescent image.

The specimen is illuminated with light of a specific wavelength (or wavelengths) which is absorbed by the fluorophores, causing them to emit light of longer wavelengths (i.e., of a different color than the absorbed light). The illumination light is separated from the much weaker emitted fluorescence through the use of a spectral emission filter. Typical components of a fluorescence microscope are a light source (xenon arc lamp or mercury-vapor lamp are common; more advanced forms are high-power LEDs and lasers), the excitation filter, the dichroic mirror (or dichroic beamsplitter), and the emission filter. The filters and the dichroic are chosen to match the spectral excitation and emission characteristics of the fluorophore used to label the specimen. In this manner, the distribution of a single fluorophore (color) is imaged at a time. Multi-color images of several types of fluorophores must be composed by combining several single-color images:

Most fluorescence microscopes in use are epifluorescence microscopes, where excitation of the fluorophore and detection of the fluorescence are done through the same light path (i.e. through the objective). These microscopes are widely used in biology and are the basis for more advanced microscope designs, such as the confocal microscope and the total internal reflection fluorescence microscope.

The luminescent microscopy images were obtained by means of Leica DMI 4000B microscope with the following filter combination: UV/violet excitation band: 354 – 424 nm and observation spectral range: >470 nm. The multicolored images obtained used the next ex/emission filters: 379-401/435-485nm for blue color, 400-418/ 478-495 nm filters for green color, and 530-560/ 573-648 nm for the red one.

The images of alive cells and were performed in PBS using Cytation 3 cell imaging multi-mode microplate reader. The temperature during measurements remained 37^{o} C.

Cells were seeded at low density on glass coverslips at 12 well plates. After growing for 48 h, the nanoparticles were added. Cells were fixed with ethanol for PL microscopy examination.

3.2.2 Second harmonic generation and two-photon excited microscopy

Multiphoton microscopy is well suited for high-resolution imaging of intrinsic molecular signals in living specimens. It provides convenient excitation of the characteristic UV absorption bands of intrinsic fluorophores using IR illumination, leaving a broad uninterrupted spectral region for efficient multicolor fluorescence collection. The ability of multiphoton

microscopy to produce images deep in optically thick preparations is crucial for intravital tissue microscopy. In addition, second harmonic generation (SHG) enables direct imaging of anisotropic biological structures possessing large hyperpolarisabilities, such as collagen. Signal on that technique depends on the second power of the excitation light intensity, so requires intense excitation in order to reach the best signal/noise ratio. The non-linear dependence on excitation also gives a great potential to improve the spatial resolution by the focusing the excitation light beam on the sample. Second harmonic generation of the material is possible only in case of non-linear response of induced polarization. These imaging modalities are easy to implement simultaneously and differ only in optical filterselection and detector placement.

SHG requires intense laser light passing through a material with a non-centrosymmetric molecular structure. Second-harmonic light emerging from an SHG material is exactly half the wavelength (frequency doubled) of the light entering the material. While two-photon-excited fluorescence (TPEF) is also a two photon process, TPEF loses some energy during the relaxation of the excited state, and SHG is energy conserving. Though SHG requires a material to have specific molecular orientation in order for the incident light to be frequency doubled, some biological materials can be highly polarizable, and assemble into fairly ordered, large non-centrosymmetric structures. Biological materials such as collagen, microtubules, and muscle myosin can produce SHG signals [106]. Nevertheless. The efficiency of generation in solid state nanoparticles is hundred times higher, then for organic compounds.

Since bulk silicon has diamond-like (centrosymmetrical) crystalline structure, it is not able to generate second harmonic signal. Nevertheless, in form of nanoparticles, the surface effects can lead to non-linear response of polarization. There are some researches concerning to the possibility of the usage of Silicon nanocrystalls as a 2-photon excited fluorescent microscopy with small nanoparticles (crystallite sizes are about 4 nm), but no second harmonic signal was observed [107].It was also found that small 2 nm crystallites of silicon are able to generate the weak second harmonic signal [108].Theoretical studies [109] show, that in case of bigger particles (about 20 nm), the SH signal should increase several orders compared to the 2nm ones. So, the Si nanoparticles can be used for SH imaging. The main criterion of the signal intensity is a size of particles.

According to the wurtzite (non centrosymmetric) crystalline structure of cubic silicon carbide, it is popular material for SHG both in bulk form and in form of nanoparticles, so there is a lot of works on this topic of SHG by SiC. Silicon carbide particles are able to generate

remarkable strong SH signal under IR laser irradiation [110]. So, the relatively big Si and SiC NPs can be used as SHG imaging agents.

The SHG pattern is mainly determined by the phase matching condition. A common setup for an SHG imaging system will have a laser scanning microscope with a titanium sapphire mode-locked laser as the excitation source. The SHG signal is propagated in the forward direction.

For optical nonlinear imaging we employed a Nikon A1R multiphoton upright microscope (NIE-Nikon) coupled with an Insight Deepsee tunable laser oscillator (Spectra-Physics, 120 fs, 80 MHz, 680 - 1300 nm). The nonlinear signals were epi-collected by a Nikon 25 water immersion objective (CFI75 APO, N.A.1.1) spectrally filtered by tailored pairs of dichroic mirrors and interference filters and acquired in parallel either by a normal photomultiplier (600 - 655 nm) or a GaAsP photomultiplier (385 - 492 nm).

3.2.3 Impedance-based cell number measurements (xCelligence)

Cell number measurements were performed using non-destructive impedance-based method (xCELLigence). The cells were grown on special plate with electrodes on its bottom. The system measures electrical impedance across interdigitated microelectrodes situated at the bottom of culture wells. The measurements are done by applying an alternative excitation signal (20 mV control voltage amplitude) at three different frequencies (10, 25 and 50 kHz) through the microelectrodes in the E-plates while monitoring the voltage drop across the electrodes where the quotient voltage/current yields the impedance Software shows cell index as a result of processing impedance data as a time function. Cell index is proportional to the cell number, single cell surface area and adhesion factor. The scheme of the setup work is shown on **Figure 3.2.3.1.**

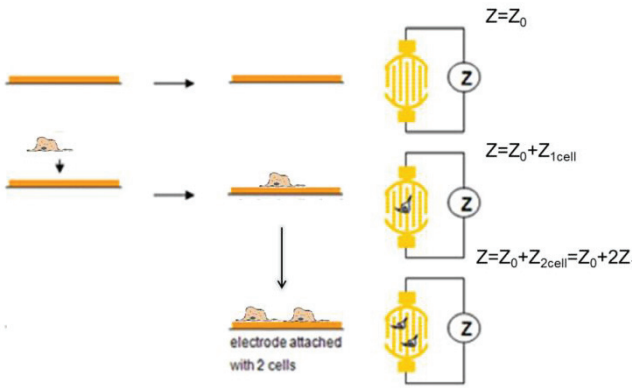

Figure 3.2.3.1: *the scheme of the xCelligence setup principle [111]*

For a given cell line under basal conditions, cell number is the main factor affecting cell index. Doubling time and cell index slopes on normalized curves were measured to compare the

effects of increasing concentrations of SiC on the proliferation speed of different cell lines. Each curve is the mean of cell index measured on 8 wells.

Usually in case of cytotoxicity tests the parameters are chosen for the toxicity are the cell viability in percent for the estimated concentration of NPs and the exposure time. Other way to measure cytotoxicity is to check the concentration, which kills the defined part of the cells (i.e LD50 parameter shows the concentration causes 50 % cell death) during estimated time. In general, there are 3 correlated parameters: the concentration of the toxic reagent, time of exposure and the number of the dead cells.

The presence of 3 parameters, 2 of which are independent from the third makes the all toxicity measurements strongly protocol-dependent. For example, the estimated LD 50 value will be the true only for the definite exposure time. If we are measuring the exposure time for which the toxic effect will be evident, we should choose both concentration of the reagent and the criteria of "evidence" of toxicity (how much cells should be dead).

If we got the cell number evolution curves for the different concentration of particles, it is possible to get from this data all of abovementioned toxicity parameters. It is possible to have an information of number of cells on any desirable time and concentration, so the raw xCELLigence data gives much more information, than any of the other toxicity parameters.

The real time proliferation measurement allows solving the problem of such protocol standardization. Nevertheless, for the proper comparison it is more convenient to get only 1 value that indicates the toxicity of Nps. In the current research I use the term "toxic dose" which shows the minimal concentration which causes cell death. It can be seen at the xCelligence graphs as a negative cell index slope.

An example of cell proliferation test is shown at the **Figure 3.2.3.1.** We can see 2 curves with cell index value, representing the cell proliferation dynamics. The cells are growing and there is no significant change in cell proliferation behavior until the 48h. After the 48 hours of proliferation, some nanoparticles in toxic concentration had been added at some samples. After the NPs addition, we can see the decrease of the cell index, while the control sample proliferation rate remains unchanged.

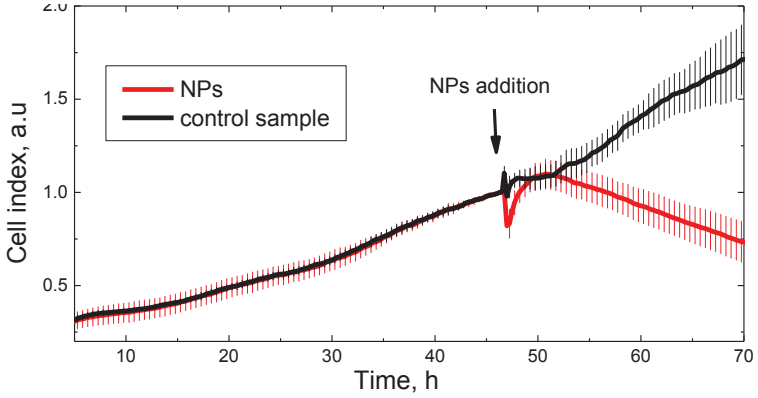

Figure 3.2.3.1 *The cell index evolution curves for 3T3-L1 cells. The time of nanoparticles addition is 48 h*

3.2.4 Bioimaging measurements statistics and cell coloring protocol

All cell lines were initially grown in flasks containing Dulbecco's modified Eagle's medium supplemented with 10% newborn calf serum 100 IU penicillin, 100 µg streptomycin, and 0.25 µg/mL amphotericin B at 37°C in a water saturated atmosphere with 5% CO2 in air, in a Heraeus incubator. Cells were trypsinized by 0.05% trypsin. Cells concentrations were measured using Sceptor pipet (Millipore). Cells were seeded at 2500 per well in a 96 wells plate – RTCA xCelligence plate for cell proliferation measurements. The same concentration of cells was seeded on quartz glass coverslips for photo acquisition. For cell toxicity experiments the 3T3-L1, HuH7, Panc1, HSC, HepG2 and Hek 293 cell lines were chosen. 3T3-L1 and HEK293 are non-cancer cells while other cell lines are cancer cell lines. During the first 48 h cells were growing under basal conditions into the cell medium inside the xCelligence setup. Then the nanoparticles were added to cell cultures for 24 h at the concentrations 1.5, 1, 0.5, 0.25 and 0.1 mg/mL of culture medium. After that, particles were washed out and replaced by fresh culture medium. Cell proliferation rates were measured over the 24 hours following after washing out the NPs.

4 Synthesis and characterization of the nanoparticles

That chapter describes the synthesis method and characterizes the most important for the current research physical properties. Generally, there are 3 subdivisions for each kind of NPs. First subdivision is the method and conditions of the synthesis. Second is a structural characterization of the nanoparticles – it contains the data about the NPs size, crystallinity and agglomeration ability. The last subdivision summarizes the properties of nanoparticles, which are interesting for current research. Usually, it is photoluminescent characteristics and second harmonic generation ability.

4.1 Porous silicon

Synthesis

The layers of anodized porous silicon were formed by standard electrochemical etching into the Teflon cell with the platinum counter electrode. The HF-EtOH –OH solution has been used as an electrolyte. The working electrode was the bulk monocrystalline silicon wafer. The scheme of the etching setup is shown on the **Figure 4.1.1.**

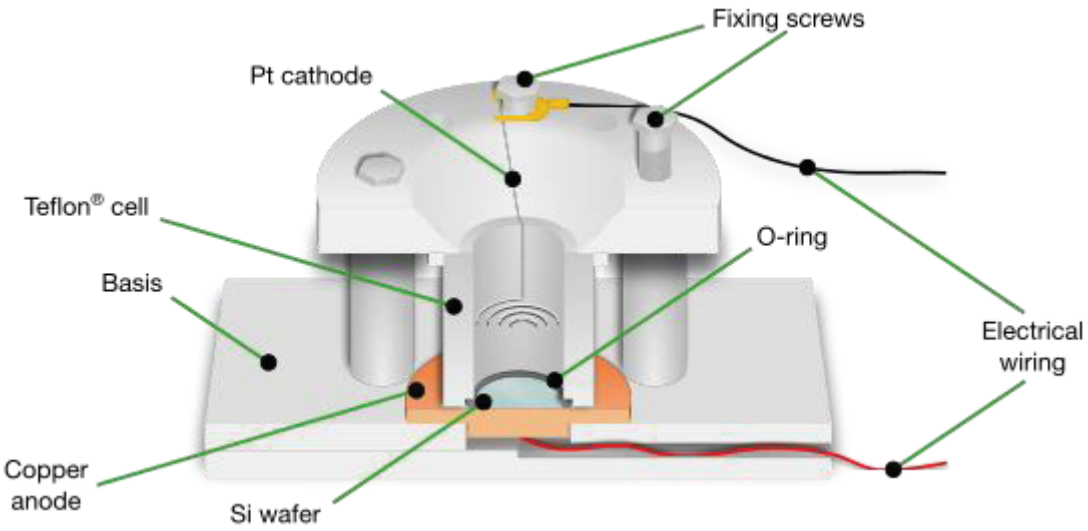

Figure 4.1.1: *The experimental setup for porous silicon production*

During the etching process the next electrochemical reactions are appeared on the silicon wafer anode:

$$6F^- + Si \rightarrow SiF_6^{2-} + 4\bar{e}$$

And on Pt cathode:

$$2H^+ + 2\bar{e} \rightarrow H_2$$

Porous silicon films were prepared by electrochemical etching of boron-doped (100) c-Si wafers (specific resistivity of 12 Ohm*cm) in a mixture of HF (48%):C_2H_5OH (1:1) under etching current density 60 mA/cm2 for 40 min. The etching was done in a Teflon cell with a platinum counter electrode at room temperature.

In order to obtain free-standing PSi films, a short pulse of the etching current approximately 600 mA/cm^2 was applied. The free-standing films were rinsed in deionized water and dried in air.

Structure

As a result, porous silicon layer had been obtained. According to the literature data [112], the abovementioned method leads to the silicon layer with the complicated porous structure with lots of small crystallites, bound together. The porous silicon was hand grinded for 10 minutes. The resulted powder was used for further experiments and x-ray diffraction analysis. XRD studies of the powder (**Figure 4.1.2**) shows that crystallite size, which can be calculated from the half-width of the peaks using Scherrer equation, is close to 3.0±0.8 nm; Sharp peaks correspond to the little amount of crystalline (not nano) Si phase left. That can be the traces of the wafer.

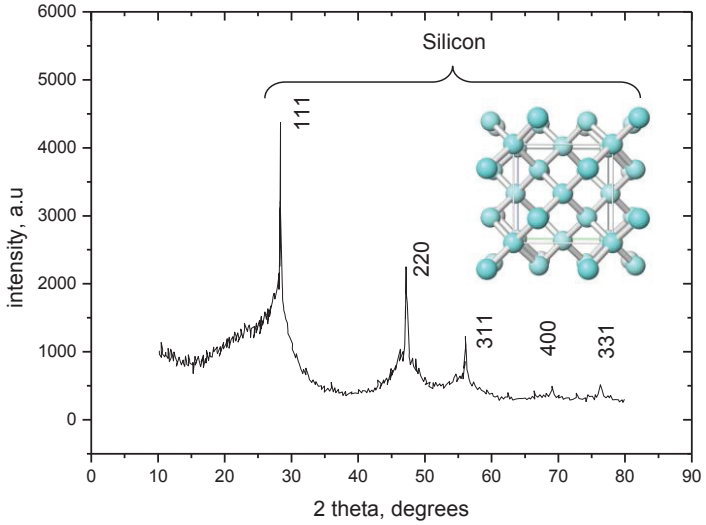

Figure 4.1.2: *the XRD pattern of the porous silicon powder. The XRD peak position corresponds to the bulk silicon structure (inset)*

After dissolution of porous layer in water and sonication into ultrasonic bath for better dispersion, it was possible to reach the particles with average size is about 100 nm (**Figure 4.1.3**)

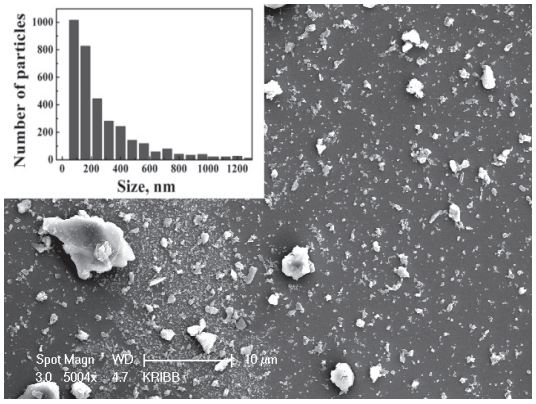

Figure 4.1.4: *SEM images of porous silicon powder after dispersion in water*

DLS measurements also confirm that we got 100 nm-sized agglomerates (**Figure 4.1.3**).

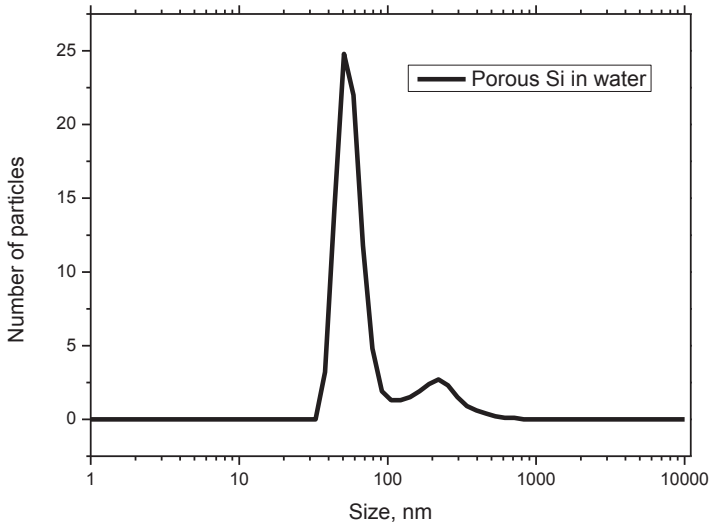

Figure 4.1.4: *size distribution of the nanoparticles' number obtained using the DLS of water suspensions of porous silicon powder.*

All of the tests allows to propose that porous silicon samples used for the experiments are the small crystallites (3-4nm), agglomerated into the bigger (about 100 nm) particles, which do not separate in water solutions.

Properties

Unlike to the bulk silicon, porous silicon has bright photoluminescence under UV or green excitation. The photoluminescent spectrum of porous silicon under 511 nm excitation is on the **Figure 4.1.5.**

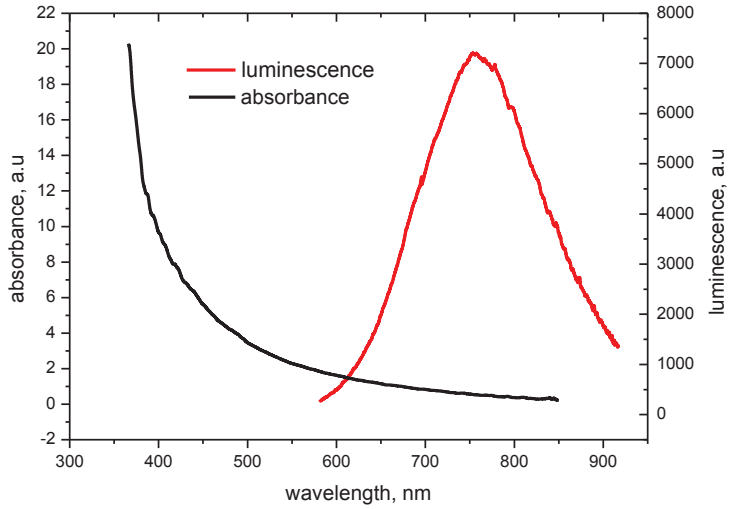

Figure 4.1.5: *the photoluminescence (red) and absorbance (black) spectra of the porous silicon*

The maximum of its luminescence is in the near-IR range (760 nm), but since this spectrum is relatively wide, the light in visible orange-red spectral range can be easily detected. Such wide peak shape concerned to the presence of crystallites with different sizes in porous silicon. After the exciting pulse, the luminescence intensity decreases during relatively long time – 20-30 microseconds depending on the emission wavelength. It also can be seen that relaxation time depends on measured the emission wavelength (**Figure 4.1.6**). Such fact can be described by the different behavior of the particles with different sizes. The bigger ones have less surface defects which can be used for radiative exciton recombination. Also such long relaxation times can be caused indirect bandgap in the bulk silicon and, as a result impossibility of intergap mechanism of recombination.

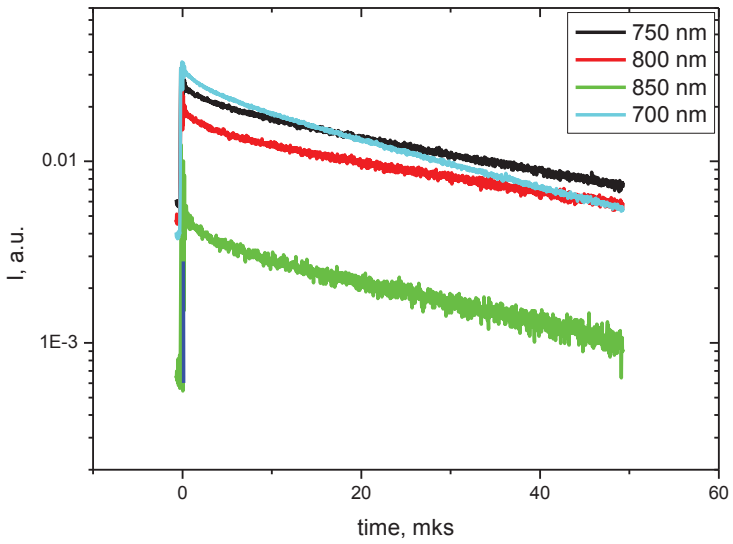

Figure 4.1.6: *The luminescence kinetics for porous silicon and different emission wavelengths. Excitation wavelength – 337 nm (pulsed nitrogen laser)*

4.2 NanoSilicon

Synthesis

The silicon nanoparticles were obtained by and laser ablation of Si in water. Samples of the silicon nanocrystals were prepared by the laser fragmentation of the microcrystallic silicon dispersed in the deionized water after 3h of degasation under Ar flow. The fragmentation of the solution were performed during the 1 h using Ti-saphire laser with 800nm wavelength. The pulse duration was 130 fs, pulse energy – 300 μJ, The pulse frequency was 1000 Hz. Laser irradiation was focused with the lens into the cuvette center. During the fragmentation, solution was stirred with a magnetic stirrer.

Structure

After production, we got well-crystallized spherical nanoparticles (TEM at **Figure 4.2.1**)

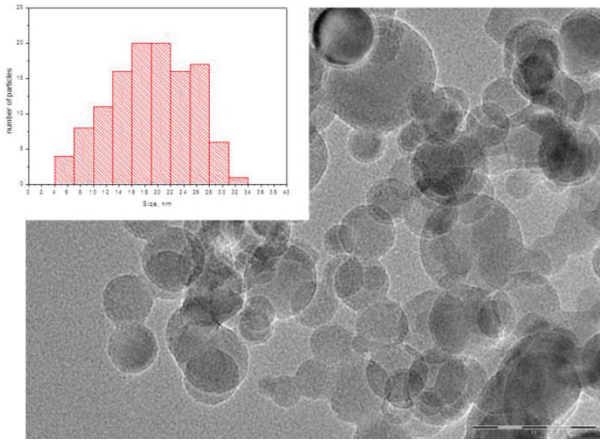

a

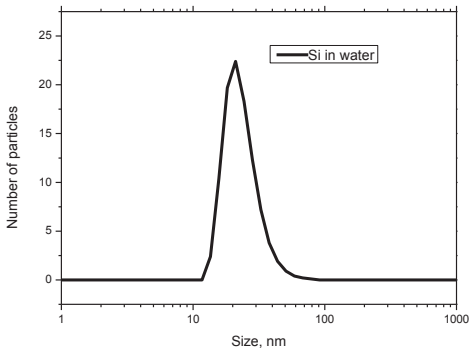

b

Figure 4.2.1:

a *The TEM image of the silicon nanoparticles obtained by the laser ablation. The size distribution obtained from the TEM image* ***b*** *Size distribution of the nanoparticles' number obtained using the DLS of water suspensions of Si NPs*

Particles size distribution obtained from the TEM images processing is shown on the **Figure 4.2.1**. Average size of such nanoparticles is about 20 nm.

The XRD analysis show that the resulted silicon nanoparticles are monocrystalline (calculated crystallite size is 15 nm) and they have the same crystal structure as a bulk silicon (**Figure 4.2.2**).

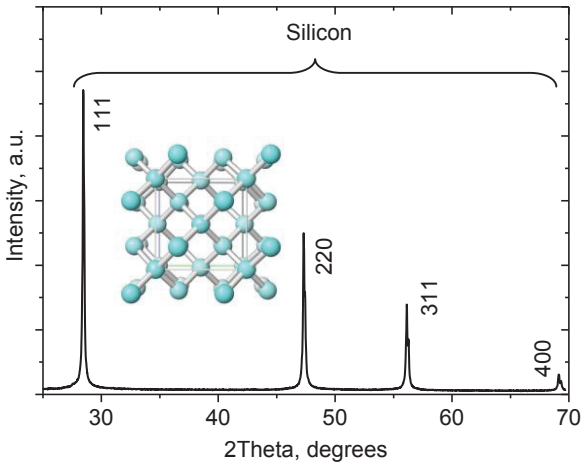

Figure 4.2.2: *the XRD pattern of the nanodiamonds powder. The XRD peak position corresponds to the bulk silicon structure (inset)*

Properties

It was found that 20 nm silicon nanoparticles, as shown in supplementary section (**Figure 8.3**), do not luminesce under UV excitation. Nevertheless, under intense irradiation they can generate second harmonic signal at doubled energy or half excitation wavelength (**Figure 4.2.3**)

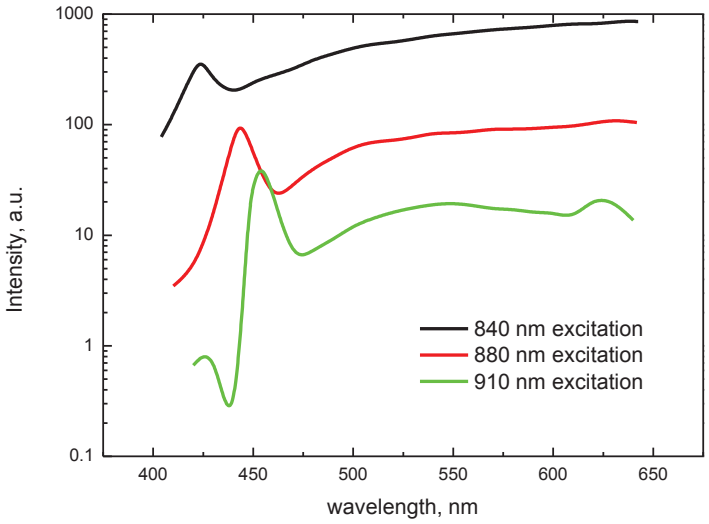

Figure 4.2.3: *Second harmonic generation ability of Si nanoparticles under IR excitation. The spectra shows that under strong IR irradiation the silicon particles with sizes about 20 nm are able to generate second harmonic response*

Also two-photon excited luminescence signal can be observed for all of the excitation wavelengths. For the applications described in this manuscript the SH signal of Si NPs is much more useful, than two-photon excited photoluminescence.

4.3 Nanodiamonds

Synthesis

Nanodiamonds with the sizes about 8 nm were ordered at Ray Techniques Ltd. The synthesis method of such nanodiamonds is Pulse Laser Ablation in Liquid (PLAL).

Structure

The nanodiamonds are the uniformly sized crystalline particles with diamond-like crystallic lattice. TEM measurements on **Figure 4.3.1** show that they exhibit in the form of the agglomerates of sub-10 nm particles.

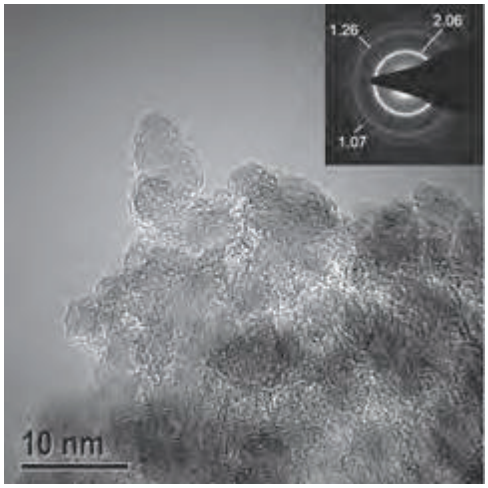

Figure 4.3.1: *TEM images of the nanodiamonds deposited from the solution. It is seen that near-10 nm nanodiamonds form the agglomerates inset shows the electron diffraction pattern.*

DLS measurements (**Figure 4.3.2**) show that in water solution they either present in form of near-40 nm aggregates or their hydrodynamic diameter is much bigger, than the size of particles itself.

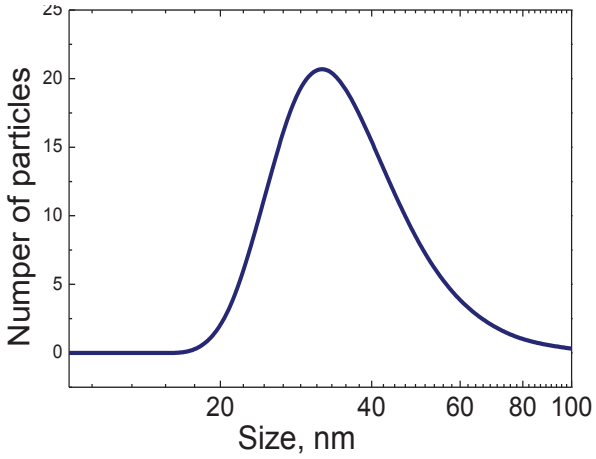

Figure 4.3.2: *Size distribution of the nanoparticles' number obtained using the DLS of water suspensions of nanodiamonds shows that the hydrodynamic diameter in solution is close to 30 nm*

XRD studies (**Figure 4.3.3**) show that nanodiamonds generally have the same crystalline structure as bulk diamonds (diffraction peaks at the same positions). The Scherrer equation allows estimating the crystallite sizes of the nanodiamonds. It is close to 8 nm

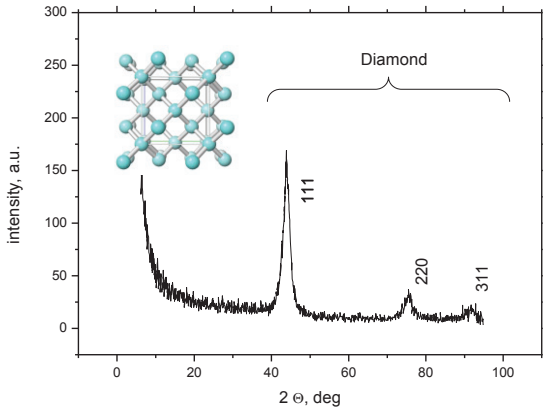

Figure 4.3.3: *XRD pattern of the nanodiamonds powder. The XRD peak position corresponds to the bulk diamond structure (inset)*

So, the nanodiamonds are the small 8 ±0.9 nm crystallites, which are slightly agglomerate in water supensions. The average agglomerate size is 30 nm.

Properties

Nanodiamonds are able to produce luminescence in green range under UV excitation. **Figure 4.3.4** shows optical properties of the diamonds. Blue curve is an absorbance spectrum of the nanodiamonds, black one is a luminescence spectrum and the red is a PLE spectrum (intensity of PL at 490 nm under different excitation). The excited state lifetime is below 10 ns.

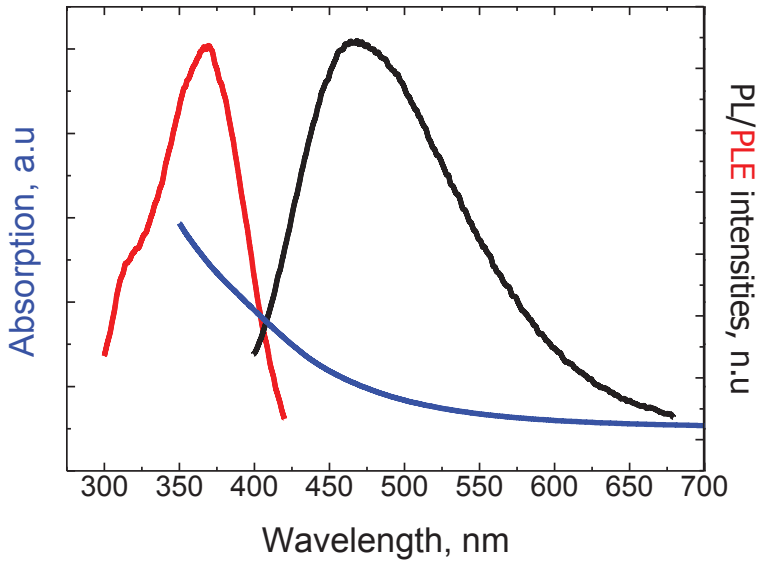

Figure 4.3.4: *the photoluminescence and absorbance spectrum of the nanodiamonds (black and blue). PLE spectrum of the nanodiamonds (emission at 490 nm)*

4.4 Carbon fluroxide (CFO)

Synthesis

Procedure of CFO production is similar to the porous silicon production, but instead of Si, polycrystalline 3-c silicon carbide wafer has been used.

Fluorescent CFO NPs were formed by means of electrochemical anodization of a low resistivity grade (<1 Ohm*.cm) bulk 3C-SiC polycrystalline wafer. The etching process took place for 3 hours at a current density of 25 mA/cm2 using a 1:1 HF (50%)/ethanol electrolyte. Despite the similar to the porous silicon production conditions, the etching of SiC is less evident process and it do not leads to the formation of the porous silicon carbide. During the anodisation, the silicon atoms are preferentially bound to the fluorine and dissolved. The rest C atoms rearrange. Such selectivity of etching is similar to the process occurs during carbon-derived carbons production process. The anodic reaction was

$$SiC + 6F^- \rightarrow SiF_6^{2-} + C(nanoparticles) + 4e$$

The prepared porous layer was dried in air for several hours. The dried layer was removed from the SiC wafer and then mechanically grinded and dispersed in a Krebs buffer solution. The formed colloidal suspension was centrifuged at 10,000×g for 20 minutes in order to collect only its top part containing very small (<10 nm) and homogeneously dispersed NPs

Structure

Since the CFO is mainly composed from low-structured and light carbon, the other methods of visualization than TEM are preferable. Such particles can be visualized on an atomic force microscopy image as shown in **Figure 4.4.1-a.** The AFM images of the CFO on the mica surface (**Figure 4.4.1a**) allow to see plenty of the NPs with a shape of thin (0.4 – 3 nm, i.e. from one to few atomic layers) disks with radius ranging from 2 to 15 nm. Size distribution of the obtained NPs was estimated from dynamic light scattering measurements

(see **Figure 4.4.1-b**) and the average NPs size is found to be in the range: 4-6 nm.

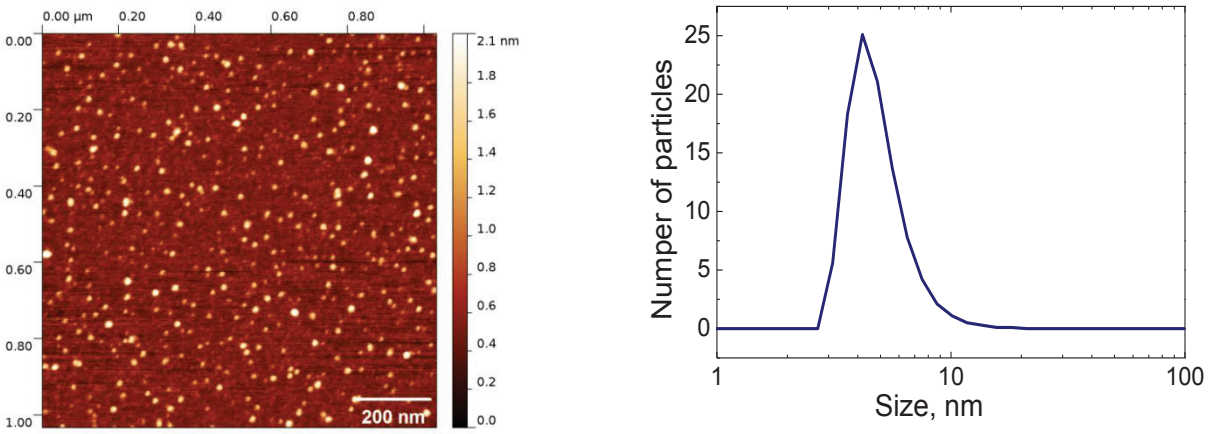

(a) **(b)**

Figure 4.4.1: *size characterizations of the CFO nanoparticles.*

a - AFM Image of the CFO NPs deposited on mica

b – Size distribution of the nanoparticles' number obtained using DLS technique

Fourier transform infrared spectrum shown in **Figure 4.4.2** gives an idea about dominant chemical bonds. (C-H, C=O and C-O) taking place in the fabricated NPs. Thus, the NPs surface is supposed to be mainly covered by carboxylic and ester groups. In order to check such propose, the NPs were hydrolised with NaOH at pH 13 in order to observe the surface bonds change. As predicted, the C-F and C-OOEt bonds were mainly replaced with C-OH, C-OOH and COONa bonds correspondingly.

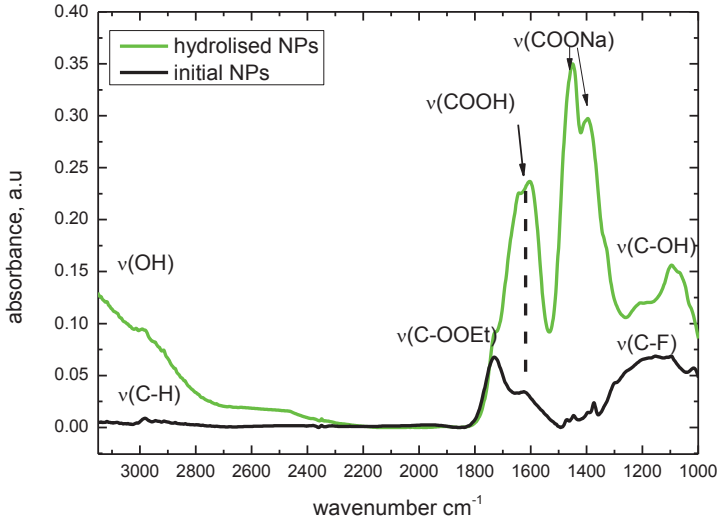

Figure 4.4.2: *the infrared absorbance spectrum of the CFO nanoparticles. Arrows show the vibrations of the specific groups.*

CFO nanoparticles were found to be XRD-amorphous (see supplementary **Figure 8.4**), which means they have not got strict crystalline structure. The structural composition of the CFO nanoparticles was estimated in [113] The preposition of the NPs structure is shown on **Figure 4.4.3**

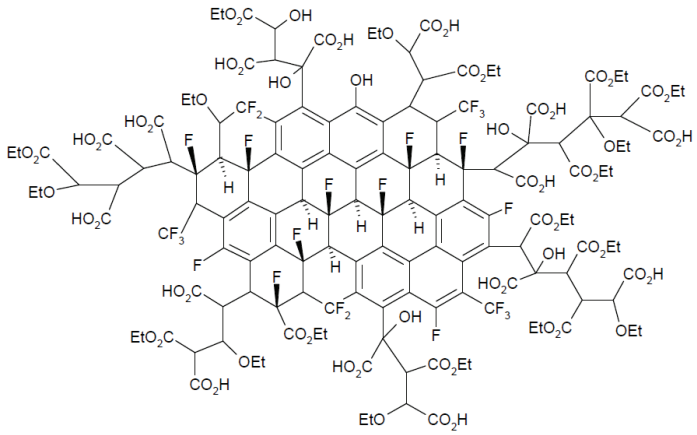

Figure 4.4.3: *the structure of the CFO NPs [112]*

The CFO nanoparticles can be described as non-crystalline semi-inorganic structures with the large amount of carboxyl groups at the surface and small average size (8 nm). They do not form agglomerates in water suspensions.

Properties

Absorbance and one-photon excited luminescence spectra of the CFO NPs are shown in figure 3. As one can see, the CFO NPs have a strong absorbance in the UV spectral range, and their photoluminescence, excited at 400 nm, is centered near 550 nm. The shape of the spectra is excitation-dependent, so we can propose the presence of different emission centers, which are excited preferentially by the different wavelengths.

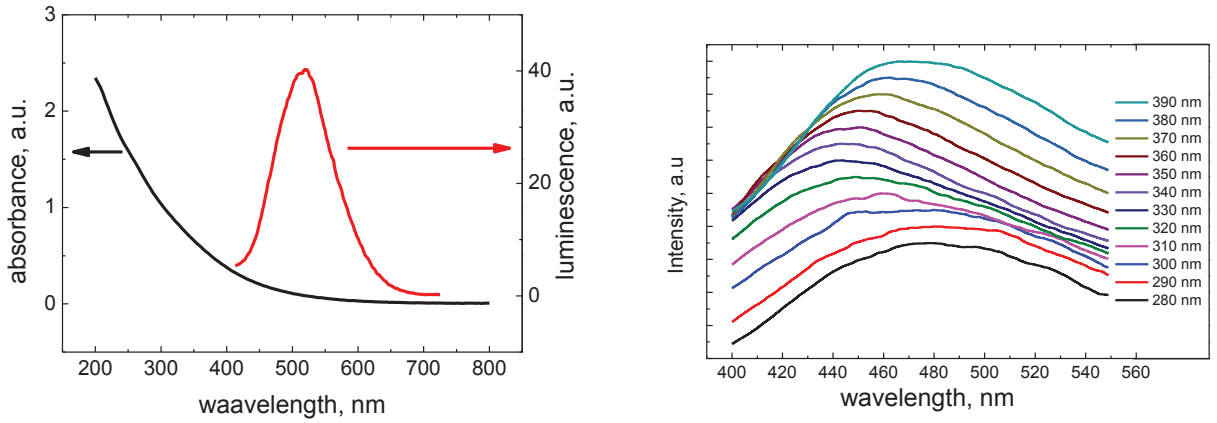

(a) **(b)**

Figure 4.4.4: *the photoluminescent properties of the CFO nanoparticles*

a – absorbance and emission spectra of the CFO nanoparticles water solution. Excitation wavelength – 360 nm

b – The excitation dependence of the PL spectrum of CFO nanoparticles

4.5 Silicon carbide

Synthesis

Silicon carbide nanoparticles were provided by the KM labs (Kiev) [114], and were obtained by carbothermal reduction from the amorphous silica, sucrose and citric acid (only for water quantity reduction). All the precursors were mixed in deionized water for 1 hour and dried to white pellets, that have been carbonized at 240^{o} C. The dark brown powder has been obtained. Finally, SiC nanopowder was obtained using high temperature treatment in furnace at 1420 C in mid vacuum under Ar flow. The reactions, followed by the treatment are the next:

1st step

$$C_6H_8O_7 \rightarrow 3C + 4H_2O + 3CO$$

$$C_{12}H_{22}O_{11} \rightarrow 12C + 11H_2O$$

2nd step

$$SiO_2(amorphous) + 3C \rightarrow 2CO + SiC(nps)$$

Structure

The sizes of the SiC particles were evaluated by the 3 different methods. SEM shows the relatively big particles with sizes about 300 nm. (**Figure 4.5.1**)

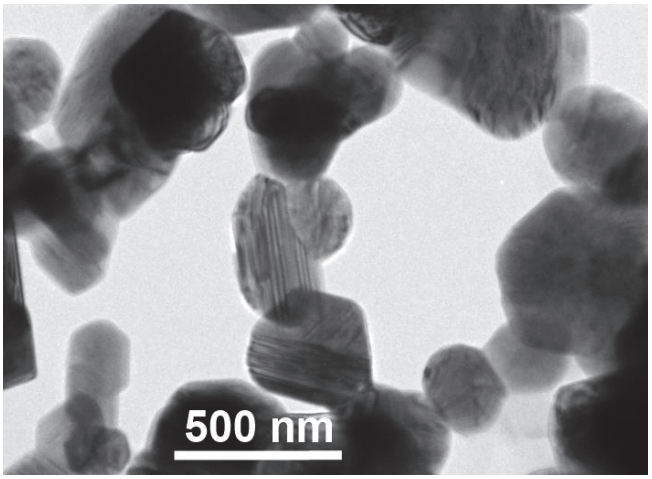

Figure 4.5.1: *the TEM image of the silicon carbide particles*

DLS measurements in water were in accordance with the TEM and shows the similar size (**Figure 4.5.2**)

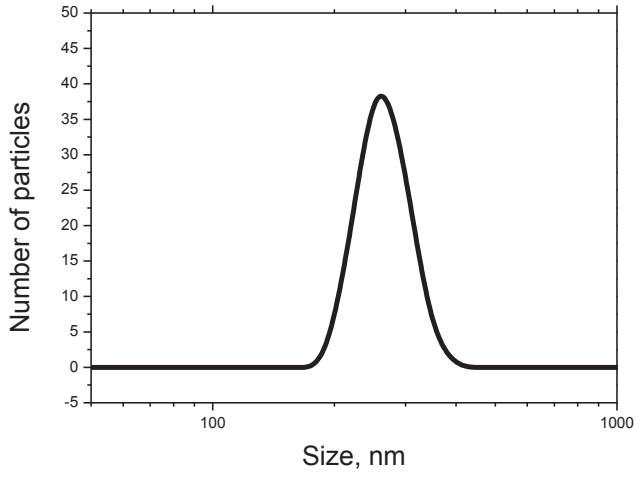

Figure 4.5.2: *the size distribution of the SiC particles obtained using DLS method*

Nevertheless, the other XRD shows that the average crystallite size is close to 70 nm (**Figure 4.5.3**). Also it was found the trace amount of hexahonal silicon carbide.

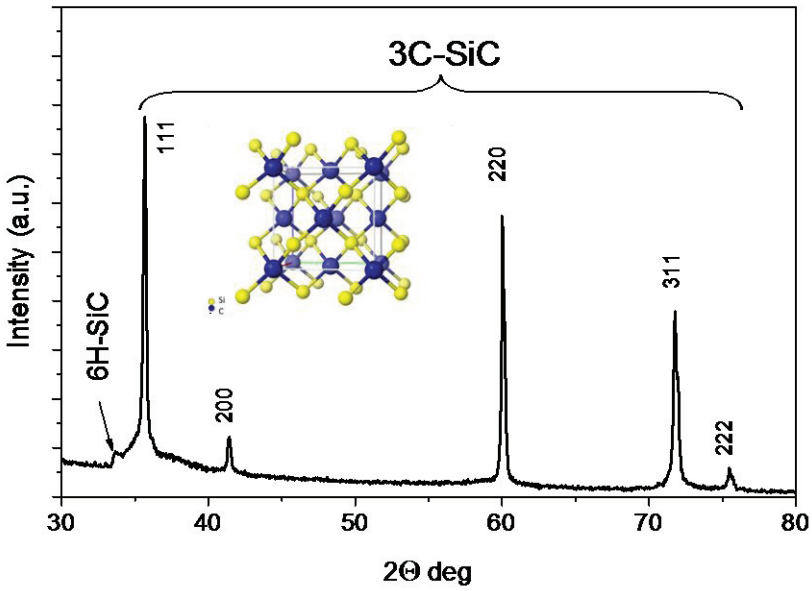

Figure 4.5.3: *the XRD pattern of the nanodiamonds powder. The XRD peak position corresponds to the bulk 3c-SiC structure (inset)*

The SiC particles have relatively big average size (250 nm) and have the structure of bulk 3c-SiC. Crystallite size, calculated from XRD pattern is about 70 ± 6 nm. That means SiC nanoparticles are not single-domained and they are consist of the several crystalline domains. The such domains do not deagglomerate in water.

Properties

The SiC nanoparticles are luminescent in a green range under UV excitation. Absorbance and emission spectra are shown on the **Figure 4.5.4.** The band gap of the bulk 3c-SiC is 2.3 eV, which corresponds to the luminescence maximum at 540 nm. One can see, that the measured luminescence maximum lies at 800 nm. That can be attributed to the recombination of confined photogenerated charge carriers at the surface defects of the particles.

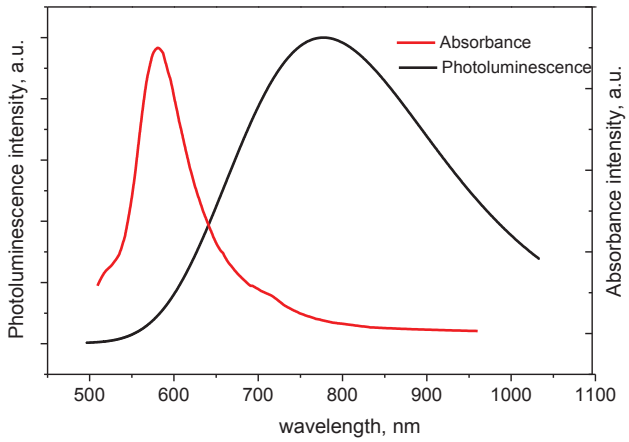

Figure 4.5.4: *Absorbance and emission spectra of the SiC particles in water suspensions. Excitation wavelength for PL graph – 360 nm.*

4.6 Conclusion of chapter 4

It was found that the group IV nanoparticles used in this work have various physical parameters. The particles' size is ranged from 8 up to 300 nm. The photoluminescent properties are also varying. Some types of the particles are non-luminescent, other have luminescence in different ranges. The comparison of the nanoparticles is shown in **Table 4.6.1**

NPs type	Size of crystallites	Size of agglomerates	PL properties	Crystalline structure
Porous Si	~3 nm	~150nm	Broad peak at 800 nm	Centrosymmetric diamond-like structure
NanoSi	~ 20 nm	~20 nm	Not luminescent	Centrosymmetric diamond-like structure
Nanodiamonds	~6 nm	~30 nm	Sharp peak at 475 nm	Centrosymmetric diamond-like structure
CFO		8 nm	Broad peak at 550 nm	Not crystalline
SiC	40 nm	~300 nm	Broad peak at 800 nm	Non- centrosymmetric sphalerite-like structure

Table 4.6.1: *the comparison of the physical properties of the NPs*

The different values in 2nd and 3rd columns for porous silicon, silicon carbide and nanodiamonds allows to propose that for these kinds of particles we have got the agglomerates in water solutions.

We obtained 2 types of silicon particles, with 3 nm crystallites and 20 nm ones. The 3 nm NPs are agglomerated and form porous silicon structure. They are brightly luminescent under UV excitation. The 20 nm particles are not luminescent.

The carbon particles are presented as fluorescent nanodiamonds with average size about 6 nm and also fluorescent CFO particles, which have complicated macromolecular structure.

Finally, SiC nanoparticles are presented as a relatevily big (300 nm) agglomerates of the fluorescent 40 nm nanocrystals.

The silicon and diamond particles have the same diamond-like cubic crystalline structure. Silicon carbide particles have non-centrosymetrical cubic sphalerite-like lattice.

Since the sphalerite structure, in comparison with the diamond one is not centrosymetrical, the 3c-SiC nanoparticles can be promising for second harmonic microscopy imaging. All of the luminescent particles can be used for imaging experiments.

5 Interaction of the NPs with the cells

It is possible to detect the particles inside the cells using different modalities. Some particles can be detected with one photon excited PL microscopy, other are seen using SH or TPEF microscopy. All the abovementioned nanoparticles have been tested on 3T3-L1 mouse fibroblasts in order to detect their intra-cellular localization (section 5.1) and to measure their cytotoxicity (section 5.2). At section 5.3 it is shown that some kind of particles are bound to proteins of the culture medium. A method to avoid such binding was proposed.

5.1 Nanoparticles' uptake

All of the particles have been tested on the 3T3-L1 cell line. Using the microscopy techniques it is possible to localize the particles inside cells. For CFO nanoparticles, porous silicon and nanodiamonds ordinary fluorescent microscopy can be used. Since SiC and bigger particles do not luminesce under UV excitation, but they are able to produce SH signal or 2-photon excited PL. Non-linear microscopy has been used for examination of these NPs distribution.

Porous silicon

Since porous silicon particles have sizes about 200 nm, weak cellular uptake was expected. Nevertheless, photoluminescent microscopy (the excitation/emission conditions were at the **Section 3.2.1**) of the 3T3-L1 cells after 4 hours of incubation with 0.25 g/L of porous silicon nanoparticles shows a strong labelling suggesting that a significant quantity of these NPs have been uptaken by cells (**Figure 5.1.1**).

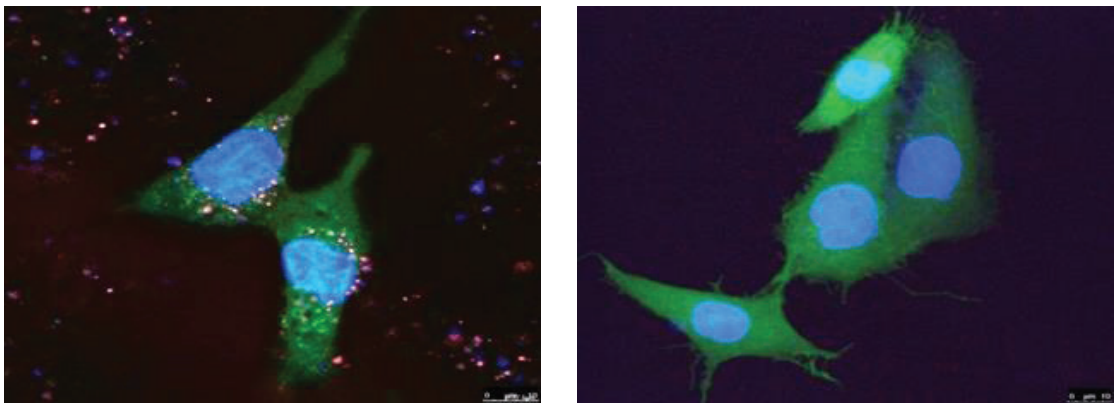

a **b**

Figure 5.1.1*: (a) Fluorescent image of 3T3-L1 cells labeled with 0.25 mg/mL of porous silicon particles. (b) Control sample without porous silicon exposure. Green, blue, and red colors correspond to the PL of cell membrane, cell nucleus, and SiNPs,*

respectively. Cell nuclei were imbued with 5 mg Hoechst dye.

Porous silicon does not produce any second harmonic signal, but it can be used for 2 photon excited imaging (**Figure 5.1.2**).

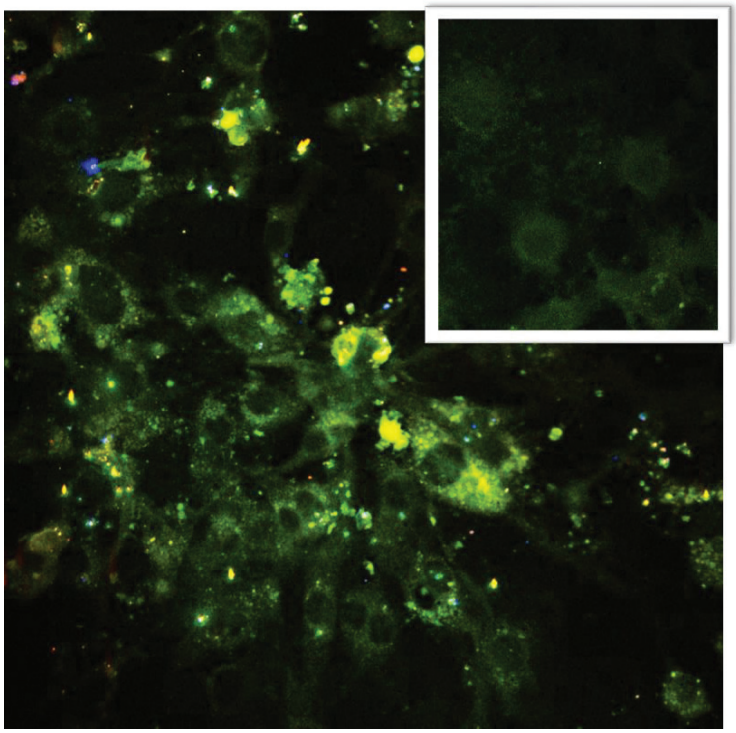

***Figure 5.1.2**: 3T3-L1 cells labeling with porous silicon Yellow dots inside the cell cytoplasm correspond to the porous silicon particles. Control sample without porous silicon is in the inset. The multichannel image with IR laser excitation (800 nm). Green channel corresponds to 500-600 nm fluorescence, blue channel is a second harmonic signal (400 nm) control sample is at the insert.*

Two-photon excited PL microscopy image shows the same localization of the nanoparticles as single photon one – the particles are inside the cytoplasms. All porous silicon particles can be seen as separated luminescent dots. That means, the porous silicon nanoparticles are present into the cytoplasm of cells in form of the relatively big agglomerates.

Nanosilicon

Typical bi-modal images of the 3T3-L1 fibroblasts cells labeled with Si nanoparticles (20nm) are shown in **Figure 5.1.3**. General healthy look of the cells, corroborating the non-toxic impact of the chosen nanoparticles' concentration (0.25 mg/mL, toxicity measurements at **section 5.2**), can be remarked. On the presented pictures, blue color corresponds to the second harmonic (SH) signal while green, yellow and red colors – to the two-photon excited

photoluminescence (TPEL) one. As it can be seen from the cell image shown in **Figure 5.1.3-a** where the signals from all detection channels are mixed together, cytoplasms of the labeled cells clearly appear mainly in yellow color accompanied by slight red tones. Since auto-fluorescence intensity of the non-labeled cells is too weak under these excitation/detection conditions (see inset in **Figure 5.1.3-a**), the observed TPEL of the labeled cells can be attributed to the smallest Si nanoparticles (with crystalline core diameters <10 nm) accumulated inside the cellular cytoplasm and ensuring its quite bright staining. The recorded high TPEL emitted by the Si NCs can be explained by their enhanced non-linear absorption due to quantum confinement and dielectric mismatch phenomena. Indeed, the non-linear absorption coefficient of Si NPs defining their third-order non-linearity and depending on the NPs size can be two orders of magnitude higher than the bulk Si value.

A special attention must be paid to numerous bright white spots with violet contours decorating the cell images. They are especially well seen in **Figure 5.1.3-b** showing a single cell from the previous picture. In particular, their localization outside the cell membranes is demonstrated by 3D image shown in **Figure 5.1.3-c**. White color of the spots means that they provide both SH and multicolor TPEL signals. For example, the picture given only by the SH channel is presented in **Figure 5.1.3-d**. The clear granular shape of the spots generating the most intensive SH emission indicates that they correspond to an aggregation of the NCs. Indeed, the Si NCs are known to be able to easily aggregate in a water containing solutions via van der Waals forces appearing between their silica shells. Being too big, the aggregated species cannot penetrate inside the cells. Nevertheless, they ensure very efficient bi-modal cell labeling. Smaller separate blue spots can be also visible in **Figures 5.1.3-b** and **5.1.3-d**. They are provided by SH signals generated by individual and relatively large Si NCs with diameters ≥20 nm.

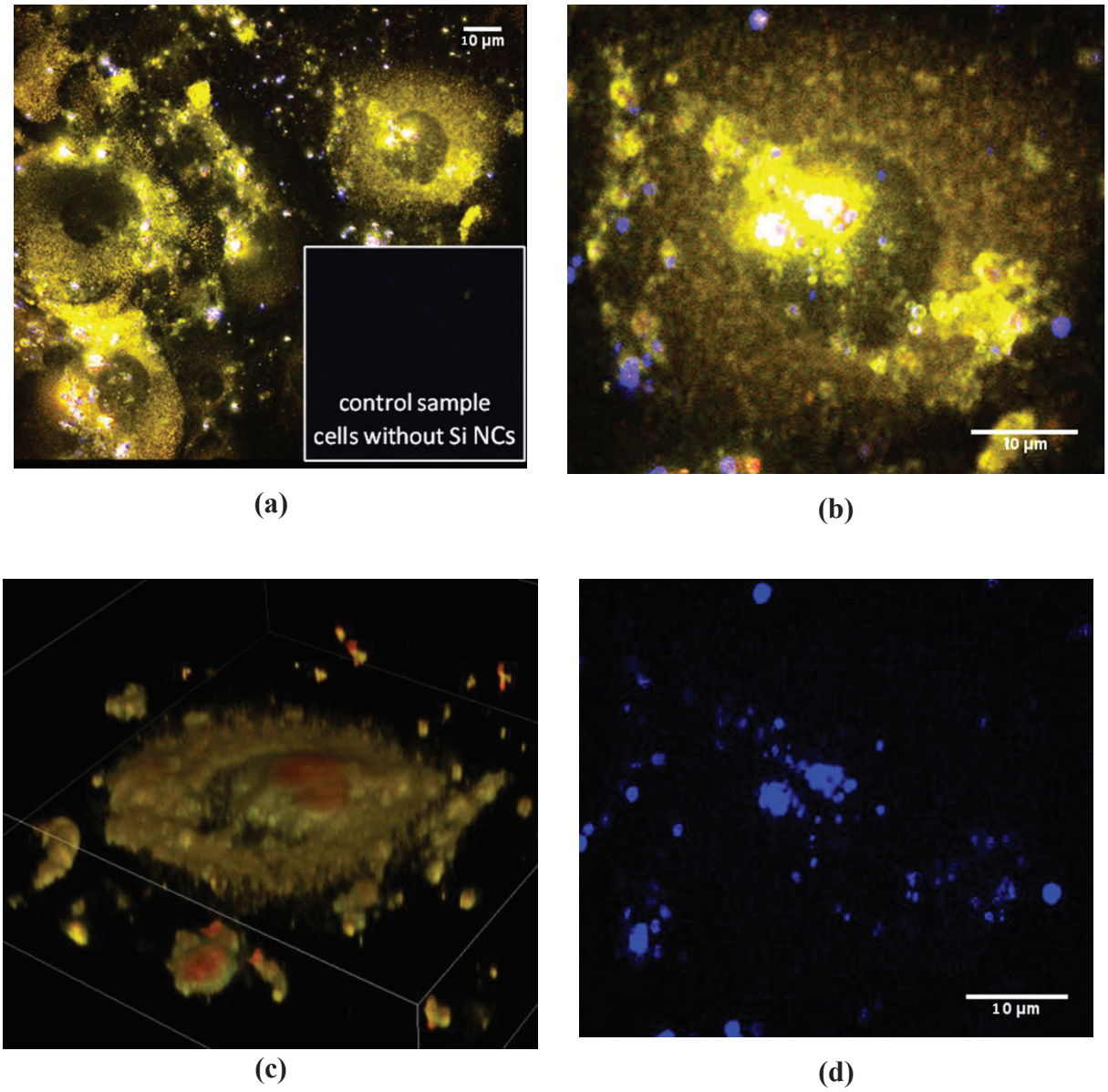

Figure 5.1.3: *(a) Non-linear optical image of the 3T3-L1 cells labeled with Si NCs (inset shows image of non-labeled control cells); (b) non-linear optical image of a single cell from the previous picture; (c) 3D image of the single cell from previous 2D picture; (d) second harmonic image of the single cell from the picture (b).*

Nanodiamonds

Nanodiamonds are oftenly proposed as an agent for the PL labeling for cell visualization. In our case, extremely small nanodiamonds (8 nm) were used for the labeling (**Figure 5.1.4** and **5.1.5**)

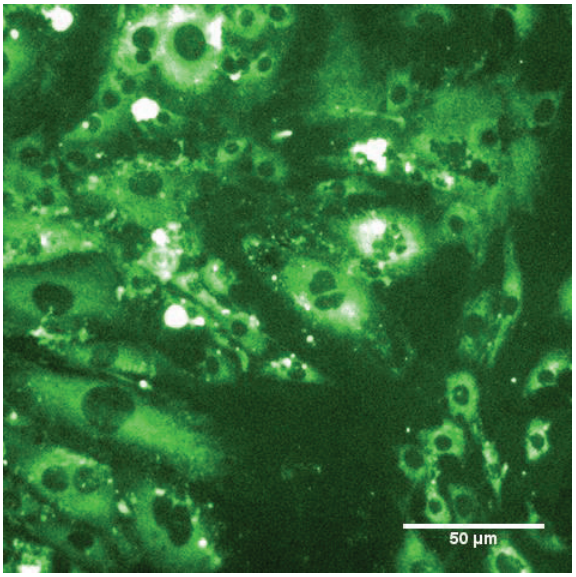

***Figure 5.1.4**: PL microscopy image of the 3T3-L1 cells labeled with 0.25 mg/mL of nanodiamonds for 24h.*

The **Figure 5.1.4** shows the uniform distribution of the nanodiamonds inside the cytoplasms of cells. Moreover, it can be also seen, that there is almost no luminescence inside the nuclei of the cells.

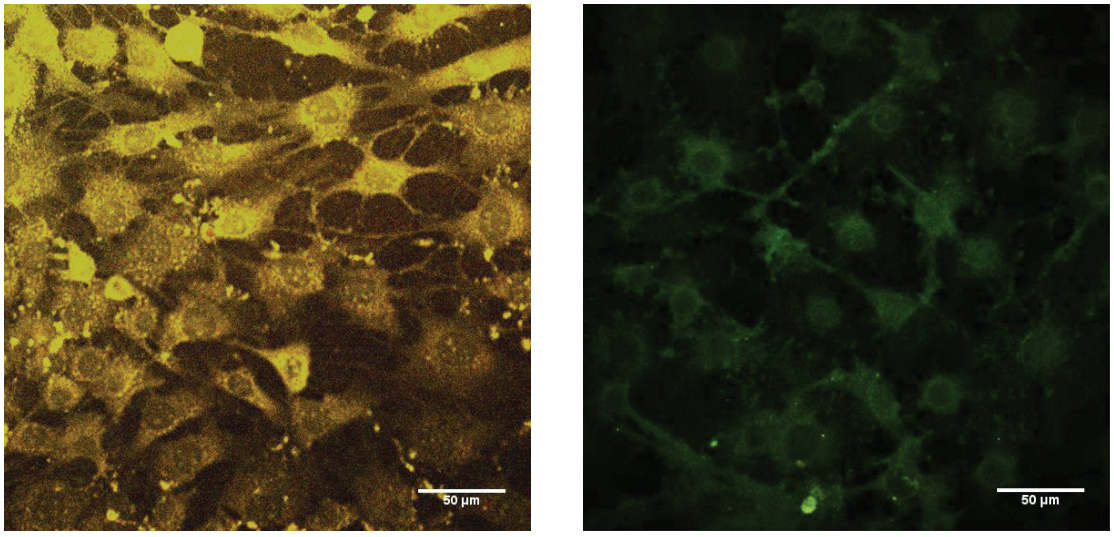

a **b**

***Figure 5.1.5**: 2-photon excited PL microscopy image of the (a) 3T3-L1 cells labeled with 0.25 mg/mL of nanodiamonds for 24h (b) control sample of 3T3-L1 under the same excitation end detection conditions.*

The **Figure 5.1.5** shows that due to high 2 photon absorption, the nanodiamonds also can be used for non-linear microscopy labeling. The 800 nm excitation leads to the generation of the TPEL signal from the nanodiamonds. Nanodiamonds localization inside the cells is in coincidence with the one observed using 1 photon excited PL microscopy.

CFO

As-prepared CFO nanoparticles can be used for the cell fluorescent labeling. It was found, that such particles predominantly accumulate inside the cell nuclei (**Figure 5.1.6**)

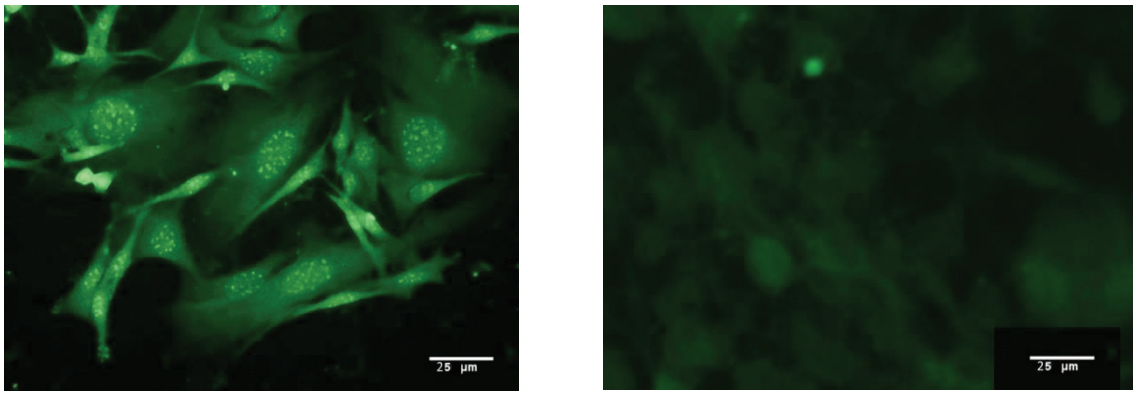

a **b**

Figure 5.1.6*: single channel photoluminescent images of the (a) 3T3-L1 cells labeled with 0.25 mg/mL of CFO nanoparticles for 24h. (b) non labelled 3t3-l1 cells under the same conditions. CFO NPs are predominantly accumulated inside the cells nuclei*

The **Figure 5.1.6** clearly highlights selective incorporation of the fluorescent SiC NPs inside the cell. Under UV/violet excitation, the cells marked by the NPs are very bright while the autofluorescence of unmarked cells is not observed at all. In particular, the cells labeled with the CFO NPs appear to be extremely bright, with the most intense fluorescence signal coming from the nuclei. It can be seen, that small particles (below 10 nm) uniformly label the cell and, as a result, it is possible to see a lot of details inside the cell. **Figure 5.1.6** shows the increased good contrast inside the nuclei.

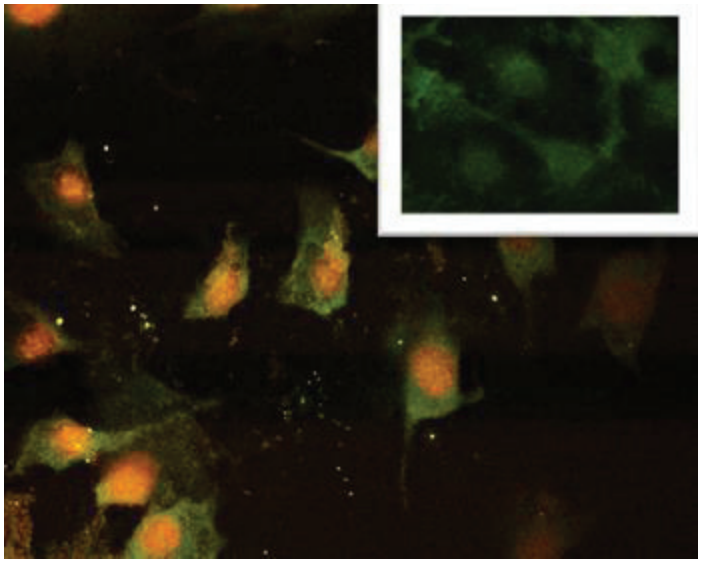

Figure 5.1.7*: non-linear optical image of the 3T3-L1 cells labeled with CFO nanoparticles (inset shows image of non-labeled control).*

Red channel corresponds to the higher wavelength, than the green one. So the orange nuclei mean an increased concentration of the nanoparticles and self-absorbance effect. As a result of absorbance of short wavelength and re-emission of longer ones, the final photon energy is lower, than in less concentrated regions, which confirms the fact of predominant nuclei uptake. Since the high z-resolution of the TPEL microscope we can conclude that the CFO NPs are accumulated inside the nuclei.

Silicon carbide nanoparticles

SiC nanoparticles had never been used as labels for the second harmonic imaging before. **Figure 5.1.8** demonstrates the possibility of using SiC nanoparticles for cell labeling. In this case laser excitation was set at 790 nm. The blue color corresponds to the second harmonic emission (395 nm) and three other colors (green for 485 nm channel, yellow for 525 channel and red for 607 nm channel) correspond to the 2photon excited fluorescence of the SiC nanoparticles and the cells. The morphology of the cell can be seen by the autofluorescence represented in green.

It can be noticed, that second harmonic signal (blue color) does not always colocalize perfectly with the 2photon excited PL at the **Figure 5.1.8**. The fact that some particles can be detected by the TPEF signal only can be explained by the size dependence of the second harmonic emission. Since TPEF signal is proportional to the 3^{rd} grade of the radius of NPs and SH signal is proportional to the 6^{th} grade, the smaller particles might yield the stronger TPEF than second harmonic signal. It can be seen that the bigger particles (yelding SH signal) are

mainly present on the cell membrane, while the smaller ones (yellow channel) are able to penetrate inside the cell cytoplasm.

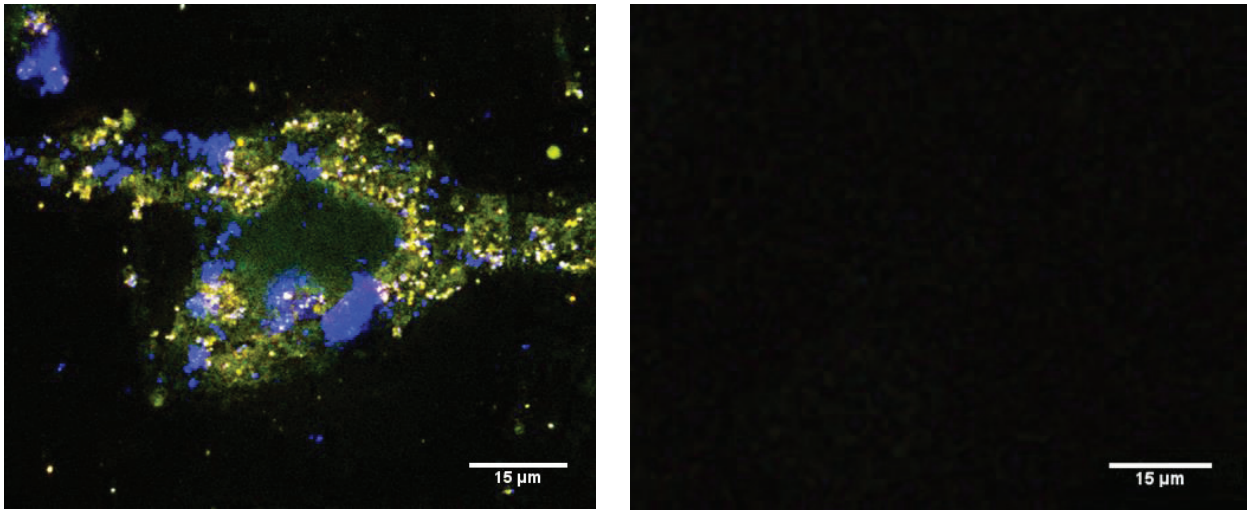

(a) **(b)**

Figure 5.1.8*: a non-linear optical image of the 3T3-L1 cell labeled with 0.1 mg/mL of SiC particles for 4 h. Blue channel is a second harmonic channel and corresponds to relatively big SiC particles, the yellow dots show the TPEL signal from small SiC particles b control sample of the 3T3-L1 cell under the same excitation and emission conditions*

5.2 Toxicity of nanoparticles.

CFO NPs

Since the CFO nanoparticles are able to enter the cell nuclei and seem to be most promising for the cell imaging, their toxicity has been studied in great details using xCELLigence system which allows to measure the real-time cell number in response to increasing concentrations of nanoparticles. Such measurements are expressed as a cell index (which is proportional to the cell number) on time plots. The results presented here concern the effect of CFO on HepG2 cancer cells.

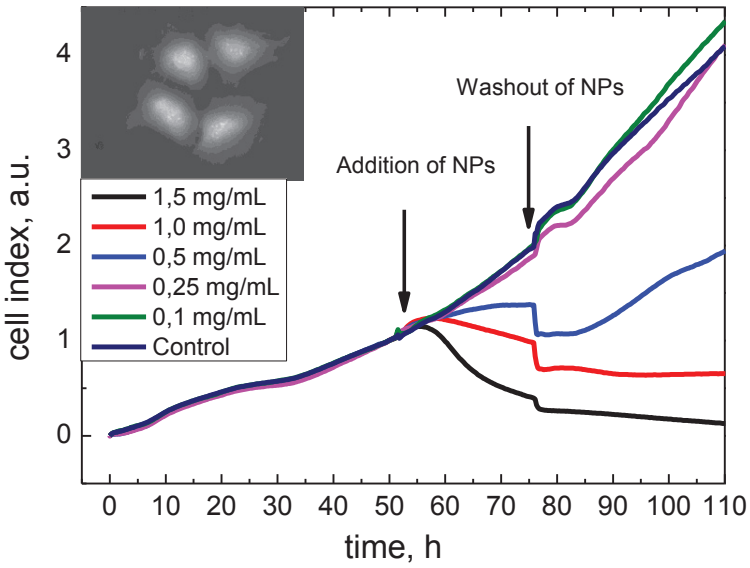

Figure 5.2.1*: cell index evolution curves for the HepG2 cells in presence of increasing CFO NPs concentrations. Arrows show the time of the CFO NPs addition and washout out time, corresponding to the change of the culture medium. The effect of uptaken NPs on cell proliferation can then be measured. Inset shows the photoluminescent microscopy image of the CFO NPs inside the HepG2 cells. Each curve is the average of the 8 simultaneous measurements*

HepG2 cells were allowed to grow without any treatment during 48 hours. At that time, increasing concentrations of CFO NPs were added to the wells for 24 hours (n=8). The highest dose of NPs is the most toxic and causes fast decrease of the cell index. The effects of CFO NPs are fast and can be seen rapidly on the cell index curves. **Figure 5.2.1** shows a dose-response effect after addition of the nanoparticles. After washing out the NPs, the cells can either restart proliferating (concentration 0 - 0.5 mg/mL) or not (1 and 1.5 mg/mL).

Although we have tested a wide range of NPs concentrations, it was not possible to measure all the concentrations. Nevertheless it can be interpolated that the effects of intermediate NPs concentrations would be intermediate to the results measured. For example, although we did not measure the effect of CFO NPs at 0.75 mg/mL we may reasonably expect that the cell index curve would have been between the ones observed in response to 0.5 and 1 mg/mL of CFO NPs (**Figure 5.2.2**).

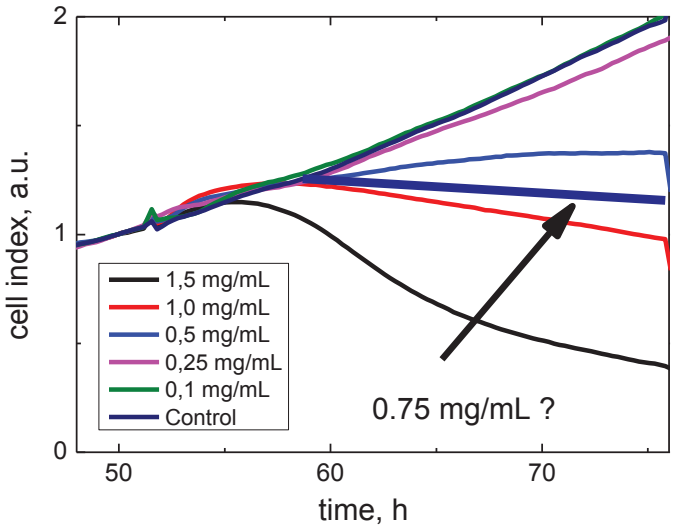

Figure 5.2.2*: example of approximation for plotting the 0.75 mg/mL cell index line.*

Using the linear interpolation of the measured data, cell index curves for all of the intermediate concentrations can be obtained. We can use the measured curves as a basis for intermediate concentrations cell index plot. For the representation of such proposal, 3D surface in the time-concentration-cell number coordinates was plotted (OriginPro software, gridding using Renka and Cline method [115]). It is possible to perform such experiment using xCelligence and such plot gives all available information about toxicity. An example of such plot is given in **Figure 5.2.3a**, which shows dose-time-cell index curve of HepG2 cells incubated with different amount of CFO nanoparticles (50 hours is the time of NPs addition). Using the cross sections of such plot (**Figure 5.2.3 b**) the evolution curves of the cell index (**Figure 5.2.3 b** upper graph), the dose response curves on the selected time **(Figure 5.2.3 b)** left graph were obtained. The section with horizontal plane give for example IC80 values for different time frames. In **Figure 5.2.3 b** (central plot), yellow line shows the horizontal plane cross-section at level 0.2. In other words, that line shows IC80 value for different exposure times.

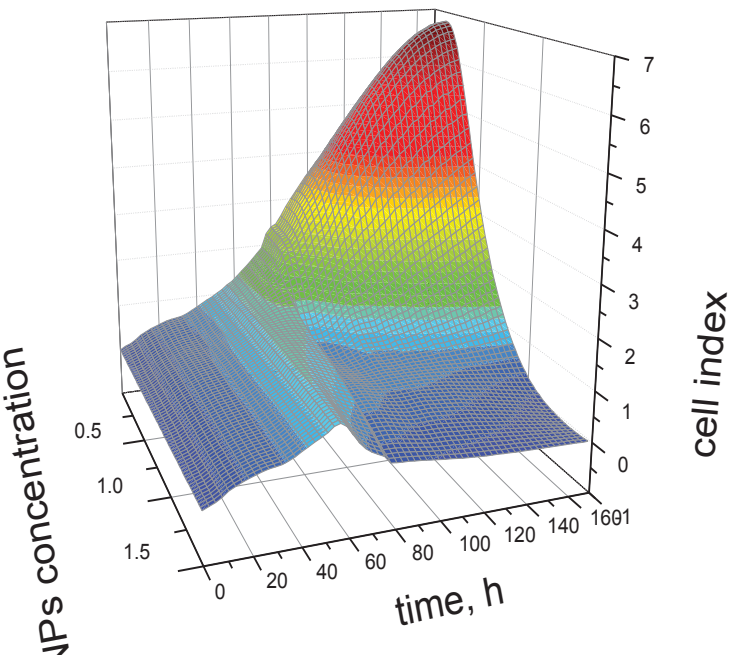

a

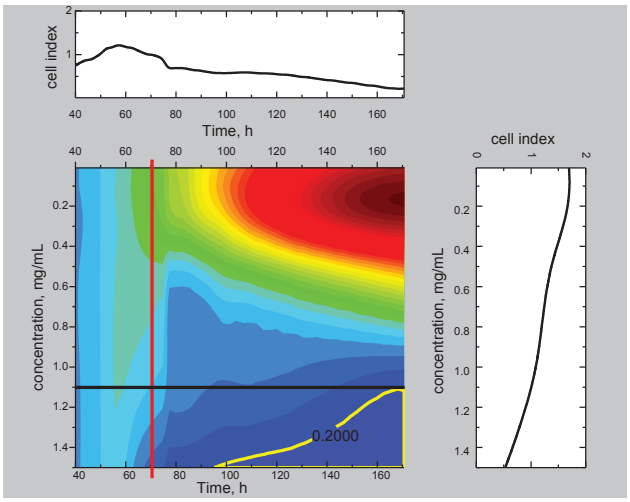

b

Figure 5.2.3: *a – 3D plot of the cell index – concentration – time dependence. (plotted using OriginLab 8.1)*

b – Colored map of the same representation, red line shows the example of cross-section plane at 70 h, left Figure is cell index profile at this time, black line at central plot – cross section plane at constant concentration (1.1mg/mL), cell index evolution curve corresponded to that concentration is the upper graph. Yellow line is a constant cell index plane cross-section line at height 0.2 (corresponds to IC80).

Other interesting idea on data representation is to show not the cell index itself, in some cases the showing of the cell growth or cell death speed can be more interesting. Cell growth parameter can be calculated as a relative slope (slope of cell index evolution curves, normalized

on cell index at the same moment). **Figure 5.2.4** shows such a plot for HepG2 cells. Looking at Figure 5.2.4 we can notice the normal growth (red color). After addition of NPs cell proliferation slows down (color changes to green or darker ones). Depending on NPs concentrations in the medium one can see the different effects, from slowing down (orange) cell index growth (green) and the cell index decrease (blue-violet). It can be clearly seen on such kind of plot that cells start responding the NPs not instantly, it takes about 5 h from cell addition (first black line) to observe an effect (red dash line). After washing out, high concentration (1 mg/mL) change the cells proliferation speed. So, the particles left inside the cells after washout can change the proliferating ability of the cells.

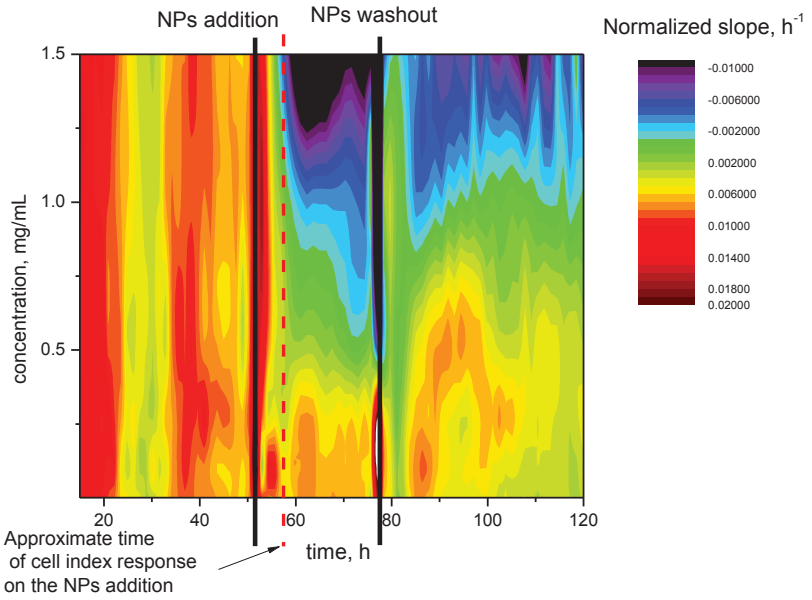

***Figure 5.2.4**: colored map of the HepG2 cell index growth speed under exposure with CFO NPs. (plotted using OriginLab 8.1)*

The main advantage of such a representation is that it rapidly indicates the effects of NPs on cell index. Limitations are that it is may be not so easy to understand and it does not contain any statistical error bars. So the next plots are given as a curves, corresponding to different NPs concentrations at the same plot.

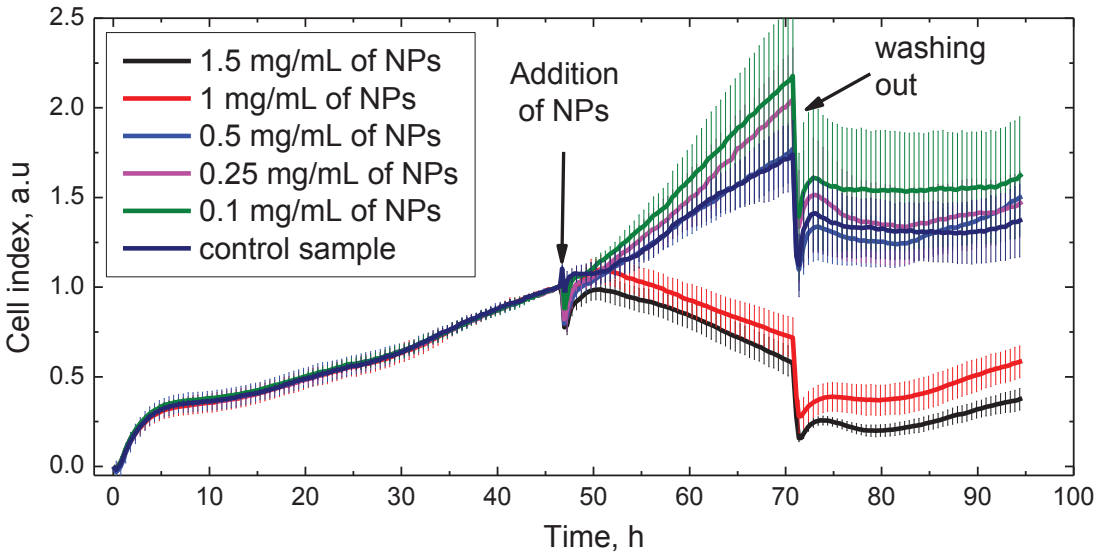

Figure 5.2.5: *cell index curves evolution of 3T3-L1 cells in response to increasing concentrations of CFO NPs and after washing out. Arrows show the time of the carbon fluorooxide addition and changing of the medium (wash out).*

The CFO nanoparticles are found to be toxic at 1 mg/mL. The slope of the cell index curve significantly changes after washing out. That fact means that the NPs left inside the cells affect their proliferation rate.

Kinetics of the CFO nanoparticles cellular uptake.

In order to get the average time necessary for the 3T3-L1 cells to uptake NPs, the average luminescence of the cells was measured under real time conditions. The graph with the PL intensity on time is shown on the **Figure 5.2.6.** Since measurements were done in medium, which produces photoluminescent background signal at the same wavelength as a CFO NPs, the measurements were performed using red filter (excitation 580-600 nm, emission 620-680 nm).

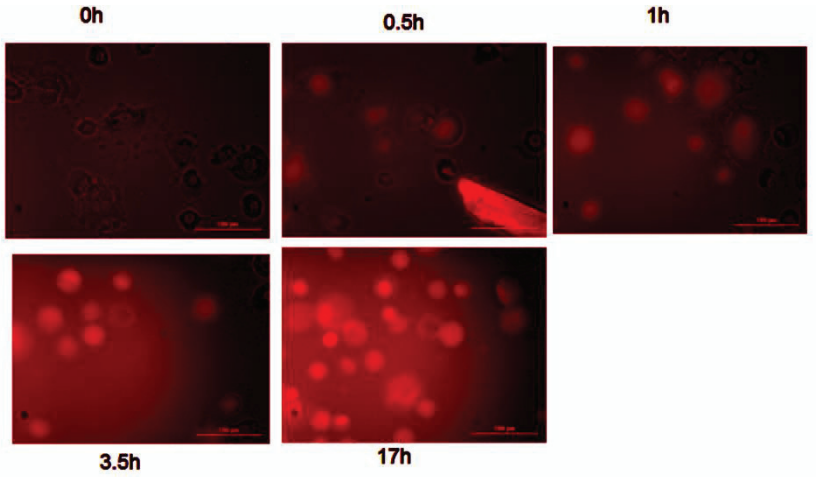

a

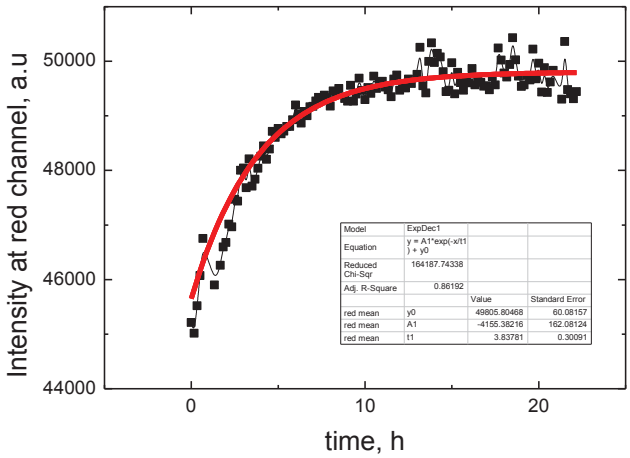

b

Figure 5.2.6: *time dependence of the penetration of the CFO NPs into the cells.*

a – the typical images used for processing and fluorescence intensity calculations. During time, there is an increasing amount of NPs inside the cells.

b – the evolution of the luminescence intensity of the cells during exposure with 0.25 mg/mL of CFO nanoparticles.

High initial baseline is caused by the NPs into the PBS solution. Since the microscope is focused on the plane with the cells, the local increase of NPs concentration inside the cells will cause increase of the PL intensity. According to this model:

$$I = I_{sat} - I_0 e^{-\frac{t}{t_{uptake}}};$$

where I_{sat} PL intensity in case of saturation with NPs, t_{uptake} is a characteristic uptake time. That time shows the time needed for the cells to reach the saturation inside the nanoparticles solution. The results of such measurements show that the average time necessary for the significant uptake is close to 5 h. So the both data from the cell index analysis and luminescent particles uptake kinetics shows that the characteristic time of the nanoparticles uptake is 5h.

Other nanoparticles toxicity.

The dose response cell index curves of the 3T3-L1 cells under exposure with the porous silicon, 20 nm silicon, nanodiamonds and SiC particles is shown on Figure 5.2.4 The nanoparticles were added (first arrow) after cell proliferation period, 24 hours later the medium was changed (second arrow).

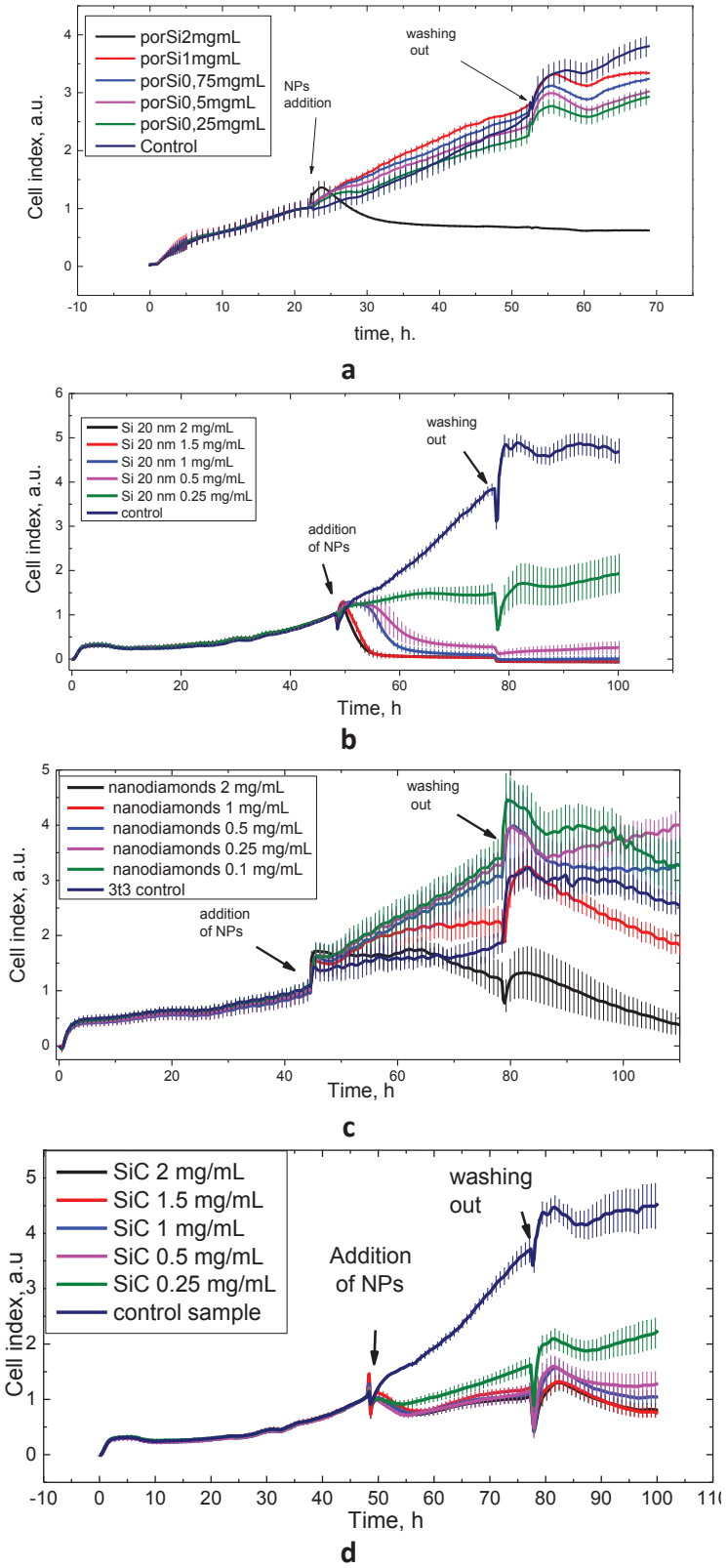

Figure 5.2.7*: Cell index evolution curves for the 3T3-L1 cells. Arrows show the time of the NPs addition and changing of the medium*

a – porous silicon, b- 20 nm silicon particles, c – nanodiamonds, d – SiC particles.

The only concentration of porous silicon that significantly affects the cell proliferation behavior is 2 mg/mL (**Figure 5.2.7a**): The lower concentrations do not change the cells proliferation rate.

It was found, that the toxic concentration of Silicon NPs (20nm) is about 0.5 mg/mL, the smaller concentrations are also able to stop the cell proliferation (**Figure 5.2.7b**). The porous silicon was found to be less toxic than the 20 nm particles. Such effect can be explained by the lower penetration ability of the above-100 nm porous silicon agglomerates inside the cells compared to 20 nm ones.

Cell index evolution curves for nanodiamonds are shown at **Figure 5.2.7c**. The toxic dose for nanodiamonds is 2 mg/mL.

Silicon carbide nanoparticles are shown to have an effect on 3T3-L1 cells proliferation at the concentrations higher than 0.25mg/mL (**Figure 5.2.7d**), The proliferation does not restart after washing the particles out, so the SiC at concentrations above 0.25 mg/ml cause the cell death.

5.3 Binding of NPs to serum albumin

The final objective about NPs is their *in vivo* utilization, which means intravenous or intra-abdominal injection which means in both cases that before reaching their target, NPs will react first with biological molecules present in the medium either blood on interstitial liquid. Almost any compound or drug used in medical application interacts with the proteins located into biological liquids. Serum albumin is the most abundant plasma protein. It is produced in the liver and forms a large proportion of all plasma proteins. In Human, serum albumin represents about 50% of human plasma proteins [116].

Albumin binds water, cations (such as Ca^{2+}, Na^{+} and K^{+}), fatty acids, hormones, bilirubin, thyroxine (T4) and pharmaceuticals. Since large abundance and high binding ability of albumin, the hypothesis of binding of NPs bovine serum albumin (BSA) was studied in the next experiments.

All of the tested NPs solutions absorb the light in visible range. Albumin solutions are transparent. The albumin can easily be precipitated by addition of ethanol to the solution. Addition of EtOH to NPs solution does not affect the stability of the tested colloids. So, in case of albumin binding, the NPs should co-precipitate with albumin.

A 40 mg/mL solution of bovine serum albumin (**A9418 Sigma**) in PBS was used. Mixtures were heated at 37°C for 90 min. After 18h Ethanol absolute was added to all of the solutions (final EtOH concentration is 25%). The albumin precipitates. After centrifugation at 2000g for 5 minutes, the albumin-contained samples have dark pellet and the supernatant became clearer, than control samples, suggesting that nanoparticles were bound to albumin. As one can see on

the **Figure 5.3.1** the CFO NPs, porous silicon and ablated Si samples are able to bind albumin and they precipitate with it. The nanodiamonds are not able to bind serum albumin.

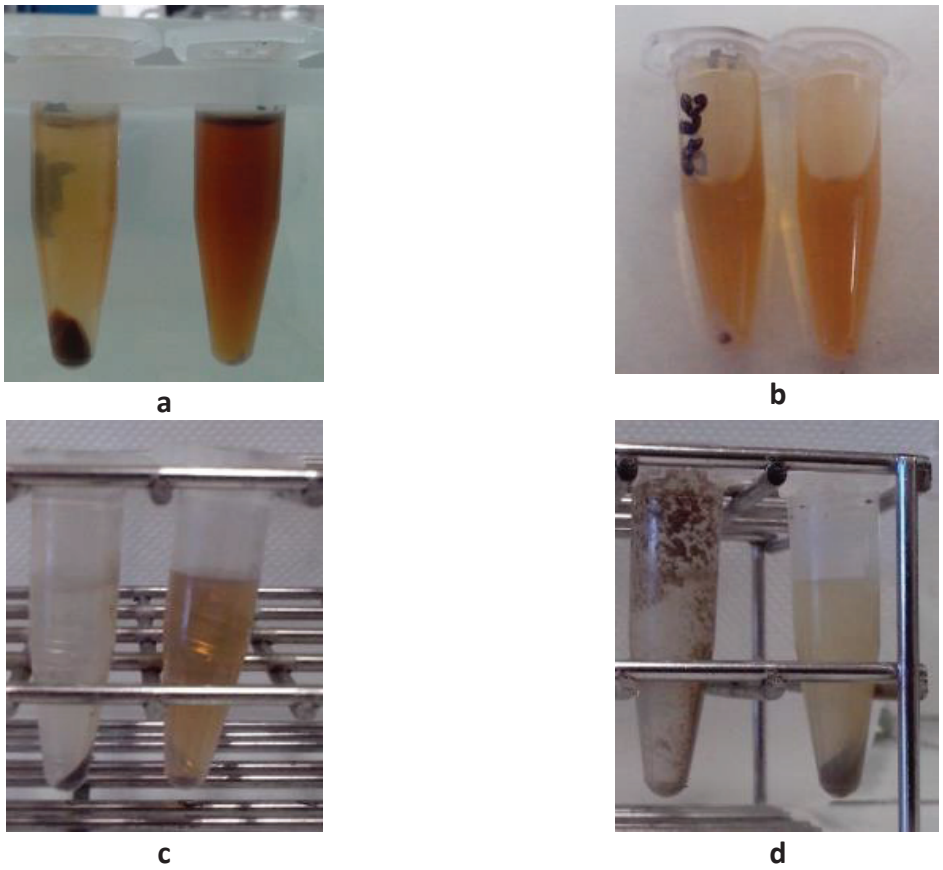

Figure 5.3.1 *NPs solutions after albumin precipitation with ethanol (left) and control (right) a – CFO NPs, b – Nanodiamonds, c – porous silicon, d – ablated Si.*

Albumin is the most abundant protein in blood and therefore the most important way of combination with the nanoparticles through reactions with amino or carboxyl terminating groups. In that case, if the binding is strong enough and irreversible, the preincubation of the nanoparticles with any aminoacid should decrease the binding rate due to the concurrent process. So, in case of non-site-specific albumin-binding preincubation of nanoparticles with any other amino acid (such as glutamine) can saturate the binding ability of CFO nanoparticles and decrease further albumin binding. So, the preincubation of the CFO, porous silicon and ablated Si NPs with 5mM glutamine followed by addition and precipitation of albumin gives the result on **Figure 5.3.2.**

a b C

Figure 5.3.2 *NPs solutions after albumin precipitation with ethanol (left samples preincubated with glutamine before the albumin addition). a – CFO NPs,b – porous silicon, c –, ablated Si*

Left sample is the NPs preincubated with glutamine for 90 min at 37^{o}C before the albumin binding. The most important difference can be seen at the **figure 5.3.2a**. The CFO nanoparticles after glutamine preincubation after albumin precipitation remains into the solution. It means that glutamine preincubation decreases the ability of the albumin binding of CFO nanoparticles. The absorbance studies of the CFO samples at 450 nm show that 100% of NPs left into the supernatant in control sample, 24% in case of albumin binding and 64% in case of glutamine preincubation of the samples. In order to check if protein binding plays a positive or negative role into the uptake of nanoparticles inside the cells, the next experiment on 3T3-L1 cells was performed. The uptake of CFO NPs was measured in PBS (contains neither proteins nor aminoacids), DMEM (contains aminoacids) and medium with serum (both aminoacids and proteins).

The quantitative analysis of luminescence intensities of the NPs inside the cells (**Figure 5.3.3**) shows that cells uptake more NPs in case of absence of serum. That proofs that all of the particles are able to penetrate inside the cells, but in case of albumin binding, the NPs lose their penetration ability.

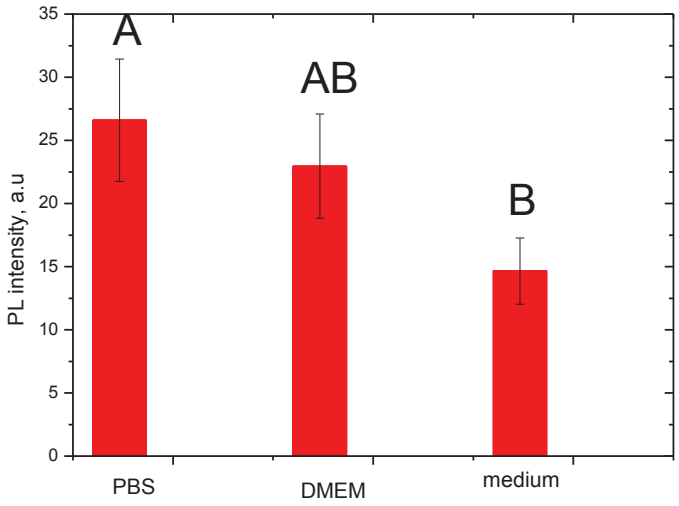

***Figure 5.3.3**: photoluminescence intensity analysis based on PL microscopy images for the 3T3-L1 cells exposed with 1g/L of CFO NPs for 4 hours in different media. The data are shown with subtracted background ± SD. There is no significant difference between the PBS and DMEM or medium and DMEM, but according to unpaired t-test the cells in PBS uptake more particles than in medium (99%).*

The uptake of NPs in PBS is similar to the one in DMEM. The NPs in albumin-containing medium cannot enter the cells with the same efficiency as in pure DMEM. That proves that the binding prevents the uptake of the NPs by the cells.

5.4 Discussion.

Comparison of NPs properties for cell imaging.

The all investigated group IV nanoparticles are able to be visualized inside the cells using the optical microscopy techniques. The CFO, nanodiamonds and porous silicon nanoparticles were observed using ordinary fluorescence microscope. Other particles, such as SiC can generate second harmonic. Bulk silicon are not able to produce SH signal, but 20-100 nm particles are able to generate weak SH signal due to surface effects (see chapter 1.3.3). So, the 20 nm Si and SiC nanoparticles can be observed using SH microscopy technique. Important properties for cell imaging are summarized in **Table 5.4.1**. All of the luminescent samples can be excited in 2photon way.

NPs	Size, nm	localization	lumine scence	2-photon excited PL	2nd harmonic generation
Nanodiamonds	6	Cytoplasm, uniform distribution	+	+	-
CFO	8	localized in nuclei (uniform distribution)	+	+	-
Porous Si	150	Mainly cytoplasm, not uniform	+	+	-
Ablated Si	20	Cytoplasm, not uniform	-	+	+
SiC	300	Mainly in membrane, few in cytoplasm, single particle can be seen	-+	+	+

Table 5.4.1*: comparison of the imaging properties of the tested nanoparticles for cell labeling.*

CFO and nanodiamonds can be used instead of ordinary organic dyes for labeling. Low toxicity at concentrations below 0.5 mg/mL for all of the tested nanoparticles, show the possibility to label the nuclei of the alive cells (proper labeling requires concentrations from 0.05 for SiC to 0.25 mg/mL for nanodiamonds CFO concentration should be above 0.1 mg/mL).

Toxicity of different NPs

The all of the abovementioned particles have relatively low toxicity compared to the other fluorescent dots, such as, for example Au dots. The dose, which causes the decrease of cell number, is shown on **Table 5.4.2**. Toxic concentrations of literature data are taken as IC50 concentrations.

NPs	Size, nm	toxic concentration, μg/mL	NPs	Size, nm	toxic concentration, μg/mL
Nanodiamonds	6	1000	SiC	300	>2000
CFO	8	1000	Au NPs [117]	20	10
Porous Si	150	2000	Carbon nanotubes	20	20

			[118]			
Ablated Si	20	500	Fe3O4 nanoparticles [119]	5	100	

Table 5.4.2*: toxic dose of the tested group IV nanoparticles (green) The red cells show the literature data on toxicity of most abundant inorganic NPs used in biology.*

Interesting, that the toxicity of silicon NPs does not depend on their size. The gold NPs, Fe_3O_4 and carbon nanotubes are added as a most frequently used for biological research inorganic particles. So, all of the particles investigated in this research (silicon carbon and SiC NPs) are hundreds times less cytotoxic. As it was shown in this research the typical time of the CFO nanoparticles uptake by the 3T3-L1 cells is 5 hours, which is typical time for the saturation of the cell by the some kinds of organic and inorganic nanoparticles. Panyam *et al.* investigated the dynamics of polymer nanoparticles uptake by the cells using endocytosis mechanism. They found that the typical time necessary to the uptake is close to 5 h, which corresponds to the value obtained into the current research [120]. Nevertheless, the particles which are uptaken by endocytosis mechanism, such as for example 40 nm silica particles [121] usually require more time (tenth of hours) to reach saturation. Fast kinetics is typical for the smaller particles, which penetrate the cell using passive diffusion mechanism. Also endosomal mechanism of uptake usually leads to the concentration of the particles inside endosomes and does not allow uniform distribution.

Albumin binding.

It was also found that all of the tested particles except nanodiamonds are able to bind plasma albumin. The CFO-albumin binding rate can be decreased by the preincubating of CFO nanoparticles with glutamine. That fact means that the nanoparticles surface can be saturated with other than albumin compounds. The interaction both with albumin and glutamine allows proposing that the CFO nanoparticles can bind unspecifically to albumin (protein) or glutamine (amino acid). We can propose that the CFO NPs can be easily conjugated not only with albumin but also with wide range of proteins. The strong protein binding usually leads to the accumulation of the particles into the liver or spleen [122]. Nevertheless, the preincubation of nanoparticles with some aminoacids, such as glutamine can open the interesting way for the drug delivery.

6 CFO nanoparticles for cell therapy.

Based on the interactions of NPs with cells, *in-vitro* experiments for cancer treatment with NPs were performed. Section 6.1 shows the different toxicities of CFO NPs for various cancer and non-cancer cell lines. It contains the quantification of such effect for CFO NPs. Section 6.2 demonstrates the possibility of application of CFO NPs as a sonosensitizer for ultrasound-assisted therapy.

6.1 Toxicity of the CFO particles on different cell lines

Figures 6.1.1 to 6.1.6 show the evolution of cell number curves of different cell lines during the 48 hours of the control period, the following 24 hours in presence increasing concentrations of CFO NPs and the following 24 hours after washing out NPs. Cell index values have been normalized at the time of CFO NPs addition. There was no slope change under basal conditions while there was a dose response effect of CFO NPs on cell index slopes, whatever are the cell lines tested. A stimulatory effect in presence of the lowest CFO NPs concentrations was observed only on 3T3-L1 cells. On all the other cell lines tested, the lowest concentrations had either no effect (HEK293, Panc01, HepG2) or decreased cell proliferation (HSC, HuH7). CFO NPs concentrations above 0.25 mg/mL reduced the cell proliferation. Generally, the higher is the CFO NPs concentration, the higher the decrease in cell index slope. The highest concentration of nanoparticles (1.5 mg/mL) significantly decreased cell proliferation in all the cell lines tested. Dose response histograms of the effects of CFO NPs on cell index are shown in **Figures 6.1.1 to 6.1.6** (left histogram).

Thanks to the xCELLigence system which allows the realtime analysis, it is also possible to study the effect of CFO NPs after washing them out. In that case, only the effects of uptaken CFO NPs are observed. We compared the slopes of cell proliferation during exposure and after washing out (**Figures 6.1.1 to 6.1.6,** right histograms). Interestingly, after washing out, since cell proliferation did not restart and cell values index were close to zero, it appears that the highest concentration of CFO NPs killed the cells in all the cell lines except in 3T3-L1 (Figure **6.1.1**, cell index). In most cell lines, cells restarted to proliferate after washing out at concentrations equal or lower to 1 mg/mL. A dose response effect of CFO NPs on cell proliferation after washing out can be observed in HSC, Panc01 and HepG2 (**Figures 6.1.3, 6.1.5, 6.1.6** lower histogram).

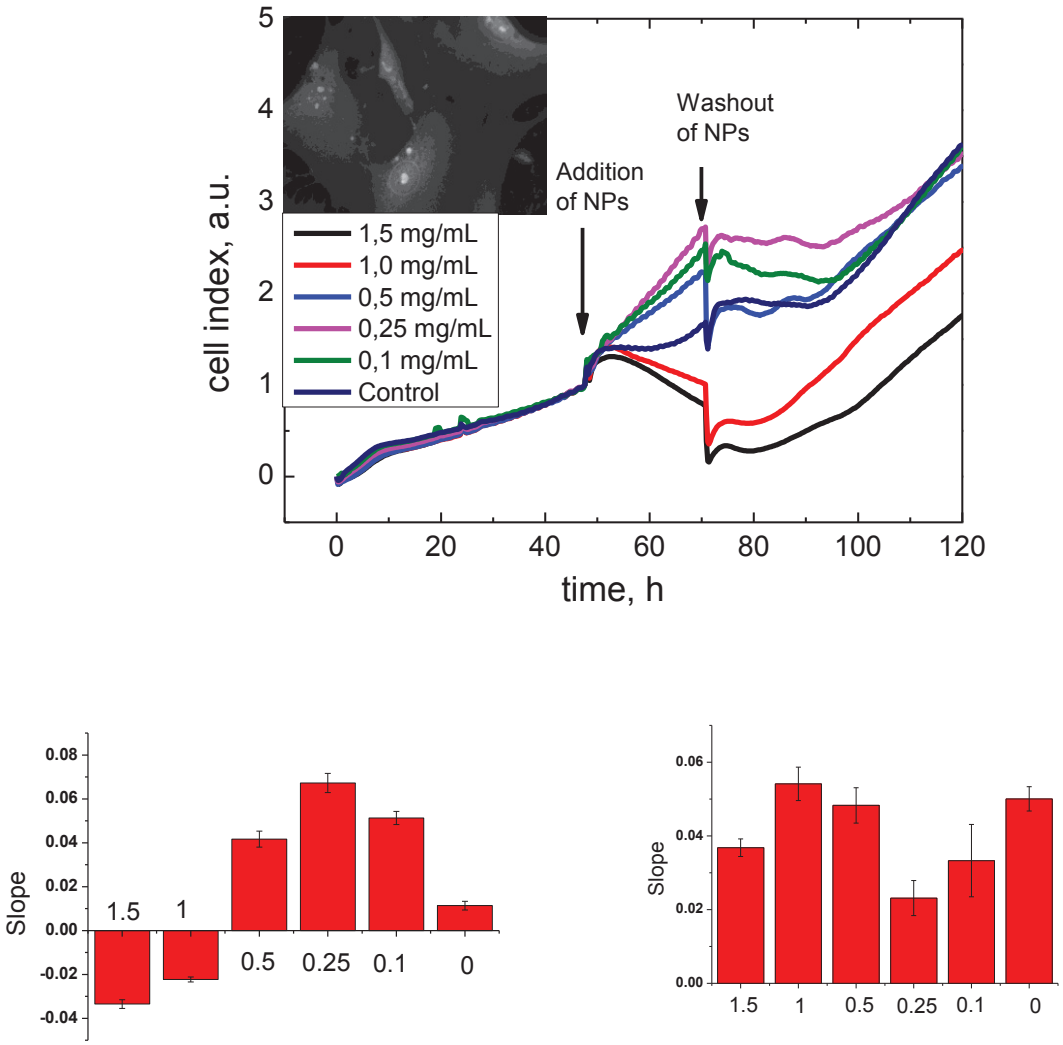

Figure 6.1.1: *the cell index curves for 3T3-L1 cells in presence of increasing concentrations of CFO NPs. Arrows show the time of NPs addition and washing out. Inset shows the photoluminescent image of the cells exposed with 0.25mg/mL CFO NPs for 4h. Histograms represent the cell index curves slope in response to increasing CFO NPs concentrations (from 52h to 64h) (left) and after washing out (from 90h to 102h) (right).*

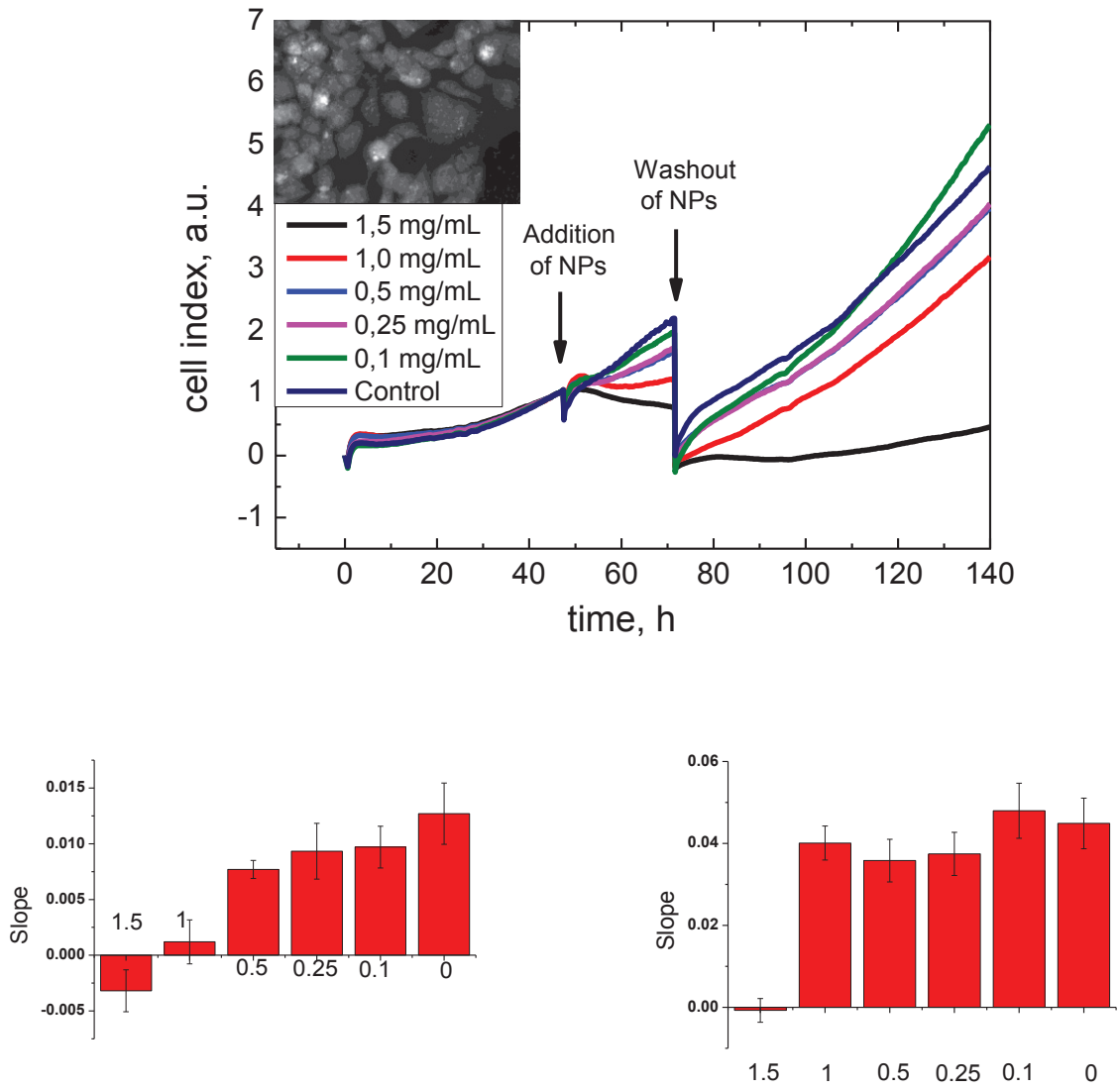

Figure 6.1.2: *the cell index curves for Hek293 cells in presence of increasing concentrations of CFO NPs. Arrows show the time of NPs addition and washing out. Inset shows the photoluminescent image of the cells exposed with 0.25mg/mL CFO NPs for 4h. Histograms represent the cell index curves slope in response to increasing CFO NPs concentrations (from 52h to 64h) (left) and after washing out (from 90h to 102h) (right).*

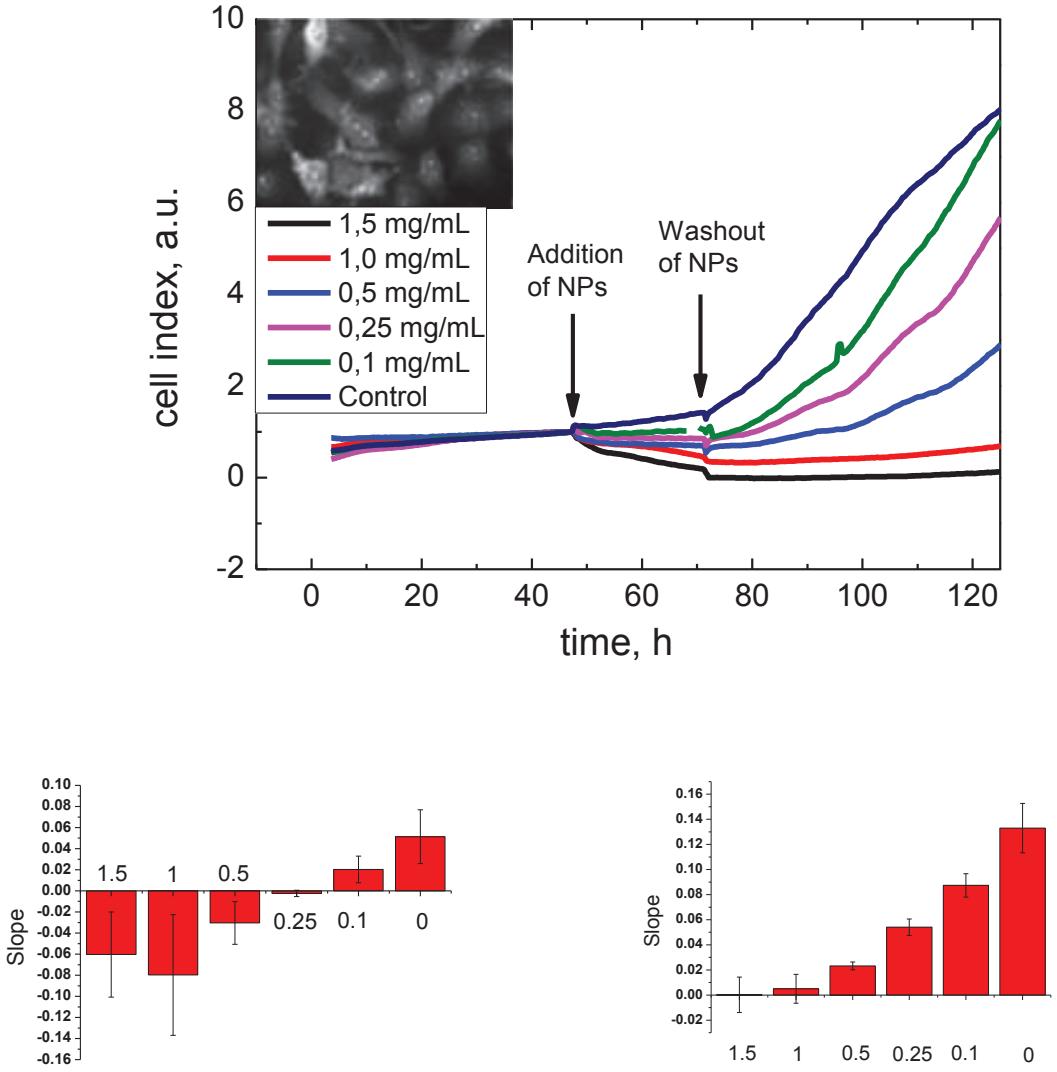

Figure 6.1.3: *the cell index curves for HSC cells in presence of increasing concentrations of CFO NPs. Arrows show the time of NPs addition and washing out. Inset shows the photoluminescent image of the cells exposed with 0.25mg/mL CFO NPs for 4h. Histograms represent the cell index curves slope in response to increasing CFO NPs concentrations (from 52h to 64h) (left) and after washing out (from 90h to 102h) (right).*

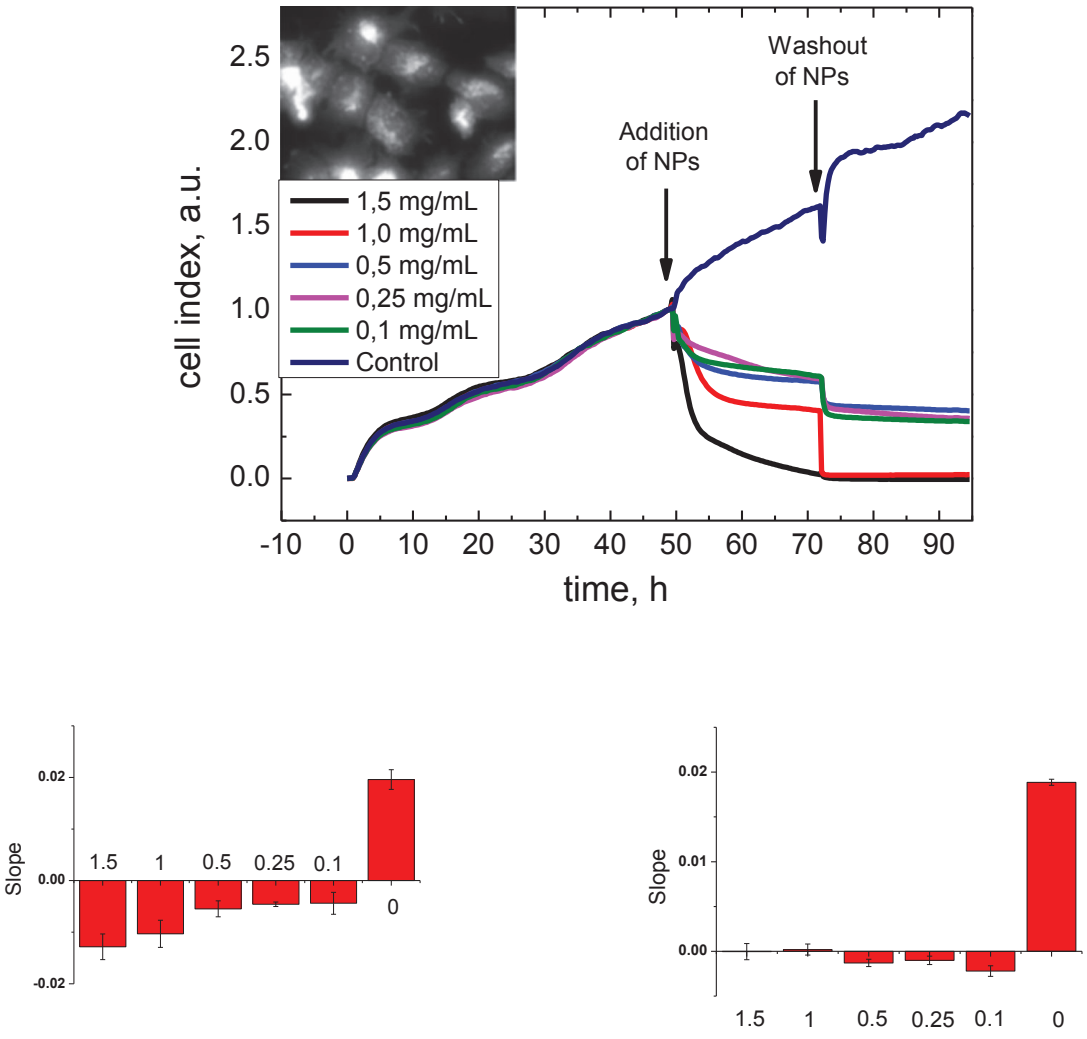

Figure 6.1.4: *the cell index curves for HuH7 cells in presence of increasing concentrations of CFO NPs. Arrows show the time of NPs addition and washing out. Inset shows the photoluminescent image of the cells exposed with 0.25mg/mL CFO NPs for 4h. Histograms represent the cell index curves slope in response to increasing CFO NPs concentrations (from 52h to 64h) (left) and after washing out (from 90h to 102h) (right).*

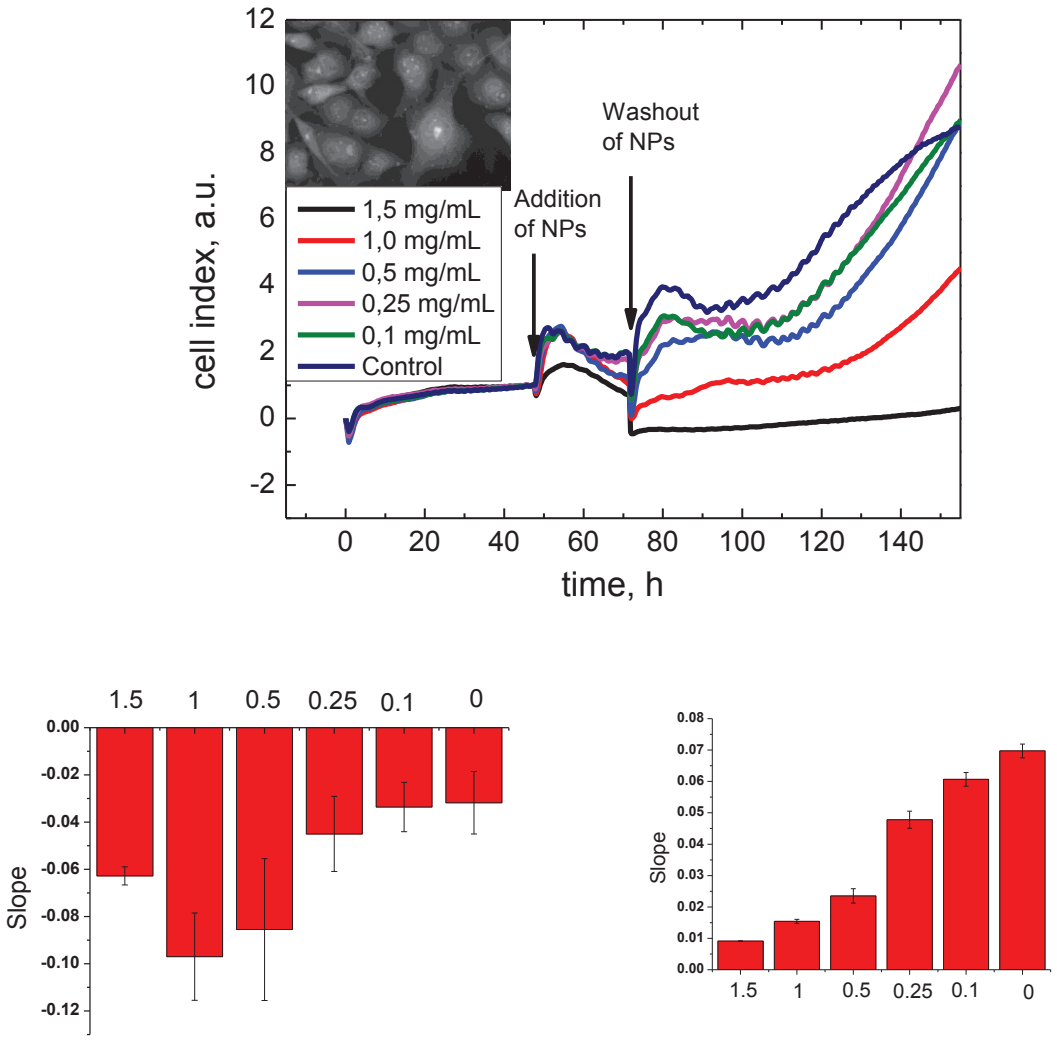

Figure 6.1.5: *the cell index curves for PANC1 cells in presence of increasing concentrations of CFO NPs. Arrows show the time of NPs addition and washing out. Inset shows the photoluminescent image of the cells exposed with 0.25mg/mL CFO NPs for 4h. Histograms represent the cell index curves slope in response to increasing CFO NPs concentrations (from 52h to 64h) (left) and after washing out (from 90h to 102h) (right).*

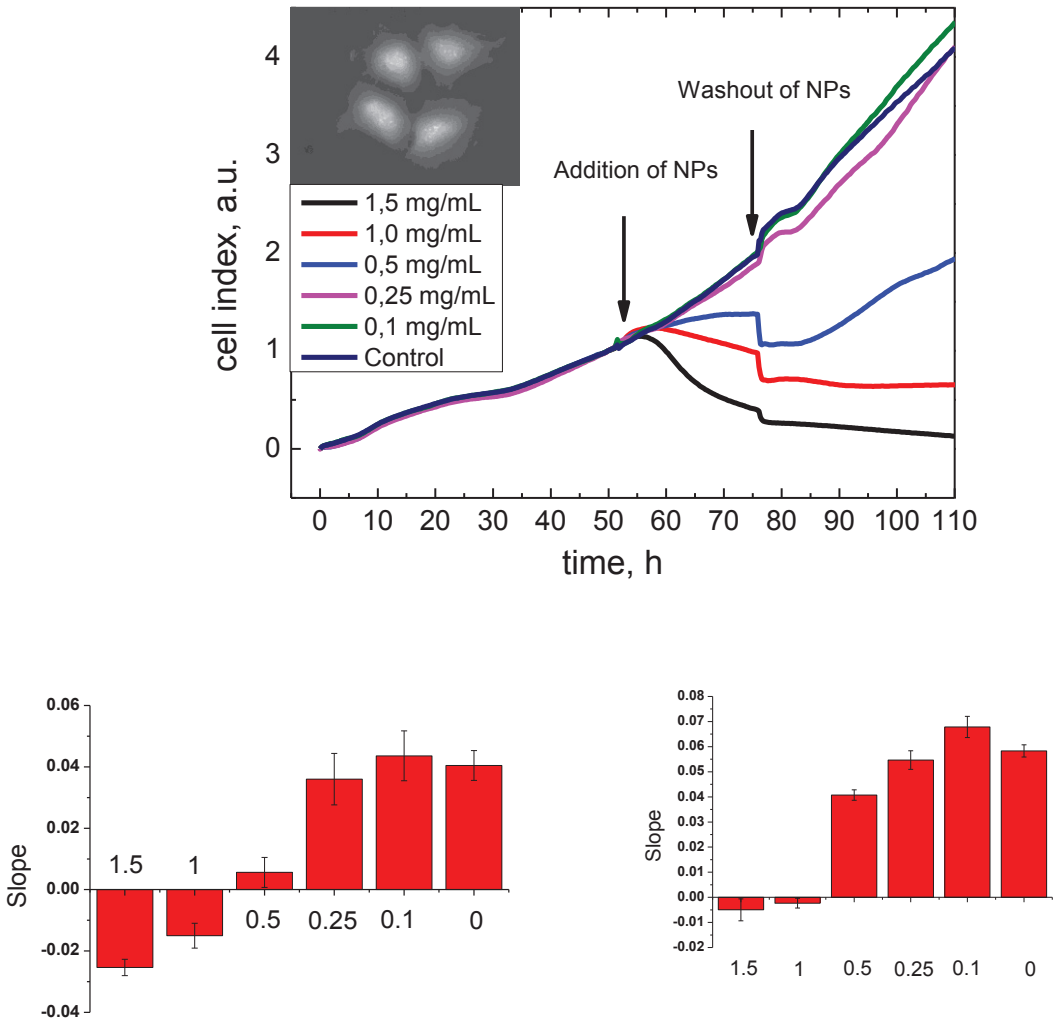

Figure 6.1.6: *the cell index curves for HepG2 cells in presence of increasing concentrations of CFO NPs. Arrows show the time of NPs addition and washing out. Inset shows the photoluminescent image of the cells exposed with 0.25mg/mL CFO NPs for 4h. Histograms represent the cell index curves slope in response to increasing CFO NPs concentrations (from 52h to 64h) (left) and after washing out (from 90h to 102h) (right).*

The statistical significance of the mean difference of the histograms is shown at supplementary materials (**Tables 8.1-8.6**) at the end of thesis. It is seen on **Figures 6.1.1-6.1.6** that CFO nanoparticles in small concentrations are able to stimulate the growth 3T3-L1 cells. There is no such effect on cancer cell lines. Other interesting observation is that after washing out CFO NPs from 3T3-L1 and Hek293, these cells restarted their proliferation even after exposure at the highest concentrations (1.5 mg/mL) which was not the case for cancer cell lines. In order to quantify the difference in behavior of the cells response to NPs we use the initial evolution curves at the constant concentrations.

Generally, the higher is the CFO NPs concentration, the higher the decrease in cell index slope. The highest concentration of nanoparticles (1.5 mg/mL) significantly decreased cell proliferation in all the cell lines tested. It can be seen in the insets on **Figures 6.1.1 to 6.1.6**, that in accordance with the previous researches, they predominantly accumulate inside the nuclei of either cancer or non-cancer cells [123].

In order to compare the toxicity of nanoparticles for different cell lines, the cell death factor (CDF) parameter has been chosen. CDF is a relative decrease of the cell index slope

$$CDF = \frac{slope(control) - slope(1.5g/l)}{slope(control)}$$

So, CDF=0 means no effect of nanoparticles, CDF=1 is complete stop proliferation, CDF>1 shows the relative cell death rate.

To test our experimental hypothesis that CFO NPs toxicity is higher when the proliferation rate is higher, we plot the doubling time versus CDF after addition of NPs chart (**Figure 6.1.7**). The CDF on **Figure 6.1.7** was measured for different cell lines for the highest concentration of nanoparticles (1,5 mg/mL). X axis represents the initial proliferation growth speed, which is a characteristic of the cell line. The dash line is a tendency curve. It can be easily noticed that there is correlation between the cell death factor and the doubling time. Generally, the faster is cell proliferation, the more toxic are the nanoparticles for such cell line. That effect can be explained by the increased uptake of NPs and, as a result the higher susceptibility to the NPs exposure.

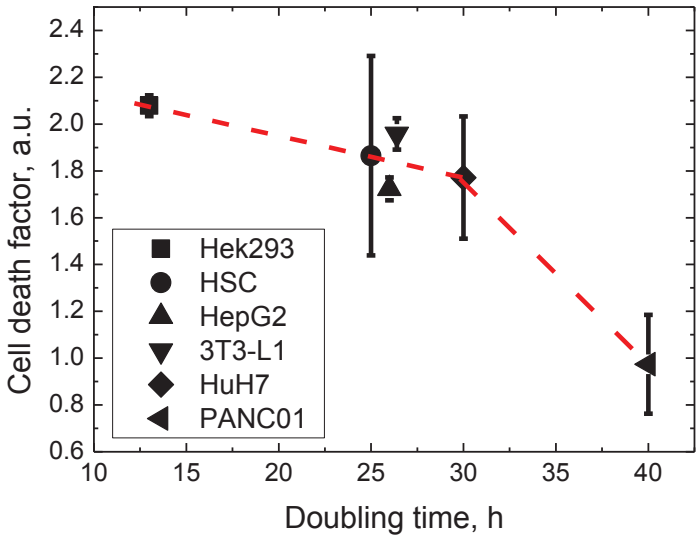

Figure 6.1.7: *correlation between cell death factor (= the toxicity of CFO NPs at 1.5 mg/mL)*

and doubling time. Dashed line is a tendency curve. Each point is the average of 8 measurements ± SEM.

The present study emphases the fact that it is important to study, not only the effect of addition of NPs on cell culture but also the behavior of cells after washing out the NPs. That difference is important for the extrapolation from *in vitro* to *in vivo* studies. Indeed, under *in vivo* experiment, the extracellular concentration of NPs is not supposed to remain high for a long time. NPs will be uptaken by cells, more or less rapidly; it is only the uptaken NPs that will change the behavior of exposed cells. Thanks to the xCELLigence system which allows the realtime analysis, it is also possible to study the effect of CFO NPs after washing out. In that case, only the effects of uptaken CFO NPs are observed.

For such observation, the cell index behavior after washing out was measured for different cell lines. The cell index evolution after washing NPs out is shown on the **Figure 6.1.8a.** All of the values are normalized at the time of NPs wash out. In the present case, there is a striking difference after washing out in 3T3-L1 and the other cell lines.

Since the differences in cytotoxicity after washout is supposed to rely on different capacities to uptake NPs, the relative amount of the nanoparticles uptaken by the cells should be measured. As have been seen in the chapter 5 CFO NPs are mainly localized inside the cell nuclei. This confirms our previous studies [124]. NPs uptake is not related to the temporary disappearance of the nuclear membrane during cell division. Indeed, significant NPs uptake are observed in only 3 hours of exposure, while a complete cell division cycle requires around 20 hours to be completed. The reason why CFO NPs concentrate inside cell nuclei only when cells divide is not yet known. The mean size of CFO NPs is very small (lower than 10 nm) which may explain why there can easily migrate inside cell nuclei. Nevertheless the small size is not a sufficient criterion to allow nuclear uptake. Indeed, we have recently shown that the surface charges are equally important, since strongly positive surface charged CFO NPs cannot penetrate inside cell nuclei [65].

The luminescence images were made using the same conditions to compare the uptake of nanoparticles by different cell lines by comparing the luminosity per cell. The results of such comparison, based on measurements of at least 20 cells are shown in **Figure 6.1.8 b.** It can be seen that the 3T3-L1 cells uptake much less nanoparticles, than the other cell lines (Statistical significance analysis is given at the supplementary section). For the comparison of the cell proliferation after washout for different cell lines, cell recovery factor (CRF) was calculated. CRF is a relative recovery of the cell index slope after wash out.

$$CRF = \frac{slope(1.5\ g/l\ after\ washout)}{slope(initial)}$$

For proper comparison, all the slopes were measured on normalized on the cell index immediately after washout curves.

There is an evident correlation between the NPs uptake rate and the toxicity of the particles inside the cells (**Figure 6.1.8 c**). The 3T3-L1 cells do not uptake much NPs, and, as a result their cell proliferation restarted after washout. PANC01, Hek293 and HSC cells uptake more nanoparticles and cell proliferation restarted with much lower rate than the one of 3T3-L1. HepG2 and HuH7 cancer cells uptake more NPs than other cell lines and as a matter of fact, their cell proliferation did not restart after washout. Since nanoparticles cause a selective toxic effect for cancer cells compare to control cell lines, they can be useful for cancer therapeutics.

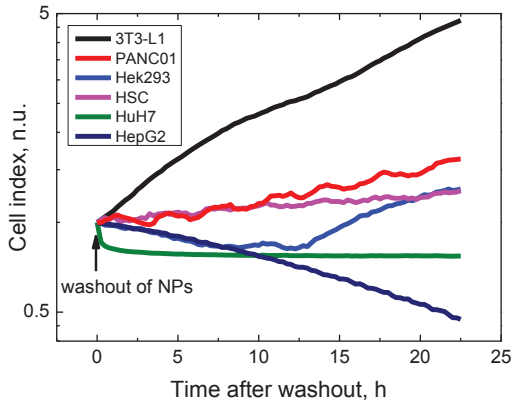

a

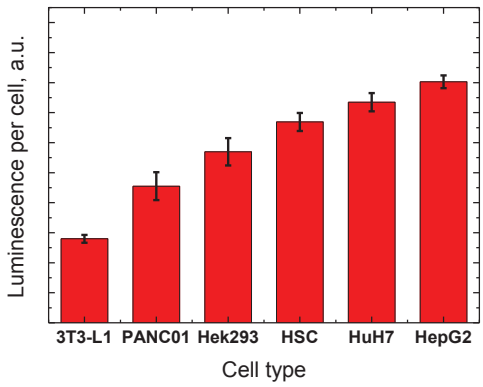

b

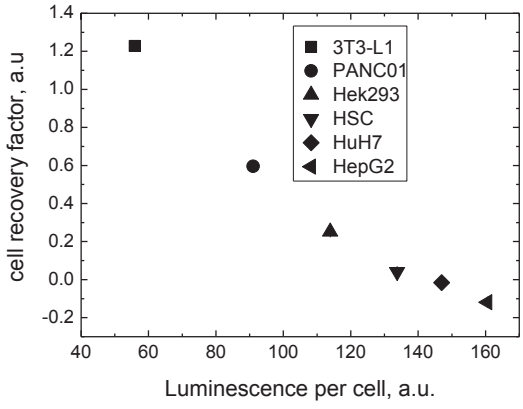

c

Figure 6.1.8: *a – cell index evolution for different cell lines after washing out the 1.5 mg/mL of nanoparticles. Cell indexes were normalized at the time of washout. b - Average amount of the NPs uptaken by the cells, measured by the luminescence per cell for different cell types exposed to NPs for 4 h at 0.25 mg/mL. Each column is a result of*

averaging at least 20 cells. Data are shown with ± SEM. c- Correlation between the luminosity per cell (relative uptake) and slope of cell index curve after washing out.

6.2 CFO nanoparticles for ultrasound-assistant therapy.

CFO NPs can be used as very efficient theranostic agents both for one- and two-photon excited luminescence cell imaging and as sonosensitizers for ultrasound-assisted therapy.

Since the NPs can be used as both fluorescent probes and sonosensitizers, they are very attractive agents for imaging and therapy of cancer. As it has been shown previously, localization of the NPs inside the cells depends on their surface charges [122]. Indeed, if the main therapeutic factor is related to the destruction of chromosomes, the NPs accumulated inside the nuclei will ensure the strongest killing effect compared to those accumulated into the cytoplasm. Fluorescence of the NPs allows non-destructive estimation of their localization before the ultrasound treatment.

3T3-L1 (fibroblasts) and HuH7 (hepatocarcinoma) cells were grown in culture medium. The cells were trypsinized and 2500 cells were added to each well of a xCELLigence 96-well plate for cell proliferation measurements. Then the cells were incubated for 48 h. CFO NPs with concentration of 0.25 mg/mL were added to the cell cultures which were additionally incubated for 24 h. Before acquisition of fluorescent image of the cells, the NPs were washed out from the extracellular environment with phosphate-buffered saline.

The preferential accumulation of the CFO NPs in the cell nuclei was confirmed once again.

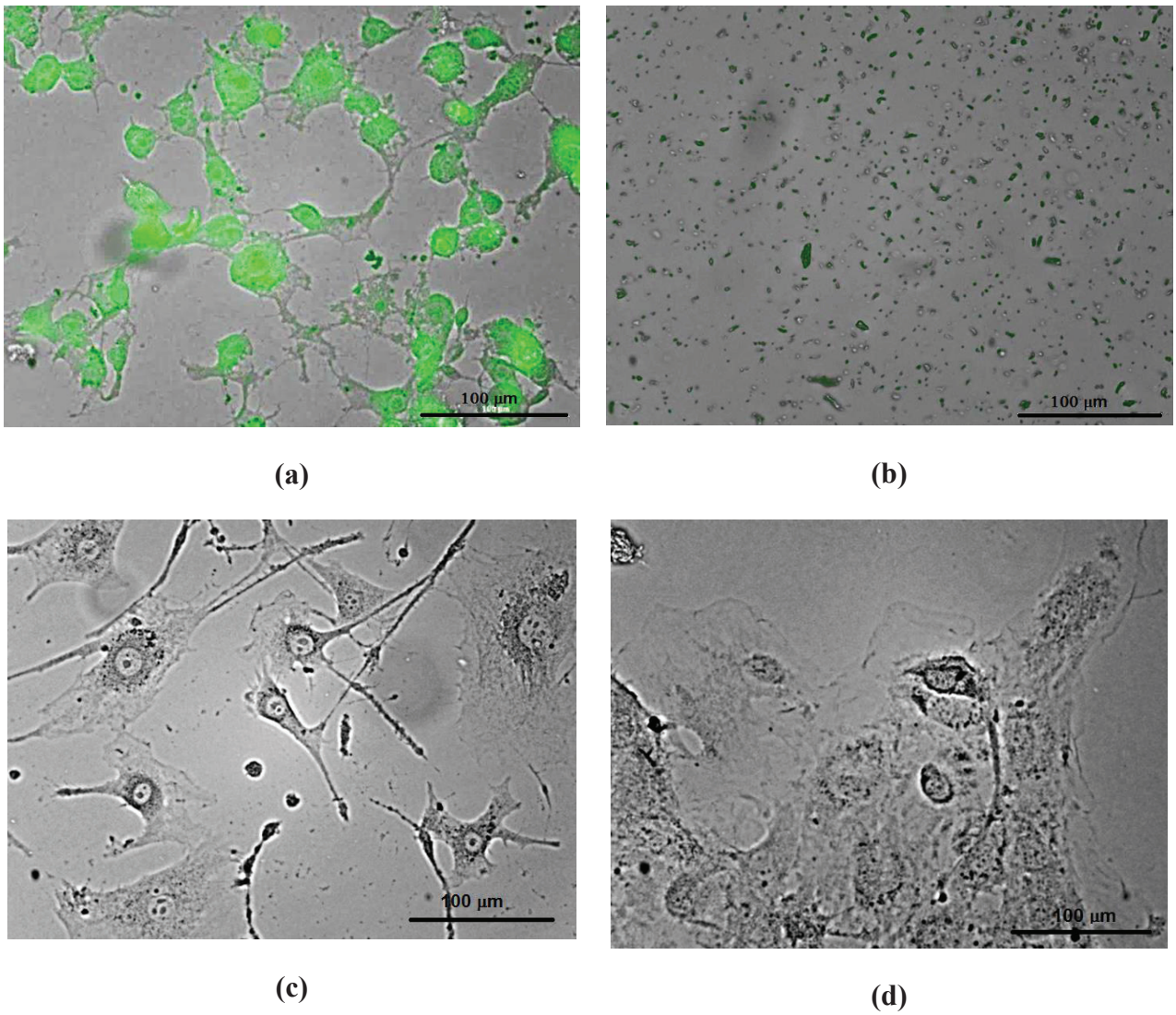

(a) **(b)**

(c) **(d)**

Figure 6.2.1*: 3T3-L1 cells labeled with CFO NPs (1 mg/mL) before (a) and after (b) ultrasound treatment. Non-labeled 3T3-L1 cells before (c) and after (d) ultrasound treatment are shown for comparison.*

As it is illustrated in **Figure 6.2.1**, ultrasound treatment (40 kHz, power density: 0.4 W/cm^3, time: 10 min) of the cell cultures labeled with the luminescent CFO NPs leads to their complete destruction (**Figures 6.2.1 a** and **6.2.1 b**) while the non-labeled cells remain undamaged (**Figures 6.2.1 c** and **6.2.1 d**). Thus, the CFO NPs are shown to be able to play a double role of one- or multi-photon excited fluorescent labels as well as of ultrasonic sensitizers selectively destroying only the labeled cells.

In order to check the effects of NP toxicity as well as of ultrasound treatment on the labeled and non-labeled cells, time evolution of the cell numbers was studied by means of xCelligence system. **Figure 6.2.2** shows time dependence of cell index. Arrows indicate the

moments when the CFO NPs are added to cells and ultrasound treatment is switched on for 10 minutes. Red lines correspond to the cells labeled with the fluorescent CFO NPs and blue ones – to control cell lines (without NPs). After ultrasound treatment, number of the labeled 3T3-L1 cells goes down rapidly because of their significant destruction described above while proliferation velocity of a control (non-labeled) cell line is completely restored. The similar effects are observed in the case of cancer cells (**Figure 6.2.2 b**). Thus, one can conclude that the NPs and ultrasound treatment alone have no toxic or damage effect on the cells, while their combined action provokes significant cell injuring which can be efficiently used for theranostic purposes.

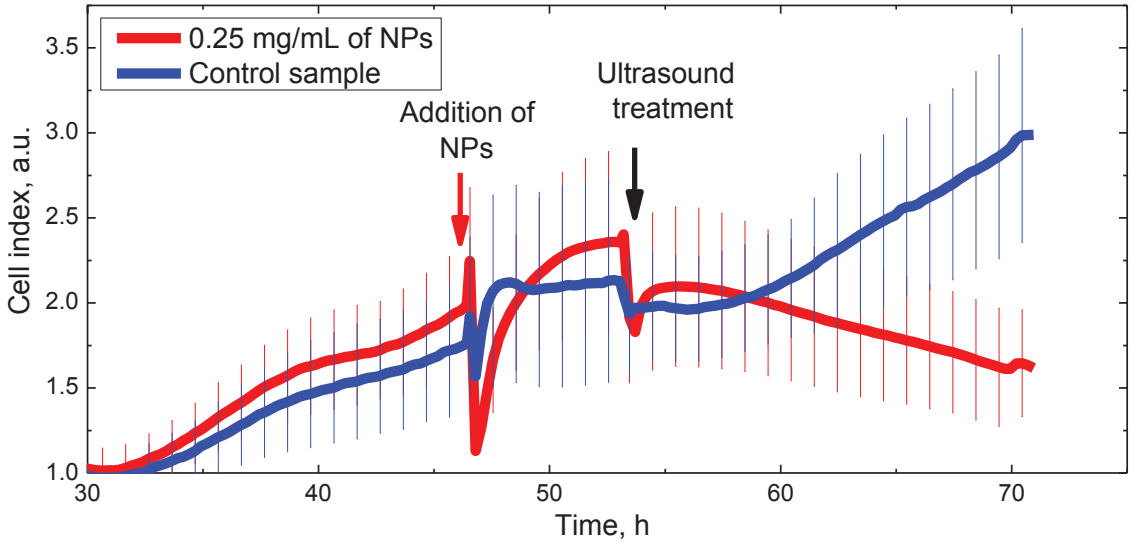

(a)

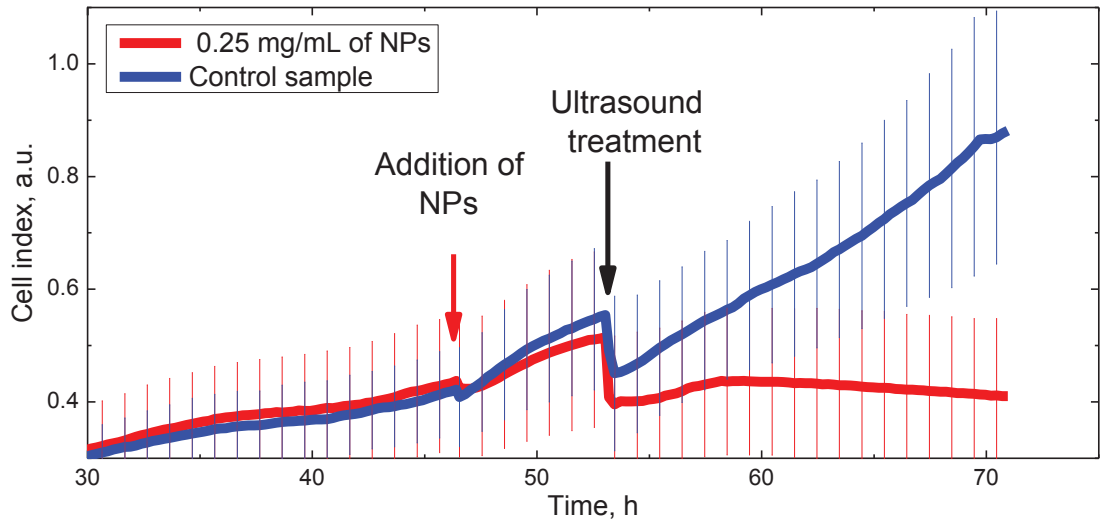

(b)

Figure 6.2.2*: in-time evolution of the cell number: (a) 3T3-L1 cell line; (b) HuH7 cancer cell line. Arrows show when the CFO NPs are added and ultrasound treatment is switched on.*

6.3 Discussion of chapter 6.

We have investigated the toxicity of CFO nanoparticles on different cell lines. We think that the measure of the direct cytotoxicity of NPs on cells is a too far simplistic estimation of NPs toxicity. Indeed, the in vivo utilization of NPs means that the extracellular NPs concentration will be increased for a limited period of time. Cellular uptake of NPs will take place only when the extracellular concentration of NPs is high enough. One can estimate that 24 hours is a reasonable in vivo washout time, suggesting that after one day most of the NPs have disappeared from the extracellular compartment. Under these conditions, most of the toxic effect of the NPs will result from the intracellular accumulation of NPs. In consequence, it is of major importance to test the NPs toxicity after their washout from the culture medium because it represents their true cytotoxicity. Also, that toxicity is directly dependent on the cellular uptake of NPs.

In general, the higher is the proliferation rate, the more toxic are the particles. But in case of short exposure with the nanoparticles and washing them out, which is more similar to the physiological conditions, we can see the other behavior; the cell recovery rate after exposure correlates with the number of the uptaken particles, but not with the initial cell proliferation rate. (**Table 6.3.1**).

CFO nanoparticles are less toxic for control cells (3T3-L1) than for the cancer cell lines ((HSC, HuH7, Panc01, HepG2). That effect mainly results from a lower uptake capacity by control cell lines compared with the one of cancer cell lines. Although the reason why CFO NPs uptake is increased in cancer cell lines, is yet unknown, these results support the utilization CFO nanoparticles for anti-cancer therapy.

Parameter	**Correlated with**
Doubling time	CDF (toxicity during exposure)
Uptake	Recovery of proliferation after washout

Table 6.3.1*: toxicity during exposure and after NPs washout is correlated with different cellular parameters*

Interesting results concern to the different action of CFO NPs on cancer and non-cancer cell lines. It was found that CFO nanoparticles are more toxic for cancer cell lines, than for non-cancer ones.

That result seems to be promising, but the different toxicity could be caused by reasons independent of cancer, for example by the origin of the cell lines. Indeed, hepatocytes may be more susceptible for the NPs, than fibroblasts. Moreover, under physiological conditions, it will be very difficult to not reach the high NPs concentrations.

The second main achievement is that *in vitro* cell tests were carried out to investigate the feasibility of ultrasound-assisted (40 kHz) treatment for cancer therapy based on the use of the CFO NPs. In particular, the ultrasound treatment of cell lines labeled with fluorescent NPs leads to cell death, contrary to the non-labeled cells. The cell lines labeled with an 0.25 mg/mL of the CFO NPs can even provoke a complete destruction of the cells under the ultrasound treatment. However, an *in vivo* systematic administration of NPs on specific sites still remains an important challenge for this therapeutic approach.

The experiments show the high in vitro efficiency of ultrasound-treatment combined with the CFO nanoparticles. The efficiency of ultrasound destruction greatly increases with the presence of NPs than without of them. Even the relatively small amount of CFO NPs is enough to sensitize the ultrasound. So, method of ultrasound-assistant cancer treatment can provide the higher selectivity than the intrinsic selectivity of the nanoparticles for cancer cells. Very small labeling is possible to reach inside the organism without of any toxic effect. The ultrasound can be applied directly to the tumor. The localization of the strong ultrasound wave inside the body is widely used for the ultrasonic lithotripsy method or the High-intensity focused ultrasound technique, ordinary used for cancer treatment.

Therefore, the non-invasive localization of ultrasound is an already solved task. The ultrasound power densities usually reached inside the body during medical cancer treatment are up to 500W/cm^2 [125] which is more than 1000 times higher than the power density used in our experiments. That shows the great potential for the ultrasound-assisted treatment and using CFO NPs for cancer therapy.

7. Conclusion.

Aim of this research was to compare the possibilities of bioapplications for different types of group IV nanoparticles and to understand which properties can define the specific applications of those particles.

All of the tested nanoparticles confirm their advantages as agents for bioapplications. They all have low cytotoxicity rate, the difference in size can be used for the specification of the applications. The group IV nanoparticles have flexible surface chemistry which can be easily manipulated. The nanoparticles can effectively interact with the light. They have high absorption rate into the UV range and several kinds of them have strong photoluminescence ability. Some of the nanoparticles are able to produce non-linear response on excitation both in terms of 2-photon excitation or second harmonic generation. Particularly, the multifunctionality of group IV nanoparticles can be shown by the comparison of different pairs of nanoparticles.

1. The comparison of porous silicon and 20 nm silicon NPs shows that the small particles have better penetration ability to the cells and due to high PL efficiency, they can be used as a luminescent labels. The bigger particles have lower uptake but due to their size some non-linear properties can be observed. So the 20 nm silicon particles can be used for SH microscopy contrast agents.
2. Comparison of SiC and Si particles show the different efficiency of group IV nanoparticles for imaging in different modalities. SiC nanoparticles were found extremely efficient as non-linear agents but they have weak photoluminescence. The Si nanoparticles are less efficient second harmonic generators. That difference is defined by the different structure of silicon and silicon carbide. 3c-SiC nanoparticles and silicon nanoparticles have similar crystal lattices, but half of the Si atoms in case of the 3c-SiC is changed by carbon ones, which causes non centrosymmetrisity and, as a result –increase of nonlinear characteristics.
3. The porous silicon particles and nanodiamonds have the same crystalline structure and similar crystallite sizes. Due to different agglomeration ratio, the porous silicon particles are less permeable through the cell membrane than nanodiamonds. The significant difference is also the PL spectral range, which is close to infrared for porous silicon and green in case of nanodiamonds.
4. The comparison of crystalline and non-crystalline forms of nanocarbons- nanodiamonds and carbon fluorooxide particles show small difference in the PL spectral characteristics. Both nanodiamonds and CFO nanoparticles can absorb the IR light using 2photon absorption mechanism. The strict difference was found into localization of the

nanodiamonds and CFO particles inside the cells. Nanodiamonds label the cell cytoplasm, while the CFO nanoparticles are predominantly accumulated inside the nuclei of cells. The localization of the CFO nanoparticles inside the nuclei of cell shows the potential of their utilization for specific bioapplications, such as cancer therapy.

So, the CFO nanoparticles were chosen as an agent for possible cancer therapy. It was found that the nanoparticles itself have the selectivity for cancer cells.

Other way for cancer treatment uses the localization of CFO NPs inside the cells. The CFO NPs can be used as a sonosensitizers for the ultrasound. Despite the low concentration of nanoparticles (4 times less than toxic one) inside the cells, they can be activated using weak ultrasound treatment. The ultrasound power with 1000 times less intensity than the US used for medical applications can cause the destruction of the cells with the nanoparticles inside. Since there is no problem to localize the ultrasound inside the body with very good precision, that method can be very effective for cancer treatment. The predominant localization of CFO in cancer cells can increase selectivity of that cancer treatment method.

Nevertheless there are some challenges concerning the current topic that have to be overcome. Complicated molecular structure of CFO nanoparticles leads to the problem of standardization. That is difficult to estimate its exact composition. That reason can also lead to low reproducibility in the CFO composition. The method of the CFO production can be improved.

The ultrasound action was checked on the NPs inside the cell nuclei and absence of NPs in medium. It is possible to determinate if the particles outside the cells will have the same destructive effect under ultrasound irradiation or not.

The mechanism of NPs migration to the nuclei remains unclear and the penetration of the nanoparticles into the nuclei can help to understand the mechanisms of nuclear transport.

8. Supplementary data

The toxicity surfaces plotted in the coordinates of Time-concentration – cell index for different cell lines and CFO nanoparticles is shown at **figure 8.1.** Arrows show the time of the NPs addition and washing out.

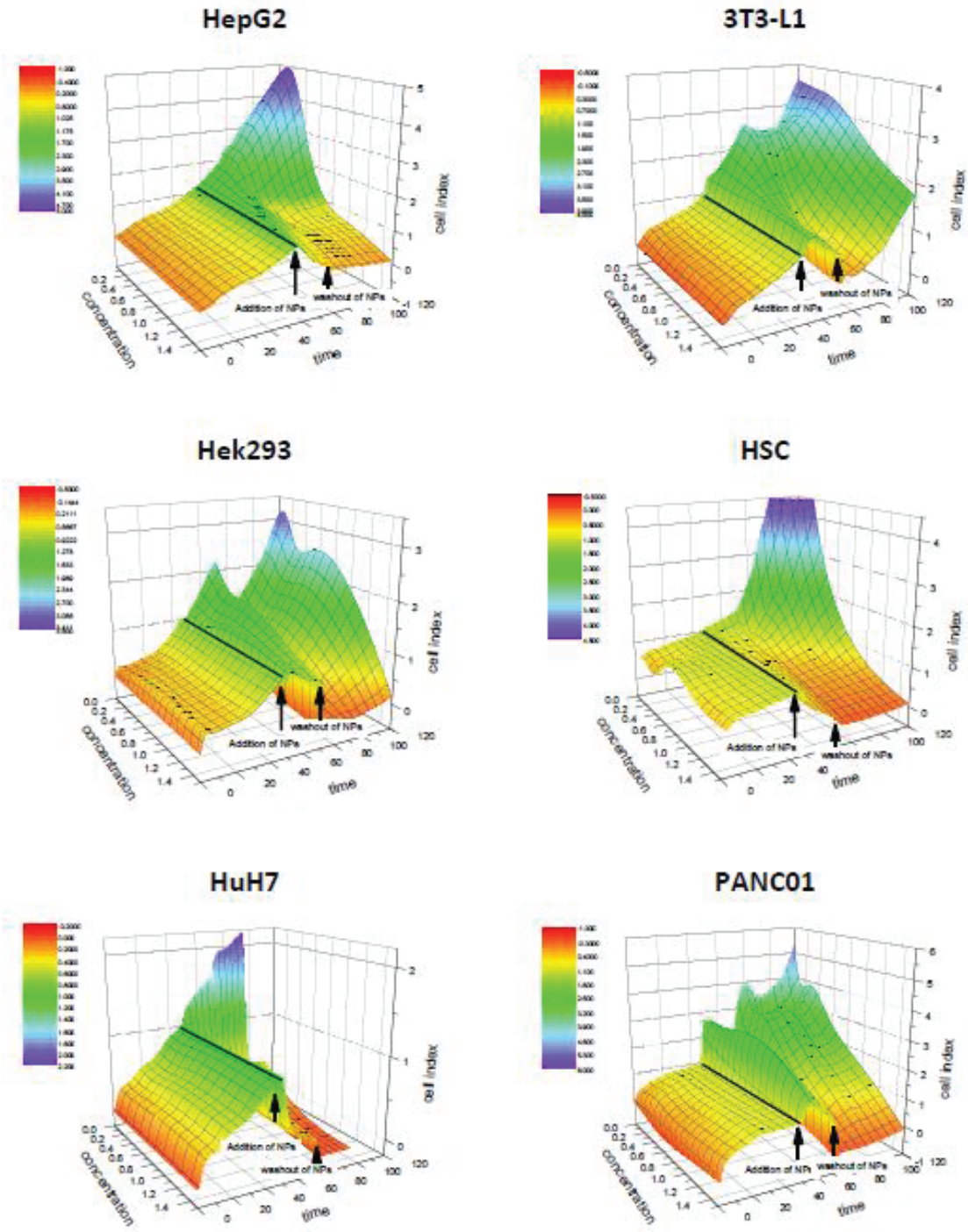

Figure 8.1 *The toxicity surfaces of the CFO NPs (based on* ***figures 6.1.1-6.1.6****)*

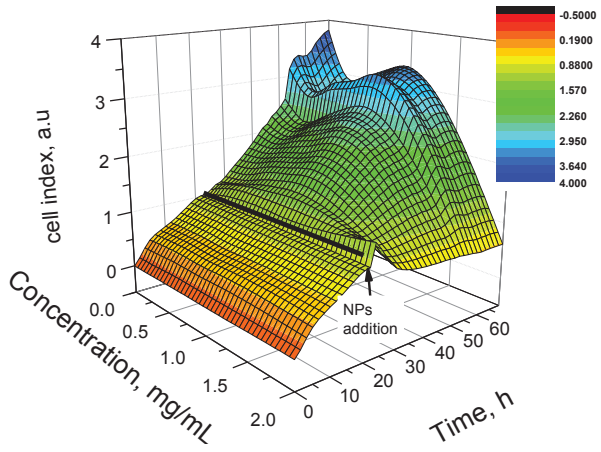

Porous silicon

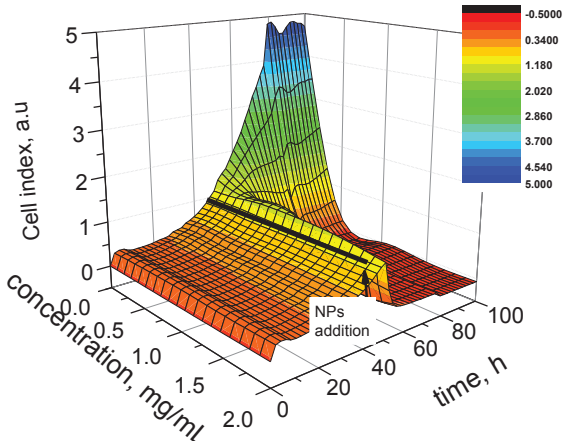

Si 20 nm

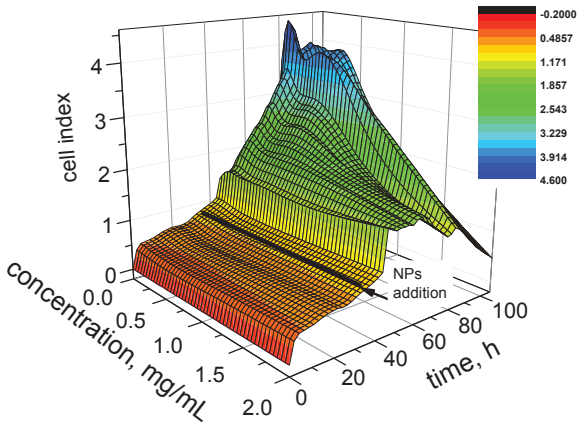

nanodiamonds

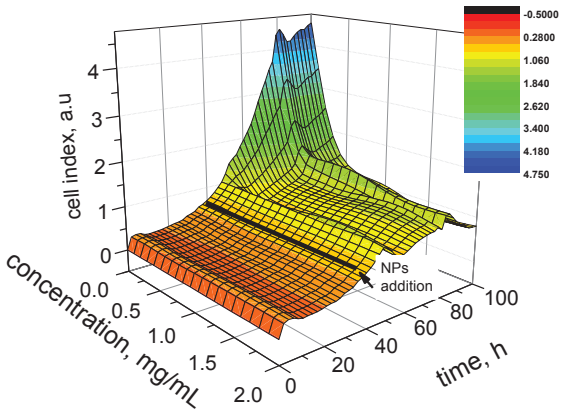

SiC

Figure 8.2 *The toxicity surfaces of the different nanoparticles on 3t3-L1 cells (based on* ***figure 5.2.5****)*

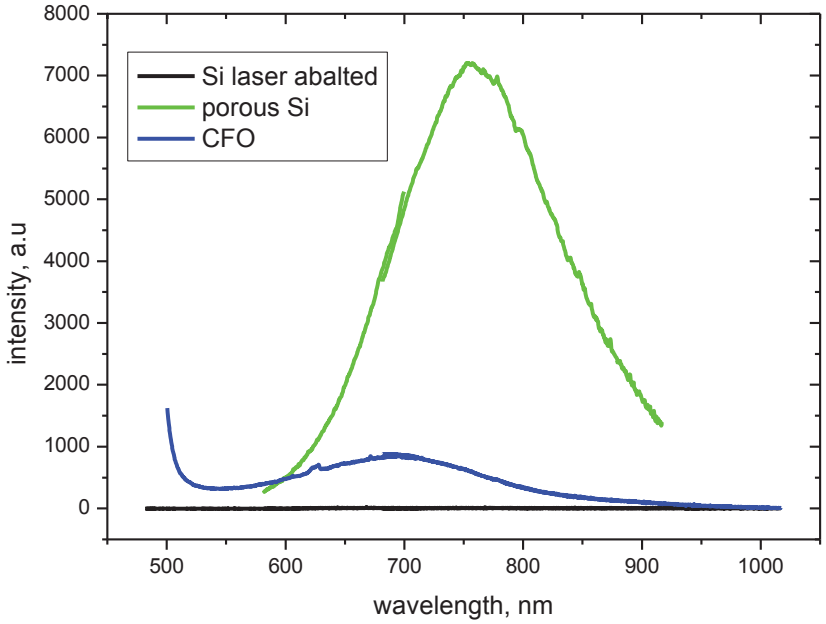

Figure 8.3 *The relative PL intensities of the porous silicon particles, ablated particles and CFO nanoparticles The excitation wavelength is 511 nm*

The XRD pattern of CFO nanoparticles is shown at Figure 8.4

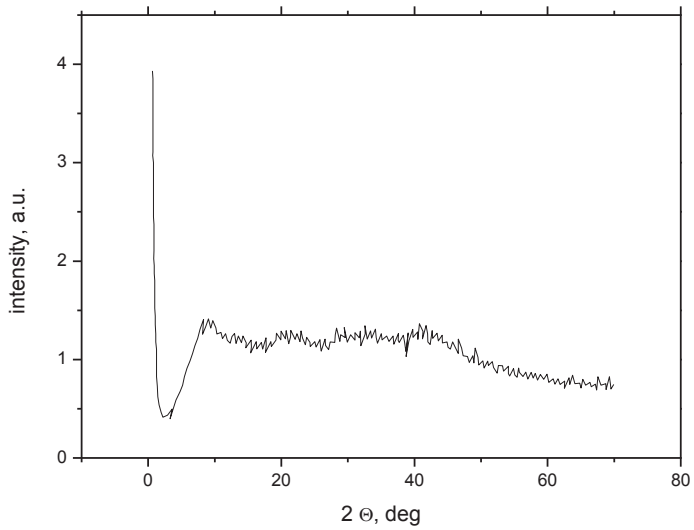

Figure 8.4 *XRD pattern of CFO nanoparticles*

Tables 8.1-8.6 show the significance of the difference in slopes based on histograms **6.3.1-6.3.6.**

The cells filled with red should not be considered as statistically significant with p>0.95.

table of paired t-values	concentration		1,5	1	0,5	0,25	0,1	0
concentration	mean slope		-0,03352	-0,02234	0,04167	0,06727	0,05128	0,01134
		slope SD	0,00201	0,00113	0,00363	0,00436	0,00297	0,00199
1,5	-0,03352	0,00201	0	-13,7137	-51,2538	-59,3786	-66,8811	-44,8594
1	-0,02234	0,00113	13,71366	0	-47,6214	-56,2727	-65,5281	-41,6271
0,5	0,04167	0,00363	51,25383	47,62136	0	-12,7629	-5,79534	20,72287
0,25	0,06727	0,00436	59,37858	56,27272	12,76286	0	8,573003	33,00746
0,1	0,05128	0,00297	66,88111	65,52808	5,795338	-8,573	0	31,5988
0	0,01134	0,00199	44,85944	41,62706	-20,7229	-33,0075	-31,5988	0
	mean slope		0,0368	0,05414	0,04828	0,02313	0,03329	0,05006
		slope SD	0,00238	0,00454	0,00479	0,00476	0,00981	0,00329
1,5	0,0368	0,00238	0	-9,56785	-6,07071	7,265266	0,983476	-9,2363
1	0,05414	0,00454	9,567852	0	2,511424	13,3339	5,455581	2,058229
0,5	0,04828	0,00479	6,070708	-2,51142	0	10,53398	3,88369	-0,86639
0,25	0,02313	0,00476	-7,26527	-13,3339	-10,534	0	-2,63548	-13,1637
0,1	0,03329	0,00981	-0,98348	-5,45558	-3,88369	2,635477	0	-4,58421
0	0,05006	0,00329	9,236298	-2,05823	0,866385	13,16369	4,584205	0

Table 8.1 *Matrix of T- values for the paired difference test for 3t3-L1. The cells filled with red should not be considered as statistically significant. Upper part is the matrix for the slopes difference before washing out, lower one – after washing out.*

table of paired t-values	concentration		1,5	1	0,5	0,25	0,1	0
concentration	mean		-0,00319	0,0012	0,0077	0,00933	0,0097	0,0127
		SD	0,00188	0,00197	8,12E-04	0,0025	0,00188	0,00275
1,5	-0,00319	0,00188	0	-4,55979	-15,0399	-11,3209	-13,7128	-13,4917
1	0,0012	0,00197	4,559793	0	-8,62769	-7,22456	-8,82876	-9,61535
0,5	0,0077	8,12E-04	15,03993	8,627693	0	-1,75387	-2,76215	-4,93193
0,25	0,00933	0,0025	11,32093	7,224562	1,753874	0	-0,33456	-2,56471
0,1	0,0097	0,00188	13,71277	8,828757	2,762154	0,334564	0	-2,54721
0	0,0127	0,00275	13,49174	9,615354	4,931932	2,564713	2,547214	0
	mean		-7,47E-04	0,04009	0,03582	0,03745	0,04797	0,04488
		SD	0,0029	0,00415	0,0052	0,00525	0,00671	0,00618
1,5	-7,47E-04	0,0029	0	-22,8141	-17,3711	-18,0131	-18,8502	-18,9044
1	0,04009	0,00415	22,8141	0	1,815327	1,11579	-2,82497	-1,81998
0,5	0,03582	0,0052	17,37106	-1,81533	0	-0,62392	-4,0482	-3,17279
0,25	0,03745	0,00525	18,01312	-1,11579	0,623916	0	-3,49247	-2,59161
0,1	0,04797	0,00671	18,85021	2,824967	4,048198	3,492469	0	0,958073
0	0,04488	0,00618	18,90439	1,819983	3,172791	2,591611	-0,95807	0

Table 8.2 *Matrix of T- values for the paired difference test for Hek293. The cells filled with red should not be considered as statistically significant. Upper part is the matrix for the slopes difference before washing out, lower one – after washing out.*

table of paired t-values	concentration		1,5	1	0,5	0,25	0,1	0
concentration	mean		-0,06035	-0,07973	-0,03041	-0,00244	0,02026	0,05133
	SD		0,04035	0,05719	2,03E-02	0,00302	0,01263	0,02551
1,5	-0,06035	0,04035	0	0,783165	-1,87575	-4,04801	-5,39255	-6,61697
1	-0,07973	0,05719	-0,78316	0	-2,29932	-3,81719	-4,82882	-5,91959
0,5	-0,03041	2,03E-02	1,87575	2,29932	0	-3,86399	-6,00508	-7,09836
0,25	-0,00244	0,00302	4,048014	3,817188	3,863987	0	-4,94418	-5,92042
0,1	0,02026	0,01263	5,392547	4,82882	6,005079	4,944177	0	-3,08723
0	0,05133	0,02551	6,616974	5,919588	7,098364	5,920418	3,087234	0
	mean		2,04E-04	0,00497	0,02323	0,05405	0,08738	0,13298
	SD		0,0141	0,0115	0,00309	0,00654	0,00929	0,0197
1,5	2,04E-04	0,0141	0	-0,74088	-4,51189	-9,79866	-14,6027	-15,5018
1	0,00497	0,0115	0,740876	0	-4,33721	-10,4931	-15,7669	-15,8725
0,5	0,02323	0,00309	4,511888	4,337211	0	-12,0516	-18,5328	-15,567
0,25	0,05405	0,00654	9,798656	10,4931	12,05161	0	-8,29771	-10,7552
0,1	0,08738	0,00929	14,60268	15,76687	18,53278	8,297706	0	-5,92162
0	0,13298	0,0197	15,50181	15,8725	15,56702	10,75519	5,921615	0

Table 8.3 *Matrix of T- values for the paired difference test for HSC. The cells filled with red should not be considered as statistically significant. Upper part is the matrix for the slopes difference before washing out, lower one – after washing out.*

table of paired t-values	concentration		1,5	1	0,5	0,25	0,1	0
concentration	mean		-0,01282	-0,01032	-0,00547	-0,00458	-0,00439	0,01959
	SD		0,00248	0,00263	1,54E-03	0,000436	0,00212	0,00192
1,5	-0,01282	0,00248	0	-1,9561	-7,12134	-9,25583	-7,30809	-29,2279
1	-0,01032	0,00263	1,956105	0	-4,50105	-6,09001	-4,96515	-25,9801
0,5	-0,00547	1,54E-03	7,121337	4,501051	0	-1,57283	-1,16578	-28,7979
0,25	-0,00458	0,000436	9,255825	6,090009	1,572833	0	-0,2483	-34,7224
0,1	-0,00439	0,00212	7,308089	4,965147	1,165781	0,248298	0	-23,7135
0	0,01959	0,00192	29,22787	25,9801	28,79794	34,72238	23,71353	0
	mean		-3,93E-05	1,93E-04	-1,30E-03	-0,00101	-0,00221	0,01886
	SD		8,96E-04	6,13E-04	4,11E-04	4,73E-04	5,93E-04	3,39E-04
1,5	-3,93E-05	8,96E-04	0	-0,60522	3,617282	2,709824	5,714187	-55,7997
1	1,93E-04	6,13E-04	0,605221	0	5,721766	4,394574	7,969054	-75,373
0,5	-1,30E-03	4,11E-04	-3,61728	-5,72177	0	-1,309	3,567359	-107,028
0,25	-0,00101	4,73E-04	-2,70982	-4,39457	1,309002	0	4,474553	-96,5756
0,1	-0,00221	5,93E-04	-5,71419	-7,96905	-3,56736	-4,47455	0	-87,2471
0	0,01886	3,39E-04	55,79967	75,37302	107,0279	96,57558	87,24712	0

Table 8.4 *Matrix of T- values for the paired difference test for HuH7. The cells filled with red should not be considered as statistically significant. Upper part is the matrix for the slopes difference before washing out, lower one – after washing out.*

table of paired t-values	concentration		1,5	1	0,5	0,25	0,1	0
concentration	mean		-0,0628	-0,097	-0,0855	-0,045	-0,0336	-0,0318
		SD	0,00382	0,01849	3,00E-02	0,01594	0,01044	0,01325
1,5	-0,0628	0,00382	0	5,123398	2,120947	-3,0715	-7,42922	-,35847
1	-0,097	0,01849	-5,1234	0	-0,92233	-6,02474	-8,44514	8,10702
0,5	-0,0855	3,00E-02	-2,12095	0,922334	0	-3,36932	-4,61722	4,62741
0,25	-0,045	0,01594	3,0715	6,024742	3,369324	0	-1,69219	1,80121
0,1	-0,0336	0,01044	7,42922	8,445139	4,617224	1,692195	0	0,30181
0	-0,0318	0,01325	6,358474	8,107025	4,627412	1,801206	0,30181	0
	mean		0,0091	1,54E-02	2,35E-02	4,78E-02	0,06066	0,06972
		SD	8,93E-05	6,37E-04	2,29E-03	2,74E-03	2,18E-03	2,19E-03
1,5	0,0091	8,93E-05	0	-27,7026	-17,7969	-39,9278	-66,8401	78,2269
1	1,54E-02	6,37E-04	27,70256	0	-9,66233	-32,5769	-56,3653	67,3636
0,5	2,35E-02	2,29E-03	17,79692	9,662329	0	-19,2313	-33,2248	41,2397
0,25	4,78E-02	2,74E-03	39,92775	32,57687	19,23134	0	-10,3882	17,6753
0,1	0,06066	2,18E-03	66,84014	56,36529	33,22484	10,38821	0	8,29288
0	0,06972	2,19E-03	78,22689	67,36356	41,23973	17,67534	8,292884	0

Table 8.5 *Matrix of T- values for the paired difference test for PANC1. The cells filled with red should not be considered as statistically significant. Upper part is the matrix for the slopes difference before washing out, lower one – after washing out.*

table of paired t-values	concentration		1,5	1	0,5	0,25	0,1	0
concentration	mean		-0,02538	-0,01502	0,00563	0,03599	0,0436	0,04044
		SEM	0,00266	0,00404	4,89E-03	0,00841	0,00813	0,00487
1,5	-0,02538	0,00266	0	-6,05791	-15,7562	-19,6789	-22,8084	-33,5491
1	-0,01502	0,00404	6,05791	0	-9,2081	-15,4638	-18,2633	-24,7905
0,5	0,00563	4,89E-03	15,75622	9,208101	0	-8,82691	-11,3199	-14,2664
0,25	0,03599	0,00841	19,67891	15,46382	8,826915	0	-1,84012	-1,29514
0,1	0,0436	0,00813	22,80837	18,26327	11,3199	1,840123	0	0,943106
0	0,04044	0,00487	33,54906	24,79054	14,26636	1,295136	-0,94311	0
	mean		-4,99E-03	-0,00234	0,04073	0,05467	0,06784	0,05831
		SEM	4,38E-03	1,93E-03	2,09E-03	3,69E-03	0,00422	0,00242
1,5	-4,99E-03	4,38E-03	0	-1,56598	-26,646	-29,4637	-33,8686	-35,7787
1	-0,00234	1,93E-03	1,565975	0	-42,8218	-38,7221	-42,7763	-55,4196
0,5	0,04073	2,09E-03	26,64604	42,82182	0	-9,29741	-16,2828	-15,5504
0,25	0,05467	3,69E-03	29,46375	38,72211	9,297415	0	-6,64502	-2,33311
0,1	0,06784	0,00422	33,86856	42,77628	16,28276	6,645024	0	5,540979
0	0,05831	0,00242	35,7787	55,41962	15,55045	2,333112	-5,54098	0

Table 8.6 *Matrix of T- values for the paired difference test for HepG2. The cells filled with red should not be considered as statistically significant. Upper part is the matrix for the slopes difference before washing out, lower one – after washing out.*

table of paired t-values	Cell line		3T3-L1	PANC01	Hek293	HSC	HuH7	HepG2
Cell line	Mean PL		55,93	91,03	113,93	133,79	146,98	160,56
		SD	2,56	9,24	9,13	5,99	6,07	4,22
3T3-L1	55,93	2,56	0,00	-3,66	-6,11	-11,96	-13,81	-21,18
PANC01	91,03	9,24	3,66	0,00	-1,76	-3,89	-5,06	-6,85
Hek293	113,93	9,13	6,11	1,76	0,00	-1,82	-3,01	-4,63
HSC	133,79	5,99	11,96	3,89	1,82	0,00	-1,55	-3,65
HuH7	146,98	6,07	13,81	5,06	3,01	1,55	0,00	-1,84
HepG2	160,56	4,22	21,18	6,85	4,63	3,65	1,84	0,00

Table 8.7 *Matrix of T- values for the paired difference test for photoluminescence of different cell lines. The table cells filled with red should not be considered as statistically significant.*

9. References

1 Ekimov, A. I., & Onushchenko, A. A. (1982). Quantum size effect in the optical-spectra of semiconductor micro-crystals. *Soviet Physics Semiconductors-Ussr*, *16*(7), 775-778.

2 Derfus, A. M., Chan, W. C., & Bhatia, S. N. (2004). Probing the cytotoxicity of semiconductor quantum dots. *Nano letters*, *4*(1), 11-18.

3 Kirchner, C., Liedl, T., Kudera, S., Pellegrino, T., Muñoz Javier, A., Gaub, H. E., ... & Parak, W. J. (2005). Cytotoxicity of colloidal CdSe and CdSe/ZnS nanoparticles. *Nano letters*, *5*(2), 331-338.

4 Lewinski, N., Colvin, V., & Drezek, R. (2008). Cytotoxicity of nanoparticles. *small*, *4*(1), 26-49.

5 Silva, G. A. (2006). Neuroscience nanotechnology: progress, opportunities and challenges. Nature Reviews Neuroscience, 7(1), 65-74.

6 Loeper, J., & Fragny, M. (1978, January). The physiological role of the silicon and its antiatheromatous action. In *Biochemistry of silicon and related problems* (pp. 281-296). Springer US.

7 Fernandez-Rosas, E., Gomez, R., Ibanez, E., Barrios, L., Duch, M., Esteve, J., ... & Plaza, J. A. (2009). Intracellular polysilicon barcodes for cell tracking. *Small*, *5*(21), 2433-2439.

8 He, Y., & Su, Y. (2014). *Silicon Nano-biotechnology*. Berlin: Springer.

9 Cullis, A. G., Canham, L. T., & Calcott, P. D. J. (1997). The structural and luminescence properties of porous silicon. *Journal of Applied Physics*, *82*(3), 909-965.

10 Uhlir, A. (1956). Electrolytic shaping of germanium and silicon. *Bell System Technical Journal*, *35*(2), 333-347.

11 Canham, L. T. (1990). Silicon quantum wire array fabrication by electrochemical and chemical dissolution of wafers. *Applied Physics Letters*, *57*(10), 1046-1048.

12 Seidel, H., Csepregi, L., Heuberger, A., & Baumgärtel, H. (1990). Anisotropic etching of crystalline silicon in alkaline solutions I. Orientation dependence and behavior of passivation layers. *Journal of the electrochemical society*, *137*(11), 3612-3626.

13 Tu, C. C., Chou, Y. N., Hung, H. C., Wu, J., Jiang, S., & Lin, L. Y. (2014). Fluorescent porous silicon biological probes with high quantum efficiency and stability. *Optics express*, *22*(24), 29996-30003.

14 Cullis, A. G., Canham, L. T., & Calcott, P. D. J. (1997). The structural and luminescence properties of porous silicon. *Journal of Applied Physics*, *82*(3), 909-965.

15 Baldwin, R. K., Pettigrew, K. A., Ratai, E., Augustine, M. P., & Kauzlarich, S. M. (2002). Solution reduction synthesis of surface stabilized silicon nanoparticles. *Chem. Commun.*, (17), 1822-1823.

16 Heintz, A. S., Fink, M. J., & Mitchell, B. S. (2007). Mechanochemical synthesis of blue luminescent alkyl/alkenyl-passivated silicon nanoparticles. *Advanced Materials*, *19*(22), 3984-3988.

17 Her, T. H., Finlay, R. J., Wu, C., Deliwala, S., & Mazur, E. (1998). Microstructuring of silicon with femtosecond laser pulses. *Applied Physics Letters*, *73*(12), 1673-1675.

18 Hofmeister, H., Huisken, F., & Kohn, B. (1999). Lattice contraction in nanosized silicon particles produced by laser pyrolysis of silane. *The European Physical Journal D-Atomic, Molecular, Optical and Plasma Physics*, *9*(1), 137-140.

19 Švrček, V., Sasaki, T., Shimizu, Y., & Koshizaki, N. (2006). Blue luminescent silicon nanocrystals prepared by ns pulsed laser ablation in water. *Applied physics letters*, *89*(21), 213113.

20 Tan, D., Xu, B., Chen, P., Dai, Y., Zhou, S., Ma, G., & Qiu, J. (2012). One-pot synthesis of luminescent hydrophilic silicon nanocrystals. *RSC Advances*, *2*(22), 8254-8257.

21 Arul Dhas, N., Raj, C. P., & Gedanken, A. (1998). Preparation of luminescent silicon nanoparticles: a novel sonochemical approach. *Chemistry of materials*, *10*(11), 3278-3281.

22 Yamada, Y., Orii, T., Umezu, I., Takeyama, S., & Yoshida, T. (1996). Optical properties of silicon nanocrystallites prepared by excimer laser ablation in inert gas. *Japanese journal of applied physics*, *35*(part 1), 1361-1365.

23 Ehbrecht, M., & Huisken, F. (1999). Gas-phase characterization of silicon nanoclusters produced by laser pyrolysis of silane. *Physical Review B*, *59*(4), 2975.

24 Baldwin, R. K., Pettigrew, K. A., Ratai, E., Augustine, M. P., & Kauzlarich, S. M. (2002). Solution reduction synthesis of surface stabilized silicon nanoparticles. *Chem. Commun.*, (17), 1822-1823.

25 Borsella, E., D'Amato, R., Terranova, G., Falconieri, M., & Fabbri, F. (2011). Synthesis of nanoparticles by laser pyrolysis: from research to applications. *Energia, Ambiente Innovazione*, 4-5.

26 Amoruso, S., Bruzzese, R., Spinelli, N., Velotta, R., Vitiello, M., Wang, X., ... & Lanotte, L. (2004). Generation of silicon nanoparticles via femtosecond laser ablation in vacuum. *Applied Physics Letters*, *84*(22), 4502-4504.

27 Švrček, V., Sasaki, T., Shimizu, Y., & Koshizaki, N. (2006). Blue luminescent silicon nanocrystals prepared by ns pulsed laser ablation in water. *Applied physics letters*, *89*(21), 213113.

28 Huang, Z., Geyer, N., Werner, P., De Boor, J., & Gösele, U. (2011). Metal-assisted chemical etching of silicon: a review. *Advanced materials*, *23*(2), 285-308.

29 Wagner, R. S., & Treuting, R. G. (1961). Morphology and growth mechanism of silicon ribbons. *Journal of Applied Physics*, 32(11), 2490-2491.

30 Wagner, R. S., Ellis, W. C., Jackson, K. A., & Arnold, S. M. (1964). Study of the filamentary growth of silicon crystals from the vapor. *Journal of Applied Physics*, *35*(10), 2993-3000.

31 Gogotsi, Y., & Presser, V. (Eds.). (2013). *Carbon nanomaterials*. CRC Press.

32 Dai, H. (2002). Carbon nanotubes: synthesis, integration, and properties. *Accounts of chemical research*, *35*(12), 1035-1044.

33 Ajayan, P. M., & Zhou, O. Z. (2001). Applications of carbon nanotubes. In *Carbon nanotubes* (pp. 391-425). Springer Berlin Heidelberg.

34 Dai, H. (2001). Nanotube growth and characterization. In *Carbon Nanotubes* (pp. 29-53). Springer Berlin Heidelberg.

35 Dresselhaus M. S., Dresselhaus G., Eklund P. C. Science of fullerenes and carbon nanotubes: their properties and applications. – Academic press, 1996.

36 Geckeler, K. E., & Samal, S. (1999). Syntheses and properties of macromolecular fullerenes, a review. *Polymer international*, *48*(9), 743-757.

37 Geim, A. K., & Novoselov, K. S. (2007). The rise of graphene. *Nature materials*, *6*(3), 183-191.

38 Mochalin, V. N., Shenderova, O., Ho, D., & Gogotsi, Y. (2012). The properties and applications of nanodiamonds. *Nature nanotechnology*, *7*(1), 11-23.

39 Khachatryan, A. K., Aloyan, S. G., May, P. W., Sargsyan, R., Khachatryan, V. A., & Baghdasaryan, V. S. (2008). Graphite-to-diamond transformation induced by ultrasound cavitation. *Diamond and Related Materials*, *17*(6), 931-936.

40 Kumar, A., Lin, P. A., Xue, A., Hao, B., Yap, Y. K., & Sankaran, R. M. (2013). Formation of nanodiamonds at near-ambient conditions via microplasma dissociation of ethanol vapour. *Nature communications*, *4*.

41 Butler, J. E., & Sumant, A. V. (2008). The CVD of nanodiamond materials. *Chemical Vapor Deposition*, *14*(7-8), 145-160.

42 Mochalin, V. N., & Gogotsi, Y. (2009). Wet chemistry route to hydrophobic blue fluorescent nanodiamond. *Journal of the American Chemical Society*, *131*(13), 4594-4595.

43 Borchardt, L., Oschatz, M., & Kaskel, S. (2014). Tailoring porosity in carbon materials for supercapacitor applications. *Materials Horizons*, *1*(2), 157-168.

44 Gogotsi, Y., Nikitin, A., Ye, H., Zhou, W., Fischer, J. E., Yi, B. & Barsoum, M. W. (2003). Nanoporous carbide-derived carbon with tunable pore size. *Nature materials*, *2*(9), 591-594.

45 Rossi, A. M., Murphy, T. E., & Reipa, V. (2008). Ultraviolet photoluminescence from 6H silicon carbide nanoparticles. *Applied Physics Letters*, *92*(25), 253112-253112.

46 Saddow, S. E. (2012). *Silicon carbide biotechnology: a biocompatible semiconductor for advanced biomedical devices and applications*. Elsevier.

47 Andrievski, R. A. (2009). Synthesis, structure and properties of nanosized silicon carbide. *Rev. Adv. Mater. Sci*, *22*, 1-20.

48 Wang, Z. M. (Ed.). (2008). *One-dimensional nanostructures* (Vol. 3). Springer Science & Business Media.

49 Zhang, F., Lees, E., Amin, F., Rivera_Gil, P., Yang, F., Mulvaney, P., & Parak, W. J. (2011). Polymer-Coated Nanoparticles: A Universal Tool for Biolabelling Experiments. *Small*, *7*(22), 3113-3127.

50 Intensive programme Design, Synthesis and Validation of Imaging Probes Turin (Italy) – September 23 to October 4, 2013 Imaging Probe: design and synthesis
Alessandro Barge private communication

51 Canham, L. T. (2007). Nanoscale semiconducting silicon as a nutritional food additive. *Nanotechnology*, *18*(18), 185704.

52 Ogata, Y., Niki, H., Sakka, T., & Iwasaki, M. (1995). Oxidation of porous silicon under water vapor environment. *Journal of The Electrochemical Society*, *142*(5), 1595-1601.

53 Buriak, J. M., Stewart, M. P., Geders, T. W., Allen, M. J., Choi, H. C., Smith, J., ... & Canham, L. T. (1999). Lewis acid mediated hydrosilylation on porous silicon surfaces. *Journal of the American Chemical Society*, *121*(49), 11491-11502.

54 Mäkilä, E., Bimbo, L. M., Kaasalainen, M., Herranz, B., Airaksinen, A. J., Heinonen, M., ... & Salonen, J. (2012). Amine modification of thermally carbonized porous silicon with silane coupling chemistry. *Langmuir*, *28*(39), 14045-14054.

55 Wu, H. C., Chang, X., Liu, L., Zhao, F., & Zhao, Y. (2010). Chemistry of carbon nanotubes in biomedical applications. *Journal of Materials Chemistry*, *20*(6), 1036-1052.

56 Mochalin, V. N., Shenderova, O., Ho, D., & Gogotsi, Y. (2012). The properties and applications of nanodiamonds. *Nature nanotechnology*, *7*(1), 11-23.

57 Luo, Y., Rong, M. Z., Zhang, M. Q., & Friedrich, K. (2004). Surface grafting onto SiC nanoparticles with glycidyl methacrylate in emulsion. *Journal of Polymer Science Part A: Polymer Chemistry*, *42*(15), 3842-3852.

58 Yakimova, R., Petoral Jr, R. M., Yazdi, G. R., Vahlberg, C., Lloyd Spetz, A., & Uvdal, K. (2007). REVIEW ARTICLE: Surface functionalization and biomedical applications based on SiC. *Journal of Physics D Applied Physics*, *40*, 6435-6442.

59 Schoell, S. J., Sachsenhauser, M., Oliveros, A., Howgate, J., Stutzmann, M., Brandt, M. S., ... & Sharp, I. D. (2013). Organic functionalization of 3C-SiC surfaces. *ACS applied materials & interfaces*, *5*(4), 1393-1399.

60 Ahire, J. H., Wang, Q., Coxon, P. R., Malhotra, G., Brydson, R., Chen, R., & Chao, Y. (2012). Highly luminescent and nontoxic amine-capped nanoparticles from porous silicon: synthesis and their use in biomedical imaging. *ACS applied materials & interfaces*, *4*(6), 3285-3292.

61 Osminkina, L. A., Tamarov, K. P., Sviridov, A. P., Galkin, R. A., Gongalsky, M. B., Solovyev, V. V., ... & Timoshenko, V. Y. (2012). Photoluminescent biocompatible silicon nanoparticles for cancer theranostic applications. *Journal of biophotonics*, *5*(7), 529-535.

62 Gonchar, K. A., Osminkina, L. A., Galkin, R. A., Gongalsky, M. B., Marshov, V. S., Timoshenko, V. Y., ... & Sivakov, V. A. (2012). Growth, Structure and Optical Properties of Silicon Nanowires Formed by Metal-Assisted Chemical Etching. *Journal of Nanoelectronics and Optoelectronics*, *7*(6), 602-606.

63 Park, J. H., Gu, L., Von Maltzahn, G., Ruoslahti, E., Bhatia, S. N., & Sailor, M. J. (2009). Biodegradable luminescent porous silicon nanoparticles for in vivo applications. *Nature materials*, *8*(4), 331-336.

64 Zhu, S., Zhang, J., Qiao, C., Tang, S., Li, Y., Yuan, W., ... & Yang, B. (2011). Strongly green-photoluminescent graphene quantum dots for bioimaging applications. *Chem. Commun.*, *47*(24), 6858-6860.

65 Fan, J., & Chu, P. K. (2010). Group IV nanoparticles: synthesis, properties, and biological applications. *Small*, *6*(19), 2080-2098.

66 Vaijayanthimala, V., Cheng, P. Y., Yeh, S. H., Liu, K. K., Hsiao, C. H., Chao, J. I., & Chang, H. C. (2012). The long-term stability and biocompatibility of fluorescent nanodiamond as an in vivo contrast agent. *Biomaterials*, *33*(31), 7794-7802.

67 Welsher, K., Liu, Z., Sherlock, S. P., Robinson, J. T., Chen, Z., Daranciang, D., & Dai, H. (2009). A route to brightly fluorescent carbon nanotubes for near-infrared imaging in mice. *Nature nanotechnology*, *4*(11), 773-780.

68 Serdiuk, T., Alekseev, S. A., Lysenko, V., Skryshevsky, V. A., & Géloën, A. (2012). Charge-driven selective localization of fluorescent nanoparticles in live cells. *Nanotechnology*, *23*(31), 315101.

69 Fan, J., Li, H., Jiang, J., So, L. K., Lam, Y. W., & Chu, P. K. (2008). 3C–SiC nanocrystals as fluorescent biological labels. *Small*, *4*(8), 1058-1062.

70 Song, Y., Gao, D., Kim, H. S., Qu, C., Kang, J., Zhu, Y., ... & Lee, C. S. (2014). Fabrication of Silicon Carbide Quantum Dots via Chemical-Etching Approach and Fluorescent Imaging for Living Cells. *Materials Sciences and Applications*, *2014*.

71 Pawlicki, M., Collins, H. A., Denning, R. G., & Anderson, H. L. (2009). Two-Photon Absorption and the Design of Two-Photon Dyes. *Angewandte Chemie International Edition*, *48*(18), 3244-3266.

72 Park, J. H., Gu, L., Von Maltzahn, G., Ruoslahti, E., Bhatia, S. N., & Sailor, M. J. (2009). Biodegradable luminescent porous silicon nanoparticles for in vivo applications. *Nature materials*, *8*(4), 331-336.

73 Wang, F., Dukovic, G., Brus, L. E., & Heinz, T. F. (2005). The optical resonances in carbon nanotubes arise from excitons. *Science*, *308*(5723), 838-841.

74 Cao, L., Wang, X., Meziani, M. J., Lu, F., Wang, H., Luo, P. G., ... & Sun, Y. P. (2007). Carbon dots for multiphoton bioimaging. *Journal of the American Chemical Society*, *129*(37), 11318-11319.

75 Beke, D., Szekrényes, Z., Pálfi, D., Róna, G., Balogh, I., Maák, P. A., ... & Gali, A. (2013). Silicon carbide quantum dots for bioimaging. *Journal of Materials Research*, *28*(02), 205-209.

76 Liu, Z., Li, X., Tabakman, S. M., Jiang, K., Fan, S., & Dai, H. (2008). Multiplexed multicolor Raman imaging of live cells with isotopically modified single walled carbon nanotubes. *Journal of the American Chemical Society*, *130*(41), 13540-13541.

77 De La Zerda, Adam, et al. "Carbon nanotubes as photoacoustic molecular imaging agents in living mice." *Nature nanotechnology* 3.9 (2008): 557-562.

78 Wu, Lina, et al. "A green synthesis of carbon nanoparticles from honey and their use in real-time photoacoustic imaging." *Nano research* 6.5 (2013): 312-325.

79 Benedetto, G., L. Boarino, and R. Spagnolo. "Evaluation of thermal conductivity of porous silicon layers by a photoacoustic method." *Applied Physics A* 64.2 (1997): 155-159.

80 Wu, L., Cai, X., Nelson, K., Xing, W., Xia, J., Zhang, R., ... & Pan, D. (2013). A green synthesis of carbon nanoparticles from honey and their use in real-time photoacoustic imaging. *Nano research*, *6*(5), 312-325.

81 Hong, C., Lee, J., Zheng, H., Hong, S. S., & Lee, C. (2011). Porous silicon nanoparticles for cancer photothermotherapy. *Nanoscale research letters*, *6*(1), 1-8.

82 van der Zee, J. (2002). Heating the patient: a promising approach?. *Annals of oncology*, *13*(8), 1173-1184.

83 O'Neal, D. P., Hirsch, L. R., Halas, N. J., Payne, J. D., & West, J. L. (2004). Photo-thermal tumor ablation in mice using near infrared-absorbing nanoparticles. *Cancer letters*, *209*(2), 171-176.

84 Hong, C., Lee, J., Zheng, H., Hong, S. S., & Lee, C. (2011). Porous silicon nanoparticles for cancer photothermotherapy. *Nanoscale research letters*, *6*(1), 1-8.

85 Sviridov, A. P., Andreev, V. G., Ivanova, E. M., Osminkina, L. A., Tamarov, K. P., & Timoshenko, V. Y. (2013). Porous silicon nanoparticles as sensitizers for ultrasonic hyperthermia. *Applied Physics Letters*, *103*(19), 193110.

86 Munoz-Noval, A., Sánchez-Vaquero, V., Torres-Costa, V., Gallach, D., Ferro-Llanos, V., Serrano, J. J., ... & Martín-Palma, R. J. (2011). Hybrid luminescent/magnetic nanostructured porous silicon particles for biomedical applications. *Journal of biomedical optics*, *16*(2), 025002-025002.

87 Su, Y., Wei, X., Peng, F., Zhong, Y., Lu, Y., Su, S., ... & He, Y. (2012). Gold nanoparticles-decorated silicon nanowires as highly efficient near-infrared hyperthermia agents for cancer cells destruction. *Nano letters*, *12*(4), 1845-1850.

88 Singh, R., & Torti, S. V. (2013). Carbon nanotubes in hyperthermia therapy. *Advanced drug delivery reviews*, *65*(15), 2045-2060.

89 Markovic, Z. M., Harhaji-Trajkovic, L. M., Todorovic-Markovic, B. M., Kepić, D. P., Arsikin, K. M., Jovanović, S. P., ... & Trajkovic, V. S. (2011). In vitro comparison of the photothermal anticancer activity of graphene nanoparticles and carbon nanotubes. *Biomaterials*, *32*(4), 1121-1129.

[90] Fuchs, B. B., Prates, R. A., Astrakas, C., St Denis, T. G., Ribeiro, M. S., Dai, T., ... & Tegos, G. (2012). Concepts and principles of photodynamic therapy as an alternative antifungal discovery platform.

91 Kovalev, D., Gross, E., Künzner, N., Koch, F., Timoshenko, V. Y., & Fujii, M. (2002). Resonant electronic energy transfer from excitons confined in silicon nanocrystals to oxygen molecules. *Physical review letters*, *89*(13), 137401.

92 Kovalev, D., & Fujii, M. (2005). Silicon nanocrystals: photosensitizers for oxygen molecules. *Advanced Materials*, *17*(21), 2531-2544.

93 Gross, E., Kovalev, D., Künzner, N., Diener, J., Koch, F., Timoshenko, V. Y., & Fujii, M. (2003). Spectrally resolved electronic energy transfer from silicon nanocrystals to molecular oxygen mediated by direct electron exchange. *Physical Review B*, *68*(11), 115405.

94 Gongalsky, M. B., Kharin, A. Y., Zagorodskikh, S. A., Osminkina, L. A., & Timoshenko, V. Y. (2011). Photosensitized generation of singlet oxygen in porous silicon studied by simultaneous measurements of luminescence of nanocrystals and oxygen molecules. *Journal of Applied Physics*, *110*(1), 013707.

95 Murakami, T., Nakatsuji, H., Inada, M., Matoba, Y., Umeyama, T., Tsujimoto, M., ... & Imahori, H. (2012). Photodynamic and photothermal effects of semiconducting and metallic-enriched single-walled carbon nanotubes. *Journal of the American Chemical Society*, *134*(43), 17862-17865.

96 Huang, P., Lin, J., Wang, X., Wang, Z., Zhang, C., He, M., ... & Chen, X. (2012). Light-triggered theranostics based on photosensitizer-conjugated carbon dots for simultaneous enhanced-fluorescence imaging and photodynamic therapy. *Advanced Materials*, *24*(37), 5104-5110.

97 Kang, B., Yu, D., Dai, Y., Chang, S., Chen, D., & Ding, Y. (2009). Cancer-cell targeting and photoacoustic therapy using carbon nanotubes as “Bomb” agents. *Small*, *5*(11), 1292-1301.

98 Anglin, E. J., Cheng, L., Freeman, W. R., & Sailor, M. J. (2008). Porous silicon in drug delivery devices and materials. *Advanced drug delivery reviews*, *60*(11), 1266-1277.

99 Liu, Z., Robinson, J. T., Tabakman, S. M., Yang, K., & Dai, H. (2011). Carbon materials for drug delivery & cancer therapy. *Materials today*, *14*(7), 316-323.

100 Bianco, A., Kostarelos, K., & Prato, M. (2005). Applications of carbon nanotubes in drug delivery. *Current opinion in chemical biology*, *9*(6), 674-679.

101 Mochalin, V. N., Shenderova, O., Ho, D., & Gogotsi, Y. (2012). The properties and applications of nanodiamonds. Nature nanotechnology, 7(1), 11-23.

102 Dynamic light scattering. (2016, January 27). In Wikipedia, The Free Encyclopedia. Retrieved 17:53, February 3, 2016, from https://en.wikipedia.org/w/index.php?title=Dynamic_light_scattering&oldid=701938497

103 Zeta potential. (2015, May 18). In Wikipedia, The Free Encyclopedia. Retrieved 09:14, February 1, 2016, from https://en.wikipedia.org/w/index.php?title=Zeta_potential&oldid=662898994

104 O'Brien, R. W. (1990). Electroacoustic studies of moderately concentrated colloidal suspensions. Faraday Discussions of the Chemical Society, 90, 301-312.

105 http://www.malvern.com/en/products/product-range/zetasizer-range/zetasizer-nano-range/zetasizer-nano-z/

106 Zipfel, W. R., Williams, R. M., Christie, R., Nikitin, A. Y., Hyman, B. T., & Webb, W. W. (2003). Live tissue intrinsic emission microscopy using multiphoton-excited native fluorescence and second harmonic generation. Proceedings of the National Academy of Sciences, 100(12), 7075-7080.

107 Tu, C., Ma, X., Pantazis, P., Kauzlarich, S. M., & Louie, A. Y. (2010). Paramagnetic, silicon quantum dots for magnetic resonance and two-photon imaging of macrophages. *Journal of the American Chemical Society*, *132*(6), 2016-2023.

108 Nayfeh, M. H., Akcakir, O., Belomoin, G., Barry, N., Therrien, J., & Gratton, E. (2000). Second harmonic generation in microcrystallite films of ultrasmall Si nanoparticles. *Applied Physics Letters*, *77*(25), 4086-4088.

109 Dadap, J. I., Shan, J., & Heinz, T. F. (2004). Theory of optical second-harmonic generation from a sphere of centrosymmetric material: small-particle limit. *JOSA B*, *21*(7), 1328-1347.

110 Pantazis, P., Maloney, J., Wu, D., & Fraser, S. E. (2010). Second harmonic generating (SHG) nanoprobes for in vivo imaging. *Proceedings of the National Academy of Sciences*, *107*(33), 14535-14540.

111 ACEA biosciences inc. http://www.aceabio.com.cn/en/theory.aspx

112 Gongalsky, M. B., Kharin, A. Y., Osminkina, L. A., Timoshenko, V. Y., Jeong, J., Lee, H., & Chung, B. H. (2012). Enhanced photoluminescence of porous silicon nanoparticles coated by bioresorbable polymers. *Nanoscale research letters*, 7(1), 1-7.

113 Alekseev, S., Korytko, D., Iazykov, M., Khainakov, S. A., & Lysenko, V. (2015). Electrochemical Synthesis of Carbon Fluorooxide Nanoparticles from 3C-SiC Substrates. *The Journal of Physical Chemistry C*.

114 http://www.kmlabs.biz/en/products/SiC-en

115 Renka, R. J., & Cline, A. K. (1984). A triangle-based C1 interpolation method. *Rocky Mountain J. Math*, *14*(1).

116 Farrugia, A. (2010). Albumin usage in clinical medicine: tradition or therapeutic? *Transfusion medicine reviews*, *24*(1), 53-63.

117 Connor, E. E., Mwamuka, J., Gole, A., Murphy, C. J., & Wyatt, M. D. (2005). Gold nanoparticles are taken up by human cells but do not cause acute cytotoxicity. *Small*, *1*(3), 325-327.

118 Tian, F., Cui, D., Schwarz, H., Estrada, G. G., & Kobayashi, H. (2006). Cytotoxicity of single-wall carbon nanotubes on human fibroblasts. *Toxicology in vitro*, *20*(7), 1202-1212.

119 Ankamwar, B., Lai, T. C., Huang, J. H., Liu, R. S., Hsiao, M., Chen, C. H., & Hwu, Y. K. (2010). Biocompatibility of Fe3O4 nanoparticles evaluated by in vitro cytotoxicity assays using normal, glia and breast cancer cells. *Nanotechnology*, *21*(7), 075102.

120 Panyam, J., & Labhasetwar, V. (2003). Dynamics of endocytosis and exocytosis of poly (D, L-lactide-co-glycolide) nanoparticles in vascular smooth muscle cells. *Pharmaceutical research*, *20*(2), 212-220.

121 Shapero, K., Fenaroli, F., Lynch, I., Cottell, D. C., Salvati, A., & Dawson, K. A. (2011). Time and space resolved uptake study of silica nanoparticles by human cells. *Molecular Biosystems*, *7*(2), 371-378.

122 Aggarwal, P., Hall, J. B., McLeland, C. B., Dobrovolskaia, M. A., & McNeil, S. E. (2009). Nanoparticle interaction with plasma proteins as it relates to particle biodistribution, biocompatibility and therapeutic efficacy. *Advanced drug delivery reviews*, *61*(6), 428-437.

123 Botsoa, J., Lysenko, V., Géloën, A., Marty, O., Bluet, J. M., & Guillot, G. (2008). Application of 3C-SiC quantum dots for living cell imaging. Applied Physics Letters, 92(17), 173902.

124 Serdiuk, T., Alekseev, S. A., Lysenko, V., Skryshevsky, V. A., & Géloën, A. (2012). Charge-driven selective localization of fluorescent nanoparticles in live cells. *Nanotechnology*, *23*(31), 315101.

125 Wu, F., Wang, Z. B., Chen, W. Z., Wang, W., Gui, Y., Zhang, M., ... & Feng, R. (2004). Extracorporeal high intensity focused ultrasound ablation in the treatment of 1038 patients with solid carcinomas in China: an overview. *Ultrasonics sonochemistry*, *11*(3), 149-154.